

Design of Software Defined Radio for SuperDARN Radars

Paul Steven Kennedy

Thesis submitted to the Faculty of the
Virginia Polytechnic Institute and State University
in partial fulfillment of the requirements for the degree of

Master of Science
in
Electrical Engineering

J. Michael Ruohoniemi, Chair
Joseph B.H. Baker
Gregory D. Earle
Robert W. McGwier

May 3, 2019
Blacksburg, Virginia

Keywords: Software Defined Radio, HF Radar, SuperDARN, Red Pitaya

Copyright 2019, Paul Steven Kennedy

Design of Software Defined Radio for SuperDARN Radars

Paul Steven Kennedy

ABSTRACT

Software defined radio (SDR) is a rapidly developing field enabled by continuing improvements in digital electronics. Software defined radio has been used extensively in communication systems due to its flexibility and cost effectiveness. Recently, SDR has been incorporated into radar systems, particularly for ionospheric research. This study investigated the benefits and design of a high frequency (HF) SDR receiver for the next generation of Super Dual Auroral Network (SuperDARN) radars. This work analyzed digital beamforming and waveform design approaches that would be enabled by the adoption of a SDR based radar design and found that these techniques could improve the performance of SuperDARN radars. This work also developed a prototype receiver to demonstrate the feasibility of a SDR based SuperDARN radar. The hardware selection for this receiver leveraged low-cost commercial off-the-shelf software defined radios and amplifier designs supplemented by custom filters. The software implementation utilized GNU Radio, an open source SDR and signal processing platform, to process and record receiver data. A prototype was successfully designed and constructed using the Red Pitaya software defined radio. This prototype included a 4 channel receiver which was evaluated in the laboratory setting and tested at the Blackstone, Virginia radar site. A comparison of results from the prototype receiver and the existing hardware showed promise for the use of this platform in future ionospheric research.

Design of Software Defined Radio for SuperDARN Radars

Paul Steven Kennedy

GENERAL AUDIENCE ABSTRACT

Software defined radio (SDR) is a rapidly developing field which uses software to perform radio signal processing traditionally accomplished by hardware components. Software defined radio has been used extensively in communication systems due to its flexibility and cost effectiveness. Recently, SDR has been incorporated into radar systems, particularly for space science research. This study investigated the benefits and design of a SDR receiver for the next generation of Super Dual Auroral Network (SuperDARN) radars. This work analyzed radar design approaches that would be enabled by the adoption of a SDR framework and found techniques that could improve the performance of SuperDARN radars. This work also developed a prototype receiver using low-cost commercial off-the-shelf software defined radios to demonstrate the feasibility of a SDR based SuperDARN radar. A prototype was successfully designed and constructed using the Red Pitaya software defined radio. This prototype was evaluated in the laboratory setting and tested at the Blackstone, Virginia radar site. A comparison of results from the prototype receiver and the existing hardware showed promise for the use of this platform in future space science research.

Acknowledgments

To my advisors, Mike and Jo, for supporting and guiding me throughout my graduate program. Thank you for believing in me and giving me the opportunity to join the SuperDARN community.

To Dr. Earle, for his support as a committee member and for introducing me to research early on in my undergraduate education.

To Dr. McGwier, for his support as a committee member and his passion for research.

To Kevin Sterne, for supporting my research and answering my many questions.

To the Virginia Space Grant Consortium, for engaging me in STEM as a high school student, undergraduate research fellow, and graduate research fellow.

To the National Science Foundation, for their support of the SuperDARN research group.

To the Bradley Department of Electrical and Computer Engineering, for their support throughout my education at Virginia Tech.

To my friends, roommates, and fellow students, thank you for being my Virginia Tech family.

To God, for blessing me with all the opportunities that led me to this point.

And of course, to my parents, Pat and Jen, for their unconditional love and support, for introducing me to engineering, and for raising me to be a Hokie.

Table of Contents

Chapter 1. Introduction.....	1
1.1 Introduction	1
1.2 SuperDARN	2
1.3 Radar Basics.....	4
1.4 Coherent Ionospheric Radar.....	8
1.5 Software Defined Radio	13
1.6 Research Questions and Structure.....	15
Chapter 2. Potential Benefits of SDR in SuperDARN Radar.....	16
2.1 Digital Beamforming.....	16
2.1.1 Null-Steering Technique	21
2.1.2 Windowing Approach.....	24
2.1.3 Imaging Radar.....	28
2.2 Advanced Waveforms	31
2.2.1 Multiple Beam and Frequency Division Multiplexing Scan Modes	31
2.2.2 Directional Filtering.....	32
2.2.3 Frequency Multiplexing and Channelizer Design	34
2.2.4 Cognitive Radar and Adaptive Waveforms	38
Chapter 3. Prototype Development	42
3.1 Red Pitaya Selection.....	43
3.2 Red Pitaya Impedance and Modification	46
3.3 Red Pitaya Characterization	47
3.4 Cross-Talk Issue and Analysis	53

3.4.1	Effect of Cross Talk on Broadside Radiation	56
3.4.2	Adjacent Pairing Approach.....	59
3.5	Front End Design	64
3.5.1	Preselection Filter	65
3.5.2	LNA Selection	67
3.5.3	PCB Design and Implementation.....	67
3.5.4	Cascade Analysis	69
3.6	Receiver Synchronization	71
3.6.1	Calibration Signal	71
3.6.2	Magnitude Calibration	73
3.6.3	Coarse Alignment in Time.....	75
3.6.4	Phase Synchronization	78
3.6.5	Long-Term Stability of Cancellation Ratio	79
3.6.6	Clock Distribution for Multiple Channel Synchronization.....	82
3.7	Test Results from Blackstone Radar	86
Chapter 4.	Future Work and Conclusions	92
4.1	Future Work	92
4.2	Conclusions	93
References	95
Appendix A – Cross Talk Analysis	99
A.1	Opposite Pairing Approach.....	99
A.2	Half Pairing Approach	100

List of Figures

Figure 1.1. Distribution of SuperDARN Radar Sites [4].....	2
Figure 1.2. Radar Field-of-View Plot [4].....	3
Figure 1.3. SuperDARN Antenna Array in Holmwood SDA, Saskatoon [6]	4
Figure 1.4. Simple Radar Pulse Sequence	6
Figure 1.5. Possible Ray Paths in the Ionosphere [4]	9
Figure 1.6. SuperDARN 8-Pulse “katscan” Sequence.....	12
Figure 1.7. Traditional Superheterodyne Architecture [13].....	14
Figure 1.8. Replacement of Analog Hardware with Software [13]	14
Figure 2.1. Traditional Beamforming Architecture for Receive and Transmit Paths.....	17
Figure 2.2. Digital Beamforming Architecture for Receive and Transmit Paths	18
Figure 2.3. Array Factor for 16 Element Linear Antenna Array	19
Figure 2.4. Cascaded Array Factors for Standard Beamsteering.....	20
Figure 2.5. Comparison of Standard Beamforming and Null-Steering Approaches	23
Figure 2.6. Main Lobe of Cascaded Antenna Patterns	23
Figure 2.7. Rectangular Windowing Function.....	25
Figure 2.8. Hamming Windowing Function	26
Figure 2.9. Effects of Various Windows on Antenna Gain, Sidelobes, and Beamwidth	27
Figure 2.10. Array Factors and Interference for N=2 Beams	32
Figure 2.11. Array Factors and Interference for N=4 Beams	33
Figure 2.12. RF Channelizer Input Signal	35
Figure 2.13. Channelizer Outputs	36

Figure 2.14. Ray Tracing for an IRI Model Ionosphere at 10 MHz, 11 MHz, and 12 MHz [4] .	37
Figure 2.15. Comparison of Pulse Waveforms	39
Figure 2.16. Comparison of Range Resolution.....	40
Figure 3.1. Red Pitaya STEMLab 125-14 [21]	44
Figure 3.2. Block Diagram of Red Pitaya Digital Frequency Conversions [22]	45
Figure 3.3. Minimum Discernable Signal vs Frequency for Modified and Unmodified Designs	47
Figure 3.4. Noise Figure vs. Frequency	48
Figure 3.5. 1 dB Compression Point.....	49
Figure 3.6. Third Order Intercept Point vs Frequency	50
Figure 3.7. SFDR vs Frequency.....	51
Figure 3.8. Transmit Power vs. Frequency	52
Figure 3.9. Third Order Intercept Point vs. Frequency	53
Figure 3.10. Effect of Cross Talk on Array Factor for $\phi = 90^\circ$	57
Figure 3.11. Effect of Windowing on Array Factor for $\phi = 90^\circ$	58
Figure 3.12. Effect of Cross Talk on Adjacent Pairing Scheme	59
Figure 3.13. Variation with Respect to Beam Direction for Adjacent Pairing	62
Figure 3.14. Array Factors for Adjacent Pairing Approach.....	63
Figure 3.15. Modified Superheterodyne Block Diagram for Direct Conversion SDR [13]	64
Figure 3.16. Bandpass Preselection Filter.....	66
Figure 3.17. Frequency Response of Filter Insertion Loss (Blue) and Return Loss (Magenta) ..	66
Figure 3.18. Front End PCB Design	68
Figure 3.19. Assembled Front End Design.....	68
Figure 3.20. Front End Frequency Response.....	69

Figure 3.21. Cascade Analysis.....	70
Figure 3.22. Calibration Pulse Magnitude	72
Figure 3.23. Demonstration of Magnitude and Coarse Time Errors	73
Figure 3.24. Magnitude Calibration Time Interval.....	74
Figure 3.25. Calibration Signals with Magnitude Corrections	75
Figure 3.26. Cross Correlation Analysis of Delay Time	76
Figure 3.27. Magnitude of Calibration Signal After Coarse Alignment.....	76
Figure 3.28. Synchronization of Transition Edges After Coarse Alignment.....	77
Figure 3.29. Sample by Sample Measurement of Transition Edge After Coarse Alignment.....	77
Figure 3.30. Phase Difference vs Time.....	78
Figure 3.31. Phase Difference vs Time of Synchronized Signals.....	79
Figure 3.32. Cancellation Ratio After Synchronization.....	80
Figure 3.33. Cancellation Ratio vs Time	81
Figure 3.34. Clock Distribution Board Layout	84
Figure 3.35. Two Pulse Sequences Shown in Single Receiver Data	87
Figure 3.36. Synchronization of Receive Channels.....	87
Figure 3.37. Synchronization of Recorded TX and RX Signals.....	88
Figure 3.38. Digital Receiver Blanking	89
Figure 3.39. Range Time Intensity Display of Prototype Data.....	90
Figure 3.40. Range Time Intensity Display of Main Array Data	90
Figure A.1. Array Factors for Opposite Pairing Approach.....	99
Figure A.2. Effect of Cross Talk on Opposite Pairing Scheme	100
Figure A.3. Antenna Factors for the Half Pairing Approach.....	101

Figure A.4. Effect of Cross Talk on Half Pairing Scheme	103
Figure A.5. Variation with Respect to Beam Direction for Half Pairing	104
Figure A.6. Effect of Cross Talk on Half Pairing Approach	105

List of Tables

Table 3.1. Reduction of Maximum Range Due to Cross Talk.....	60
Table A.1. Antenna Element Weights for $\phi = 60^\circ$	102

Chapter 1. Introduction

1.1 Introduction

The invention of the radio by Guglielmo Marconi changed the way we communicate across the globe. Half a century later, the invention of the transistor radio once again revolutionized communications by making radios compact and portable. Today, the availability of low cost electronics has enabled software defined radios to bring a new wave of advancement to radio engineering. Many applications have been developed for commercial communications to accommodate multiple communication standards and modulation schemes while maximizing the efficiency of spectrum usage. Software radio technologies also open the door to new techniques for radar design, particularly in phased array radars. One potential use case is the Super Dual Auroral Radar Network (SuperDARN) collaboration's network of coherent high frequency (HF) radars due to the unique challenges of ionospheric radar design.

This thesis presents several techniques for improving SuperDARN radar performance and a prototype demonstrating the feasibility of a software defined SuperDARN radar. This introductory chapter provides background information referenced throughout this work. Section 1.2 describes the goals and design of the SuperDARN collaboration. Section 1.3 presents radar fundamentals used in the analysis of potential new techniques and the inherent tradeoffs of radar design. Section 1.4 summarizes the theory of operation for SuperDARN radars and addresses the unique aspects of ionospheric radar. Section 1.5 provides a brief background on software defined radios and how they differ from traditional hardware radios. Section 1.6 states the thesis objectives and organization.

1.2 SuperDARN

The Super Dual Auroral Radar Network is an international collaboration of over 30 radars designed to study plasma in the ionosphere, a region of Earth's upper atmosphere from about 60 to 1,000 km in altitude containing high concentrations of charged particles [1] [2] [3]. The ionosphere plays a critical role in understanding the risks to electrical power grids, communication systems, satellite based navigation systems such as GPS, and radiation hazards for spacecraft due to space weather. Understanding how plasma flows in the ionosphere provides the information needed to model the ionosphere's response to the solar wind and interplanetary magnetic field. The primary focus of SuperDARN is collecting data on the plasma convection patterns in the high latitude regions of the ionosphere [1]. Figure 1 shows the coverage of the SuperDARN network over mid to polar latitudes as well as the many nations collaborating towards this objective.

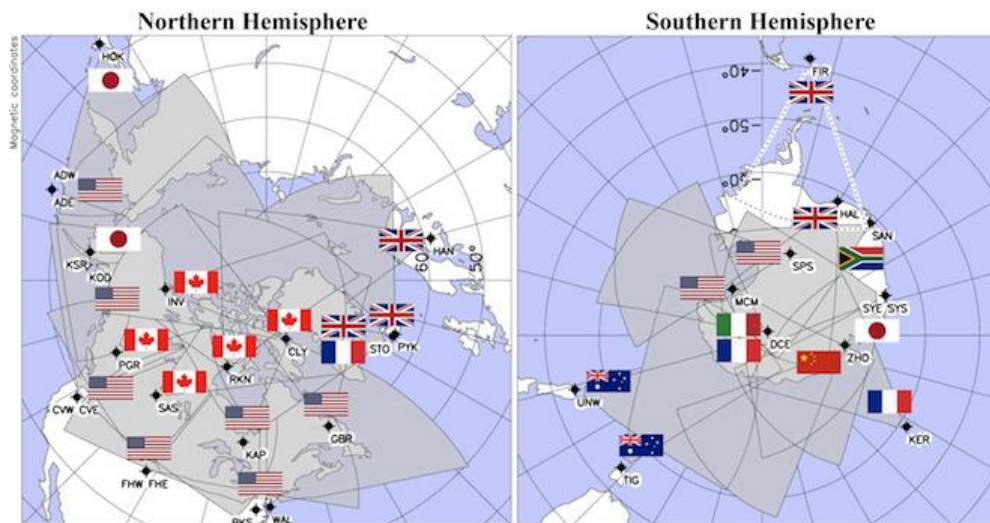


Figure 1.1. Distribution of SuperDARN Radar Sites [4]

Each radar site consists of a 16-element antenna array connected to analog beamformers and a single transceiver. The constructive interference between array elements forms a beam of focused radiated energy which determines the look direction of the radar. This beam is then sequentially steered across the radar field of view, producing measurements as a function of range and direction as shown in Figure 1.2.

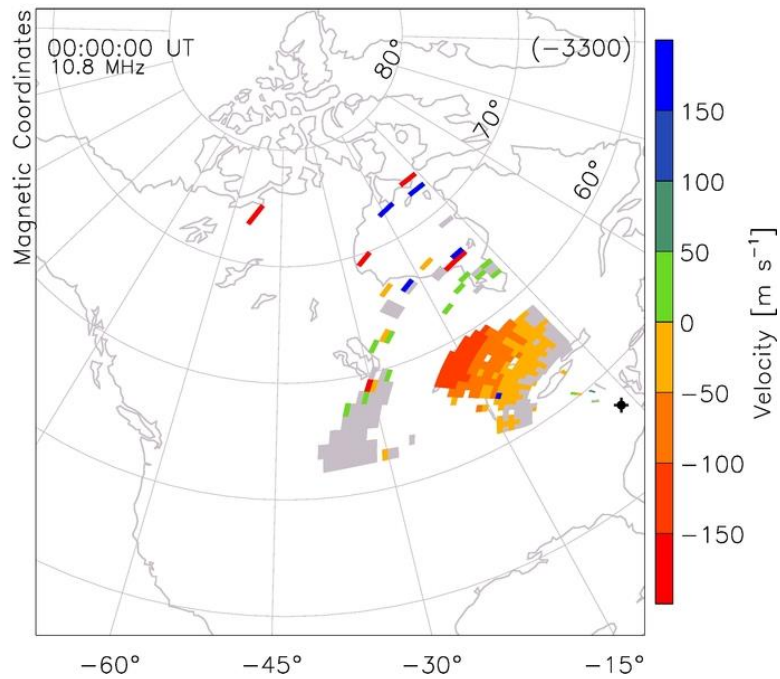


Figure 1.2. Radar Field-of-View Plot [4]

The color indicates the measured velocity of the radar targets. In the case of the SuperDARN radars, the targets are irregular density structures in the ionosphere and backscatter from the Earth's surface. This velocity information is then used in the mapping of the plasma convection pattern.

The antenna elements may be either log periodic dipole arrays or twin terminated folded dipoles depending on the particular site [5]. Both of these antenna options offer a wide bandwidth such that a range of frequencies can be used depending on propagation conditions in the ionosphere

and spectrum usage by interfering sources of radio waves. Figure 1.3 shows a SuperDARN array at Holmwood, Saskatoon using log periodic dipole arrays as the antenna elements. The 16 antenna elements seen in the main array are connected to radio hardware in the building seen in the center of the array. Additionally, a 4-element interferometry array is seen behind the main array and can be used to obtain elevation angle information.



Figure 1.3. SuperDARN Antenna Array in Holmwood SDA, Saskatoon [6]

Currently, SuperDARN radar sites operate as monostatic radars such that the transmitter and receiver are collocated. Future iterations of SuperDARN radars may operate as bistatic or multistatic systems, but the radar fundamentals presented in this work are discussed only for monostatic systems.

1.3 Radar Basics

The origins of radar are usually traced back to World War II and the Chain Home early warning radar which was instrumental in the Battle of Britain. Even earlier than World War II, similar technologies were used in ionospheric studies such as the ionosonde invented by Gregory Breit and Merle Tuve in 1925 [7]. All radar systems share the same basic operating principle. First, a transmitter generates electromagnetic waves which propagate outwards towards a target. The

interaction between these waves and the target produces a backscattered echo. This echo is then observed by a receiver. Comparing the backscattered echo with the transmitted signal then provides information about the target. In the case of SuperDARN radars, the desired information includes the presence, position, and velocity of the target.

The detection portion of radar (RAdio Detection And Ranging) is determined from the presence or absence of received power (P_r). A detection threshold differentiates between the presence of a target and random thermal noise power. The expected power is determined by the radar range equation shown in the Equation 1 below where P_t is the transmitted power, G is the antenna gain, λ is the wavelength, σ is the radar cross section of the target, and R is the range of or distance to the target [8].

$$P_r = \frac{P_t G^2 \lambda^2 \sigma}{(4\pi)^3 R^4} \quad (1.1)$$

The target position is represented by the range and direction to the target relative to the radar position. The range is determined from the time delay (t) of the echo from the transmitter to the receiver. The range and time delay are related by the propagation velocity of the radio wave which is taken to be the speed of light (c) as shown in Equation 2 below:

$$R = \frac{ct}{2} \quad (1.2)$$

The factor of two is a result of the radio wave travelling twice the distance to the target as it travels from the transmitter, to the target, and back again. The direction of the antenna beam when a detection occurs provides the directional information of the target. The antenna beam orientation is measured in both azimuth and elevation which, combined with the target range, gives the relative position of the target.

The range and direction of the target are not exactly known due to instrumental limitations on the resolution of the measurements. The azimuthal beamwidth of the antenna determines the azimuthal resolution of the radar. Likewise, the elevation resolution is determined by the beamwidth of the antenna in elevation. In the case of the SuperDARN radars, the linear main array only provides azimuthal information unless combined with information from the interferometry array to determine the elevation angle. The waveform design determines the range resolution of the radar [8].

In a pulsed Doppler radar, the radar transmits a sequence of pulses transmitting energy and an interpulse period without radiated power. Figure 3 shows a sample pulse sequence where the duration of a single pulse is given as τ and the time between the start of subsequent pulses is the Pulse Repetition Interval (PRI). The inverse of the PRI is referred to as the Pulse Repetition Frequency (PRF).

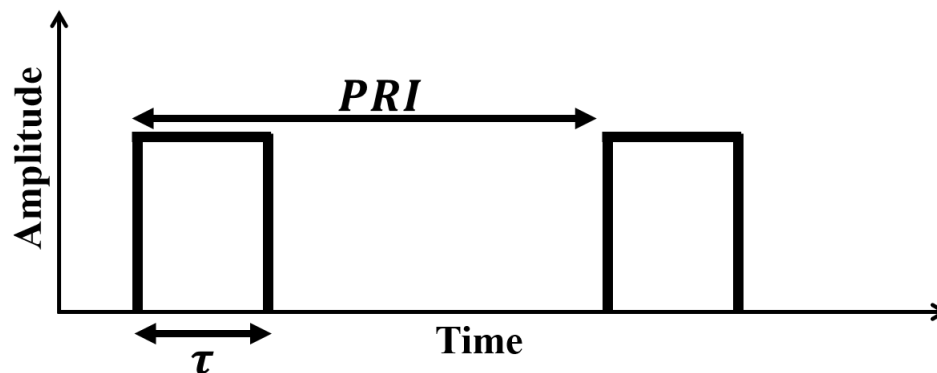


Figure 1.4. Simple Radar Pulse Sequence

The pulse length determines the range resolution (ΔR) of the radar as shown in Equation 3 below:

$$\Delta R = \frac{c\tau}{2} \quad (1.3)$$

The target velocity is obtained from the phase information of a pulsed Doppler radar. As suggested by the name, the velocity information is obtained by measuring the Doppler effect on the received waveform. For a stationary radar, any target with motion along the radar line-of-sight will impart a frequency shift on the backscattered echo. This frequency shift is called the Doppler frequency (f_d) and is directly proportional to the relative velocity (v_r) of the target:

$$f_d = \frac{2v_r}{\lambda} \quad (1.4)$$

The Doppler frequency is obtained from radar data by examining the phase information between subsequent pulses. Using a quadrature receiver architecture, both the amplitude and phase (ϕ) information of the backscattered echo are preserved. The Doppler frequency is then calculated from the change in phase between each pulse in the radar sequence:

$$f_D = \frac{1}{2\pi} \frac{d\phi}{dt} \quad (1.5)$$

Ambiguities are introduced if the Nyquist sampling theorem is violated due to large phase change between two pulses. Since the time between pulses is given by the PRF, the maximum unambiguous Doppler shift and Doppler velocity can be expressed as a function of the PRF:

$$f_{d,ua} = \frac{PRF}{2}, \quad v_r = \pm \frac{\lambda PRF}{4} \quad (1.6)$$

Recalling that the maximum unambiguous range is inversely proportional to the PRF, there is an inherent tension between achieving a long maximum unambiguous range and a high maximum unambiguous velocity. Much of radar waveform design is focused on techniques to circumvent this issue.

Increasing the number of pulses appears to be a simple method for increasing the received power without affecting the positional resolution. However, for a fixed range ambiguity, increasing the number of pulses negatively affects the temporal resolution or refresh rate of the radar. In the case of SuperDARN radars, plasma convection patterns are dynamic and a higher refresh rate is beneficial for understanding how changes in the plasma flows happen. A high refresh rate ensures that brief features in the convection are observed. The update rate for the entire radar field-of-view is usually 1-2 minutes in the SuperDARN radars and is a function of the dwell time on each beam and the number of beams required to completely scan the radar field-of-view [4].

1.4 Coherent Ionospheric Radar

Utilizing radar for the purpose of ionospheric measurements requires a unique set of considerations. First, the propagation of the emitted radio wave is altered by charged particles present in the ionosphere. The ionosphere is formed by several layers ordered by altitude with varying properties of particle composition, density, velocity, and temperature. The refraction of a propagating electromagnetic wave through the ionosphere depends on the frequency of the wave and the free electron density in the ionosphere. Since the free electron density varies with altitude, the refractive index varies with altitude [9].

Satellite communications typically use higher frequencies such as X band (8-12 GHz) in order to minimize the change in refractive index and penetrate through the ionosphere. On the other hand, amateur radio operators utilize lower frequencies such as the HF (3-30 MHz) spectrum and leverage the ionosphere's properties to enable non-line-of-sight (LOS) communications [9].

Typical LOS communications are limited by obstacles or the curvature of the Earth preventing a clear path from transmitter to receiver. A sky wave propagation mode takes advantage of the change in refractive index in the ionosphere to "reflect" radio waves off the ionosphere

redirecting them to receivers at great distances. This effective reflection occurs when the upward propagating wave encounters a transition to a layer of sufficiently high density to refract the wave to propagate downwards. Figure 5 presents the various paths a radar signal may take through the ionosphere. Shallow incidence angles result in refraction back towards Earth, while sharp incidence angles result in penetration of the ionosphere.

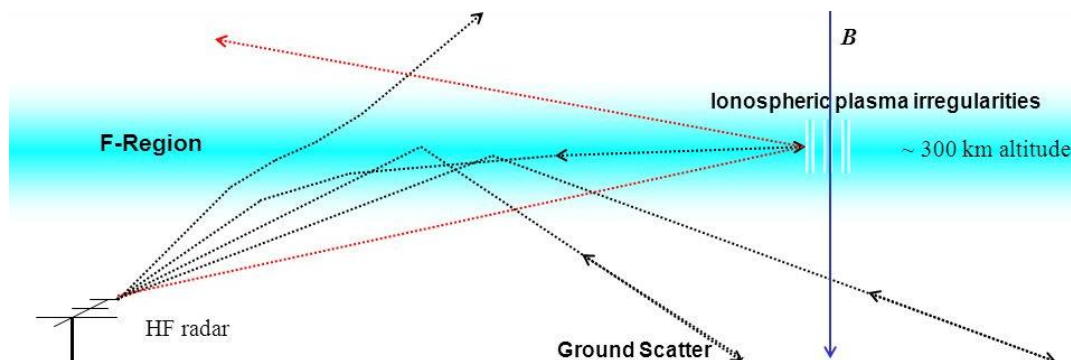


Figure 1.5. Possible Ray Paths in the Ionosphere [4]

Since the Earth's ground is also conductive, the radio waves can reflect off the Earth's surface allowing "multi-hop" operation. Multi-hop operation occurs when the radio wave is reflected by the ionosphere more than once. SuperDARN radars also operate in the HF frequency range both to detect small-scale plasma density variations known as ionospheric irregularities, and to take advantage of multi-hop propagation modes. Structures in the ionosphere or on the ground function as targets for the radar and produce backscattered echoes.

In most radar systems, echoes from the ground and other stationary objects are considered to be clutter and diminish the signal quality in the system. In SuperDARN systems, ground scatter can provide valuable information on propagation and ionospheric conditions. For instance, the reliable and continuous presence of ground scatter targets during daytime enables the detection of short-wave fadeout events when the sky wave propagation mode is lost due to the onset of

heavy absorption in the ionosphere. Nevertheless, the primary targets needed for mapping plasma convection patterns are due to ionospheric irregularities.

SuperDARN radars operate as coherent scatter ionospheric radars [2]. These coherent scatter radars measure echoes from irregularities in electron density which have spatial scales comparable to the radar operational wavelength. The local variation in electron density produces a small fluctuation in the permittivity of the medium. When excited by the incident radio wave, a polarization fluctuation is produced which leads to a displacement current density. This current density results in reradiated energy in the form of radar echoes. The equivalency between the spatial scale of the irregularity and the radar wavelength is important for constructive interference to occur. When the irregularity has a wavelength equal to one-half of the radar wavelength, Bragg or coherent scatter occurs [2].

Due to the nature of coherent scatter from ionospheric irregularities, the target radar cross section (σ) cannot be treated the same way as the “hard” or discrete target assumed previously when the radar range equation was introduced. A discrete target has a definite cross sectional area regardless of the radar operating parameters. In contrast, a “soft” or beam-filling target such as rain or ionospheric irregularities are dispersed throughout the entirety of the beam and range gate. Thus, a larger range gate will result in more backscattered power because there will be more target material. Therefore, the radar cross section of a beam-filling target depends on other radar parameters. The radar range equation can be modified using a volumetric radar cross section which reduces to the modified radar range equation shown below where A represents the effective area of the receive antenna and σ_v represents the volumetric cross section of the scattering target [10]:

$$P_r = \frac{P_t A \sigma_v \Delta R}{4\pi R^2} \quad (1.7)$$

One important difference in this version of the radar range equation is the diminished effect of range on the received power. Previously, the received power was inversely proportional to the quartic of range. Now, the power decreases as the square of the range. The antenna gain, which is proportional to the effective antenna area (A), is also less important to the received power since a wider beam reflects off more target material. However, the antenna beamwidth is still important for determining the azimuthal resolution of the radar. Additionally, a tradeoff is introduced between the received power and the range resolution of the radar.

Ionospheric irregularities are an overspread target medium meaning that a single inter-pulse period sufficiently long to resolve range without ambiguity cannot simultaneously measure the target's speed without ambiguity. In other words, a traditional pulsed Doppler radar cannot achieved the necessary unambiguous range and velocity needed to characterize the medium. Instead, a different waveform design must be used [11].

To overcome the short correlation time of the medium, SuperDARN and other ionospheric radars utilize multi-pulse sequences. In a multi-pulse sequence, each pulse has a different spacing or lag compared to the other pulses, and multiple pulses occur within a single pulse sequence. The phase difference information from each lag combination in the sequence can then be used to calculate the Doppler velocity while maintaining the low PRF required to achieve a high unambiguous range. This sequence works on the assumption that echoes from different ranges are uncorrelated [11]. Figure 6 shows an example of a multipulse sequence used in SuperDARN radars. Each pulse pair uses a different lag spacing, and no lag combination is repeated.

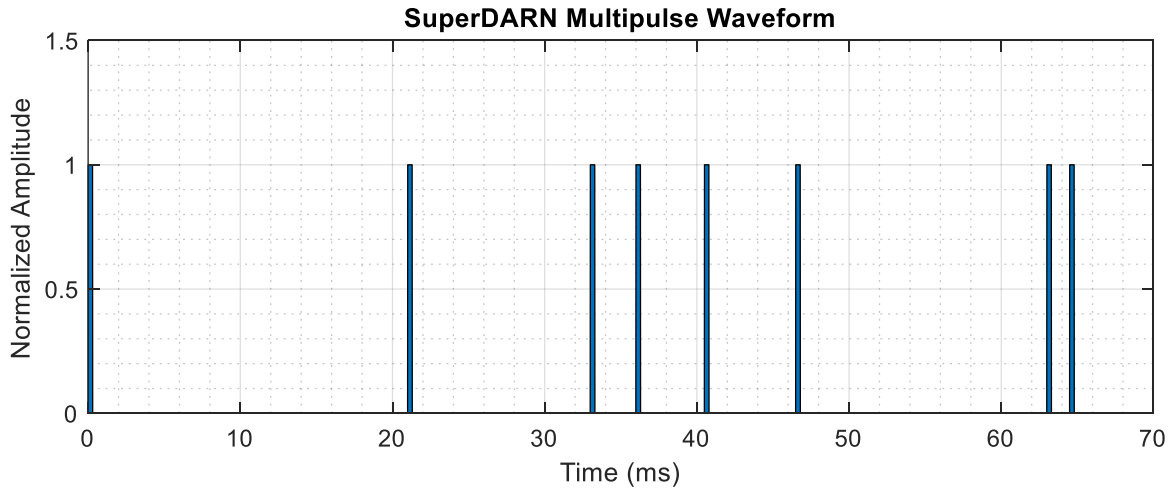


Figure 1.6. SuperDARN 8-Pulse “katscan” Sequence

The multi-pulse sequence does come with tradeoffs. The inclusion of multiple pulses can introduce a range ambiguity as a received echo may have been generated by any one of these pulses. This issue is overcome through coherent integration of multiple pulse sequences. Through this process, the correlated echoes corresponding to the correct range gate experience coherent integration gain and the uncorrelated cross range echoes are suppressed [11]. However, any repetition of lag pairs will result in a range ambiguity. Conversely, any missing lag pairs will contribute to spectral ambiguity. Due to hardware constraints, the transmitter and receiver cannot be operating at the same time as the high transmitted power would damage the sensitive receiver components. In a multi-pulse sequence, this means that the receiver is blanked with heavy attenuation during the times when the radar is transmitting a pulse. This issue, known as receiver blanking, can cause missed detections of individual pulse returns. Through careful design of the pulse sequence, the extent of the receiver blanking issue can be minimized such that another pulse within the sequence is likely to detect the target. Thus, waveform design is an important factor in determining the performance of a SuperDARN radar.

1.5 Software Defined Radio

Radio frequency (RF) design has experienced rapid growth corresponding to the evolution of low cost electronics and the growing popularity of software defined radios. Joe Mitola first used the phrase *software radio* in 1991 to refer to a class of reprogrammable or reconfigurable radios [12]. Alternatively, Dr. Jeffrey Reed asserts, “a good working definition of a software radio is a radio that is substantially defined in software and whose physical layer behavior can be significantly altered through changes to its software” [12]. Thus, the flexibility of software defined radio, in the sense that its functionality can be reconfigured, is a central attribute of software radio. This flexibility is paramount for accommodating the rapid changes in communication standards and the need for multiple modulation schemes. A reconfigurable system permits adaptive or cognitive systems to change their operating characteristics in response to their environment, and allows a single device to achieve the functionality of several devices. As Reed notes, this enhanced flexibility is accomplished by replacing hardware components with digitization and digital signal processing [12].

Ideally, digitization would occur immediately following the antenna, but this approach is not practical for radio frequency signals. Instead, software radio architectures begin with the traditional superheterodyne approach and implement components in the digital domain using software. Figure 7 shows the architecture of an analog superheterodyne receiver.

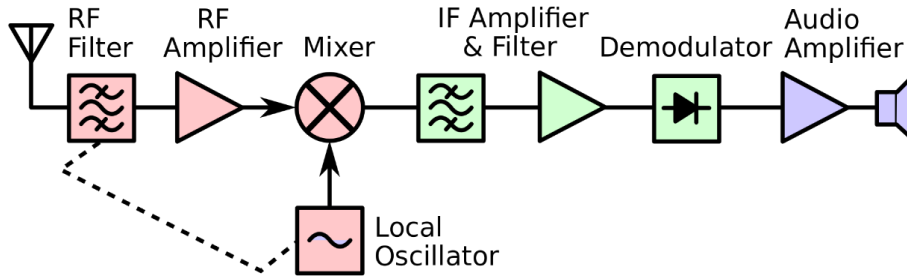


Figure 1.7. Traditional Superheterodyne Architecture [13]

In this architecture, the signal processing is broken down into a radio frequency (RF) stage and an intermediate frequency (IF) stage. The RF stage, shown in red, consists of all the parts after the antenna up to and including the mixer. In this stage, hardware components perform filtering, amplification, and frequency conversion at a tunable frequency corresponding to the desired signal. After the mixer performs a frequency conversion, additional signal processing and demodulation is performed at the fixed IF frequency. In software radio architectures, some elements of the demodulation, IF signal processing, or frequency conversion are implemented in the digital domain as shown in Figure 8.

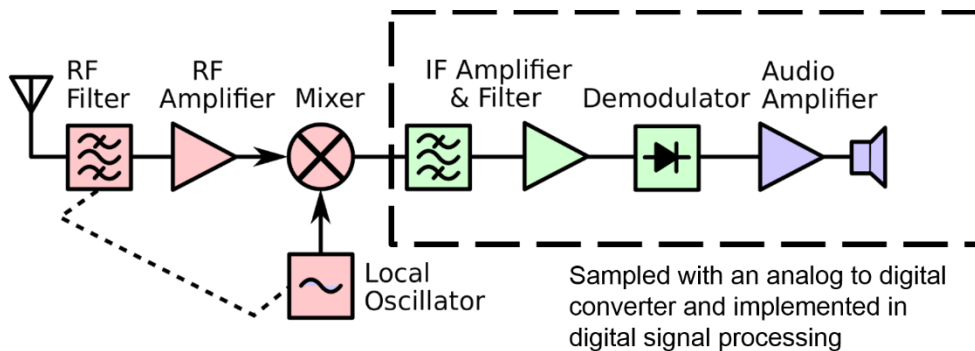


Figure 1.8. Replacement of Analog Hardware with Software [13]

Software radio architectures that eliminate the need for analog mixers are referred to as direct conversion architectures. While direct conversion is often impractical for traditional radars operating in the GHz regime, HF radars can be implemented using direct conversion with an analog to digital converter with a high sampling rate. A future SuperDARN software defined radar would likely utilize a direct conversion architecture.

1.6 Research Questions and Structure

This thesis focuses on two broad questions relating to software defined radio use in SuperDARN radars. First, what potential radar performance benefits would a software defined radio approach provide? Second, what steps are necessary to implement a low-cost software defined radio architecture in a SuperDARN radar? The second chapter of this work explores the potential improvements to the azimuth, range, and temporal resolution of the radar that could be obtained using a SDR approach. Case studies are produced for radar performance using several techniques enabled by software defined radios. The third chapter of this work details the development of a hardware prototype and the unique challenges to building a software defined SuperDARN radar. A discussion of the results, proposed future work, and conclusions are offered in the fourth chapter.

Chapter 2. Potential Benefits of SDR in SuperDARN Radar

The first potential benefit of a software radio framework is improved directional resolution and reduced ambiguity. Sections 2.1, 2.2, and 2.3 examine improvements to directional ambiguity by using digital beamforming techniques to suppress sidelobe interference. Section 2.4 considers an imaging radar approach to improving directional resolution.

2.1 Digital Beamforming

The antenna array beamforming process determines the directional resolution, and the low cost of SDR enables the implementation of digital beamforming techniques. In an antenna array, like the arrays used by SuperDARN, phase delays (ϕ_n) corresponding to each antenna element control the direction of the main lobe of the antenna pattern. In traditional analog beamforming, this process is accomplished on receive using analog hardware to achieve the phase shifts and to sum the signals before passing the output to a single receiver as shown Figure 2.1. On transmit, a single transmitter generates the waveform, which is then divided and passed to each antenna element with the appropriate phase delays.

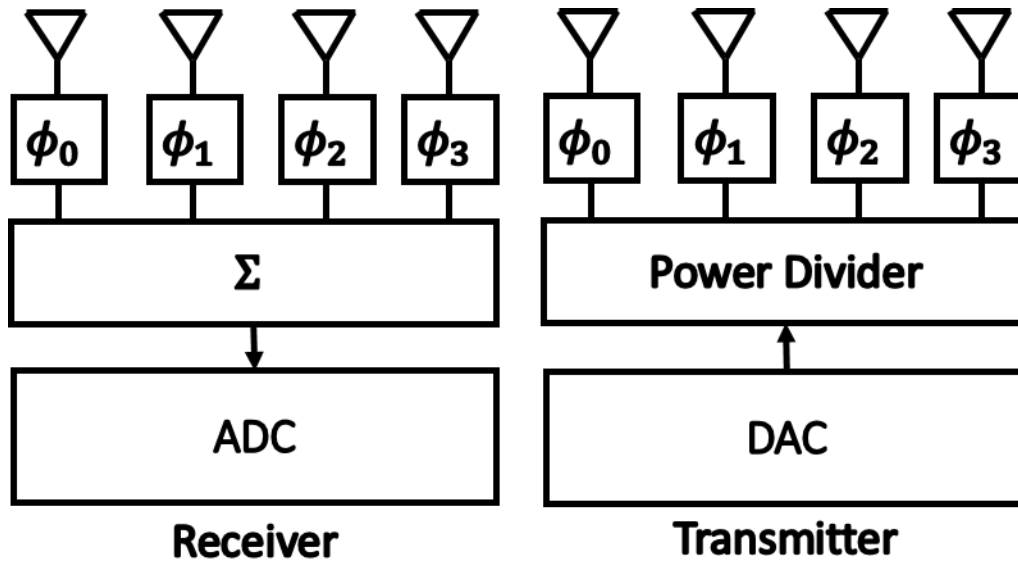


Figure 2.1. Traditional Beamforming Architecture for Receive and Transmit Paths

Each antenna element in the array is accompanied by an analog phase shifter. There are several ways to accomplish the phase shifting in an analog beamformer. The simplest option uses switched delay lines to reroute the signal through a transmission line with a length corresponding to the desired phase delay. This approach benefits from the simplicity of the design, but it limits the performance of the beamformer.

First, the relationship between transmission line length and phase delay is wavelength dependent. Thus, changes in frequency will alter the phase delay in the beamformer and will distort the resultant array factor. Additionally, the number of potential look directions must be predetermined in order to ensure that all requisite delay line length options are available in the design. In order to have a large number of look directions, the corresponding hardware then becomes relatively large or complex to account for all potential phase delays. At very low frequencies, the delay line lengths required may be prohibitively large requiring a more complex delay line design.

Alternatively, electronic phase shifters can be used to provide a variable phase delay based on a control signal input. This approach benefits from higher degrees of flexibility and precision due to the ability to select the desired phase shift electronically. Electronic phase shifters can also be smaller than delay lines, particularly at lower frequencies. However, phase shifters suffer from bandwidth limitations similar to the delay line approach.

Digital beamforming offers an alternative approach to the traditional delay lines and phase shifters. In a digital beamformer on receive, each antenna element in the array is sampled by a separate ADC. After quantization, phase delays are applied to each signal in the digital domain and the summation is also performed digitally. On transmit, each element is fed by a separate DAC and the phase delays are applied in the digital domain as shown in Figure 2.2.

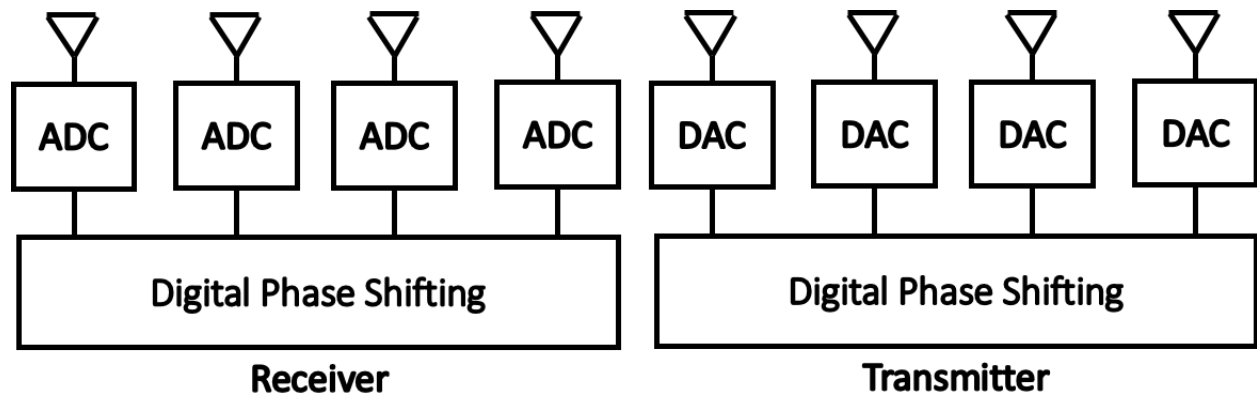


Figure 2.2. Digital Beamforming Architecture for Receive and Transmit Paths

This approach offers considerably greater flexibility and enables new methods of optimizing the array performance. The increase in signal processing complexity is offset by the reduction in electronic circuitry. The lack of electronic switches of phase shifters increases the reliability of the beamformer and improves the precision of the beamformer across a wide range of temperatures and frequencies.

Previously, the prohibitive cost of placing a transceiver on every antenna element made analog beamforming the preferred option. Continuous advancements in electronics design, the evolution of software defined radios, and the corresponding reduction in cost now enable the widespread implementation of digital beamforming techniques. Enabling digital beamforming techniques is one potential motivation for adopting a software radio architecture in future SuperDARN radars.

This work explored a number of potential processing methods in order to determine the potential system improvement as a result of adopting a digital beamforming approach. Using MATLAB, this work developed code to enable the analysis of a 16 element linear antenna array for various phase and amplitude weights. Using standard phase weighting, the corresponding array factor appears as shown in Figure 2.3.

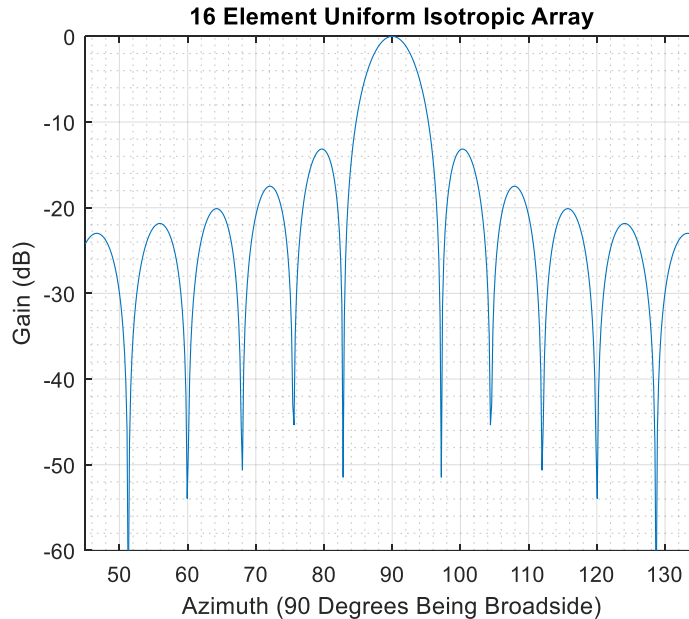


Figure 2.3. Array Factor for 16 Element Linear Antenna Array

One notable feature is that the highest sidelobe is only 13.2 dB below the peak of the main lobe. In a radar system, the varying radar cross section of different targets means that a large target in one of these sidelobes could obscure a smaller target in the main lobe or cause a false detection when there is no target present. An additional factor to consider is that the SuperDARN system is monostatic meaning the same antenna is used on both transmit and receive. Cascading the transmit and receive patterns produces the combined pattern shown in Figure 2.4.

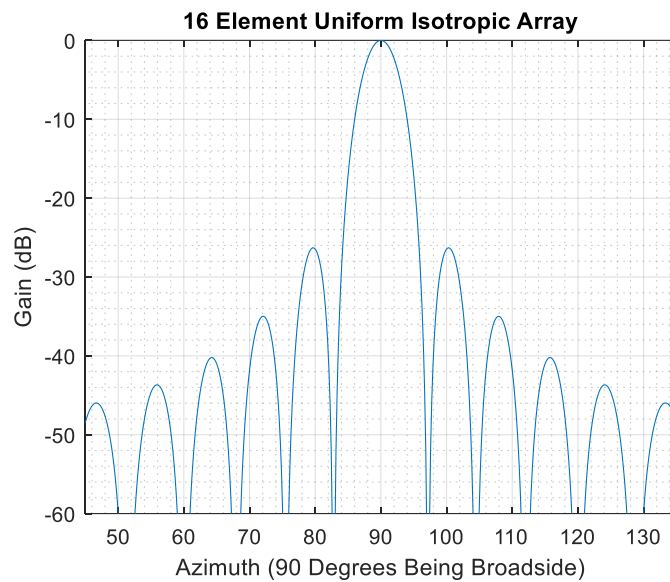


Figure 2.4. Cascaded Array Factors for Standard Beamsteering

The sidelobe attenuation from both patterns results in a peak sidelobe 26 dB below the main lobe peak. Examining the overall pattern, the sidelobes fall off quickly after the first sidelobe. Since the secondary sidelobes are far lower, reducing the first sidelobe could improve the radar performance even if it increases power in the lower sidelobes. Null-steering offers one potential method for the suppression of sidelobe interference.

2.1.1 Null-Steering Technique

Any antenna pattern contains a main lobe where radiation is desired, sidelobes where sources of interference may occur, and nulls where incoming power is rejected. Traditional beamforming typically focuses on the placement of the main lobe, but many modern applications have warranted extended focus on the placement of nulls. The typical advantage of a null-steering approach comes from placing nulls in the direction of known interference sources. In the case of SuperDARN radars, predetermined interference sources are minimal, but null-steering can be adapted to suppress sidelobe power.

Null-steering accomplishes null placement by modifying the phase and amplitude weights applied to each element of the antenna array. The weights of the traditional beamformer with main lobe peak in the direction of ϕ_0 are calculated as a function of antenna element number (n) according to the equation below [14]:

$$\mathbf{w}_0(n) = A_n e^{jn\pi \cos \phi_0} \quad (2.1)$$

In these weights, the direction of the main lobe is controlled by the phase delay from the complex exponential term, and the shape of the pattern is influenced by the amplitude weights (A_n) applied to each antenna element. Next, the weights corresponding to a traditional beamformer steering in the direction of a desired null at ϕ_1 are calculated according to the equation below [14]:

$$\mathbf{w}_1(n) = A_n e^{jn\pi \cos \phi_1} \quad (2.2)$$

These two sets of weights represent two beams with different main lobe directions. This new weighting vector is then scaled by a factor r and subtracted from the traditional weighting vector as shown in the equations below, where the superscript, H , represents the Hermitian transpose of the vector [14]:

$$r = \frac{(\mathbf{w}_1^H \cdot \mathbf{w}_0)}{\mathbf{w}_1^H \cdot \mathbf{w}_1} \quad (2.3)$$

$$\mathbf{w} = \mathbf{w}_0 - \mathbf{w}_1 \cdot r \quad (2.4)$$

Subtracting the weights corresponding to the null placement accomplishes null-steering by creating destructive interference in the radiation pattern in the direction of ϕ_1 . The scaling factor minimizes distortion of the radiation pattern in the desired main lobe direction of ϕ_0 .

This work used a null-steering approach to place a null in the direction of the right hand peak sidelobe on transmit and in the direction of the left hand peak sidelobe on receive. This type of steering requires doubled phase shifting hardware with the traditional delay line or analog phase shifter approaches to beamforming. In digital beamforming, this approach can be implemented by simply changing the values of the phase weights. The resulting combined antenna pattern using this asymmetric null-steering approach is shown in Figure 2.5.

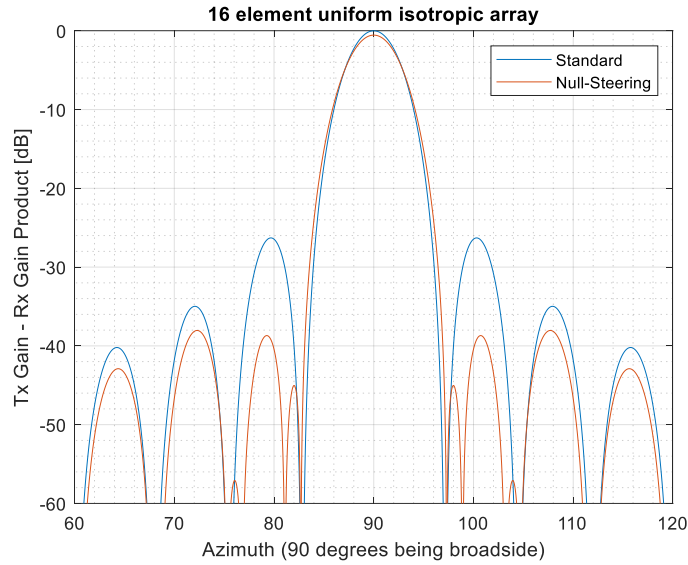


Figure 2.5. Comparison of Standard Beamforming and Null-Steering Approaches

This approach significantly reduces the peak sidelobe of the cascaded antenna pattern. With null steering, the peak sidelobe becomes three smaller sidelobes with a peak of -38 dB relative to the peak of the standard main lobe. However, this comes at the expense of a reduced main lobe peak for the null steering approach which is shown more clearly in Figure 2.6.

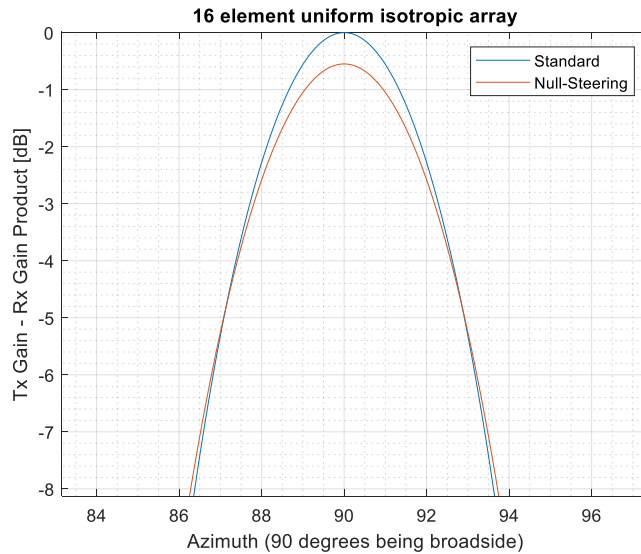


Figure 2.6. Main Lobe of Cascaded Antenna Patterns

As can be seen in the figure above, there is a 0.5 dB loss using the null-steering approach discussed above. Recalling the radar range equation, this loss in power or antenna gain results in a reduction in the system signal to noise ratio. Thus, the sidelobe interference improvement of the null-steering approach comes at the expense of the sensitivity of the radar system.

Ultimately, null-steering approaches to beamforming, enabled by SDR and digital beamforming, can reduce clutter and false detections by suppressing sidelobe interference at what appears to be a minor cost in terms of sensitivity.

2.1.2 Windowing Approach

Windowing offers another approach to sidelobe suppression in antenna arrays. The usage of windowing functions to mitigate sidelobe interference is a standard practice in digital signal processing and offers another tool for improving the radar performance. In spectral analysis, applying a Fourier transform to a signal of finite length results in spectral leakage which appears as sidelobes in the frequency domain. Windowing mitigates spectral leakage by applying a tapered weighting function across the signal deemphasizing the discontinuities at the ends of the finite length signal [10]. In phased arrays, each element of the finite length antenna array is a sample in space of the incident wave analogous to the time domain samples used for spectral analysis. Thus, many of the same spectral processing techniques can be applied to phased arrays. The sampling nature of phased arrays also gives rise to the traditional half-wavelength spacing between array elements to satisfy the Nyquist sampling theorem.

A wide variety of windowing functions exist, each with varying degrees of sidelobe suppression, mainlobe widening, and scalloping loss. A traditional SuperDARN beamformer with no windowing applied is effectively a 16 point rectangular windowing function with one point for each element of the antenna array. Using the paradigm of spectral analysis, the time and frequency domain effects of a 16 point rectangular window are shown in Figure 2.7.

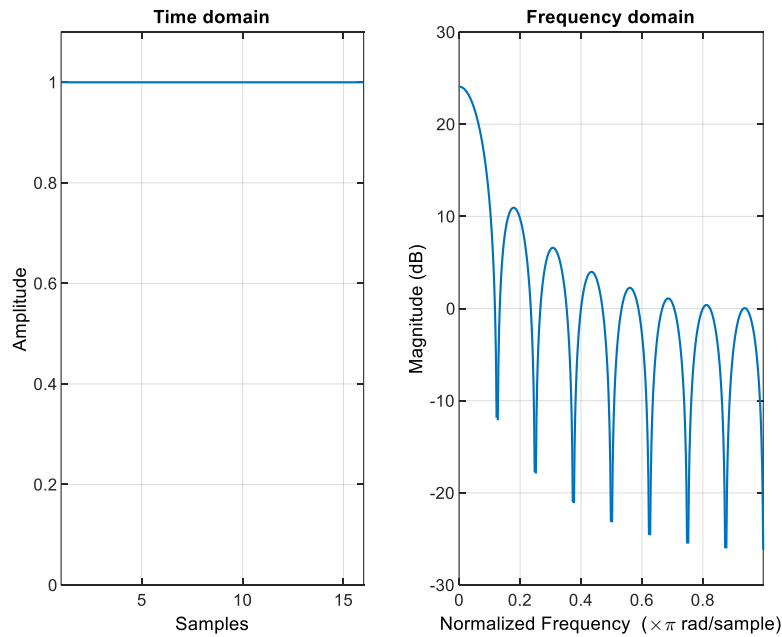


Figure 2.7. Rectangular Windowing Function

Each point is weighted equally resulting in a sharp discontinuity at the end of the sample. The frequency domain plot shows a peak power magnitude of 24.1 dB corresponding to the integration gain of 16 samples. It also shows a mainlobe 3 dB width of 0.11π rad/sample and a peak sidelobe power of -13.2 dB. This integration gain and -13 dB sidelobe power are familiar from the array factor figure. This same result occurs because spectral analysis with a rectangular windowing function is equivalent to the traditional beamforming process. An alternative windowing process using a Hamming window is shown in Figure 2.8.

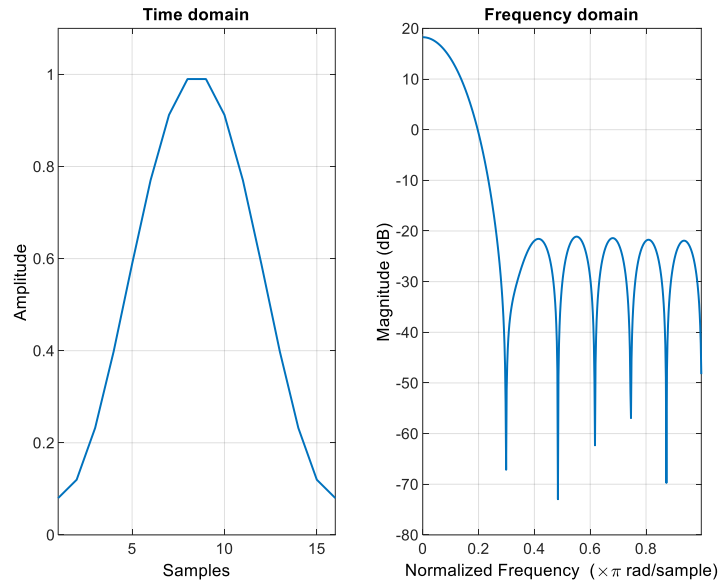


Figure 2.8. Hamming Windowing Function

In the time domain, the Hamming window sharply tapers the edges of the sampling interval in order to reduce spectral leakage. Due to the tapering, some of the integration gain is lost as shown by a peak power of only 18.2 dB. The mainlobe is also much wider with a 3 dB width of 0.16π rad/sample. The advantage of the Hamming window comes from a sharply reduced peak sidelobe level of -39.4 dB relative to the main lobe. Each windowing function utilizes a different tapering scheme to achieve a different tradeoff between loss of integration gain, main lobe broadening, and sidelobe suppression. This work explored several windowing functions for SuperDARN phased arrays, and select results of windows applied to a 16 element linear array of isotropic elements are shown in Figure 2.9.

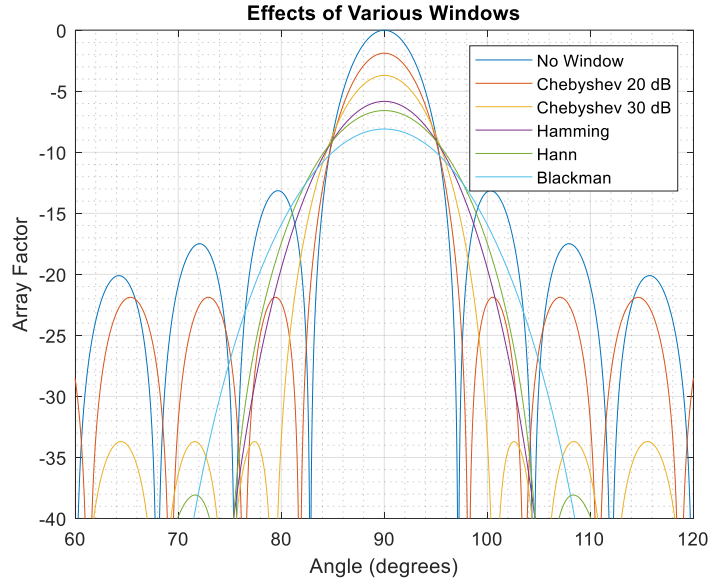


Figure 2.9. Effects of Various Windows on Antenna Gain, Sidelobes, and Beamwidth

As seen in the figure above, one fundamental tradeoff in the usage of windowing functions is reduced sidelobes in exchange for increased beamwidth. In the particular application of the SuperDARN over-the-horizon radars, the directional resolution at the furthest range gates is linearly dependent on the antenna beamwidth as shown in the equations below [10]:

$$\Delta\theta_{az} = \theta_{3\text{ dB}} [\text{rad}]; \quad \Delta x = R\Delta\theta_{az} \quad (2.5)$$

At close range gates, directional resolutions on the order of tens of kilometers are achievable. However, at the furthest range gates, the directional resolution degrades to hundreds of kilometers. Thus, the cost of sacrificing beamwidth must be considered versus the improvement in sidelobe rejection. There is a possibility of using windows in applications that do not require fine directional resolution. For instance, a radar operating mode could utilize a scan with a wide beamwidth in order to more rapidly complete the scan and provide higher temporal resolution at the expense of the directional resolution.

Another fundamental tradeoff is the loss of integration gain due to the tapering of the windowing function. As discussed in the null-steering section, any loss of gain results in a reduction in the maximum range and signal to noise ratio of the radar. Since the signal to noise ratio is critical in the detection of targets and the quality of the Doppler velocity measurements, severely tapered windows such as the Blackman window are not viable options for SuperDARN radars. Less aggressive tapering schemes such as a 20 dB Chebyshev window may still be a viable option for certain operating modes, especially given the minimal mainlobe widening of this window. Ultimately, windowing functions have potential for operating modes with high sidelobe suppression requirements and low directional resolution requirements.

2.1.3 Imaging Radar

Beamforming techniques are not the only option for improving directional resolution and ambiguity if the raw data from each antenna element is recorded. By separately recording the data from each antenna, each antenna element can be treated as an independent sensor and an estimation process can be used to determine the angle of arrival for backscattered power. Like the windowing technique, this approach uses a technique developed in the spectral processing of time domain signals. A number of possible estimators exist such as the Capon maximum likelihood estimator, the Burg maximum entropy method, and the MUSIC (MUltiple Signal Classification) estimator. The MUSIC approach to imaging was previously demonstrated with a SuperDARN array by R. Todd Parris, W.A. Bristow, and S. Shuxiang at the Kodiak radar site and is described here as an example of imaging radar performance [15].

The MUSIC algorithm was originally developed in the 1970s by Schmidt at Northrop Grumman based on previous work by Pisarenko and was applied to frequency estimation [16] [17]. This estimator utilizes eigenvector decomposition to separate a correlation matrix in orthogonal signal

and noise vectors. For an imaging radar with M available lags and N antennas, the cross correlations between antennas are calculated to produce a correlation matrix, \mathbf{R} , as shown in the equation below [15]:

$$\mathbf{R} = \begin{bmatrix} R_{00}(\tau_0) & \cdots & R_{0N}(\tau_0) \\ \vdots & \ddots & \vdots \\ R_{00}(\tau_M) & \cdots & R_{0N}(\tau_M) \end{bmatrix} \quad (2.6)$$

In this matrix, each column corresponds to one of the N antennas and the cross correlation is calculated against a reference antenna ($n = 0$). Each row represents a different lag pair or delay represented by τ_m . Thus, an individual entry, $R_{0n}(\tau_m)$, represents the cross correlation between the reference antenna and antenna n at the lag τ_m .

The correlation matrix is then multiplied by a vector, $\mathbf{u}(f)$, of complex sinusoids to produce a phase vector, $\mathbf{X}(f)$.

$$\mathbf{u}(f) = [e^{j2\pi f\tau_0}, e^{j2\pi f\tau_1}, \dots, e^{j2\pi f\tau_M}] \quad (2.7)$$

$$\mathbf{X}(f) = \mathbf{u}(f) \cdot \mathbf{R} \quad (2.8)$$

Then, a cross-spectral correlation matrix, $\mathbf{V}(f)$, and its eigenvectors, $\mathbf{E}(f)$, can be found as

$$\mathbf{V}(f) = \mathbf{X}(f)^H \mathbf{X}(f) \quad (2.9)$$

$$\mathbf{E}(f) = \text{eig}(\mathbf{V}(f)) \quad (2.10)$$

The eigenvectors can then be separated into signal vectors, $\mathbf{v}_s(f)$, and noise vectors, $\mathbf{v}_n(f)$ based on the magnitude of eigenvalues.

$$\mathbf{E}(f) = [[\mathbf{v}_{n1}(f) \dots] [\mathbf{v}_{s1}(f) \dots]] \quad (2.11)$$

Finally, the brightness distribution, $B(\vec{k}, f)$, can be calculated based on noise vectors where $w(\vec{k})$ represents the weighting vector.

$$w(\vec{k}) = \left[e^{j\vec{k} \cdot \vec{r}_1}, e^{j\vec{k} \cdot \vec{r}_2}, \dots, e^{j\vec{k} \cdot \vec{r}_N} \right]^T \quad (2.12)$$

$$B(\vec{k}, f) = \frac{1}{w(\vec{k})^H (\Sigma v_n(f) v_n^H(f)) w(\vec{k})} \quad (2.13)$$

From the Parris, et al, Kodiak experiments, a 16 element SuperDARN array with a SNR of 23 dB can expect approximately 0.4° azimuthal resolution [15]. In contrast, the traditional beamforming approach used for the Kodiak radar receiver has an azimuthal resolution of 6.4° at a frequency of 10 MHz. Thus, imaging radars and directional estimators offer a far superior approach to calculating the direction of arrival for backscattered echoes.

The tradeoff with an imaging radar approach is the increase in the volume of data required for the processing. The other techniques considered so far simply adjust the weighting of the phased array before a combined stream of data is stored. Traditionally, the raw data from the antenna elements or even raw data from the sum of the array are not kept. Instead, an autocorrelation is calculated at the radar site and the resultant data are then transmitted across a radio link and stored. Storing the data from each individual antenna element increases the data requirements by a factor of 16. Thus, future adoption of an imaging radar approach would require a significant change to the type of data stored or an upgrade to the communication systems at the radar sites. Ultimately, imaging radars have a high potential for improving directional resolution in SuperDARN radars, but they are currently limited by data handling constraints.

2.2 Advanced Waveforms

The second motivation for adopting an SDR approach is the performance benefits of advanced waveform design enabled by SDR. The first section examines the ability of an SDR wideband digital beamformer radar to operate simultaneously across multiple frequency channels and look directions. The second section analyzes the potential benefits of an adaptive waveform design.

2.2.1 Multiple Beam and Frequency Division Multiplexing Scan Modes

The combination of digital beamforming and the flexibility of SDR enable new scan modes that improve the temporal resolution of the radar. In the current configuration, the radar sweeps a single beam sequentially across the radar field-of-view while using a single transmit frequency at a time. Modern cellular communication protocols utilize frequency division multiplexing to subdivide a frequency band into individual channels to enable a single base station to communicate with many devices [18]. The same principle can be implemented in a software defined radar that channelizes its spectrum to allow for separate processing of each narrowband section. With analog beamforming hardware, all the frequency channels are transmitted in the same direction, or a complex interleaving of the signals is required to change the look direction. In a digital array, the phase delays are applied in the digital domain, allowing for different beamformers to be applied to each of the narrowband signals. Thus, a software defined radar could look in multiple directions at once. As a result, fewer dwell times would be required in order to scan the entire radar field-of-view.

This approach requires limited interference between the narrowband signals. This interference is limited in two ways: the directional filtering of the digital beamformer and the frequency filtering of the channelizer.

2.2.2 Directional Filtering

This work used the digital beamforming code from the previous section to analyze the directional filtering and optimum beam spacing. Assuming a 60° radar field-of-view, the optimum spacing of N beams would be $\phi_{sep} = 60^\circ/N$ and the refresh rate would be $R_N = \frac{R_0}{N}$ where R_0 is the refresh rate for a single scanning beam. For the simplest multiple beam case of $N = 2$ beams, their array factors overlap as shown in Figure 2.10. The overlap between these patterns results in a directional interference pattern also shown in Figure 2.10.

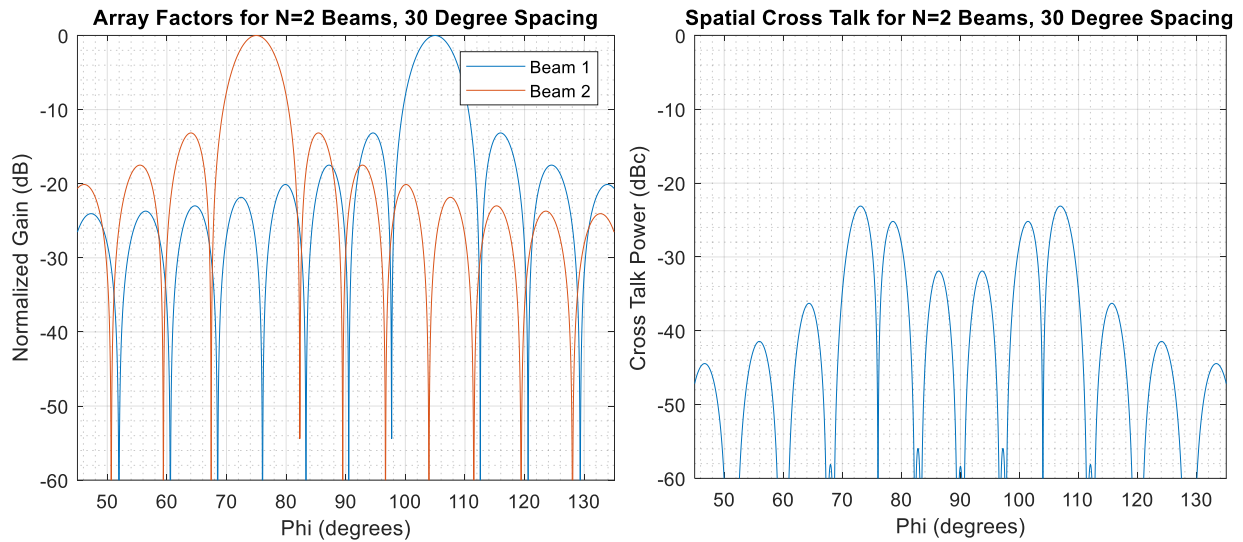


Figure 2.10. Array Factors and Interference for N=2 Beams

The interference pattern represents the relative strength of backscatter from a target illuminated by beam 2 and received by beam 1. In this case, the interference pattern shows that any interfering target illumination will be attenuated by over 20 dB. Additionally, this work observed that the nulls of one array factor approximately correspond to the look direction of the other beam. Thus, null-steering did not offer any additional interference suppression in this instance.

This work found that the optimum number of beams for a 16 element radar array with a 60° field-of-view was $N = 4$ beams with a spacing of 15° . Adding additional beams resulted in overlap of the main lobes of the antenna patterns. The array factors of these 4 beams and the sum of the interfering illumination received by beam 1 across beams 2, 3, and 4 are shown in Figure 2.11.

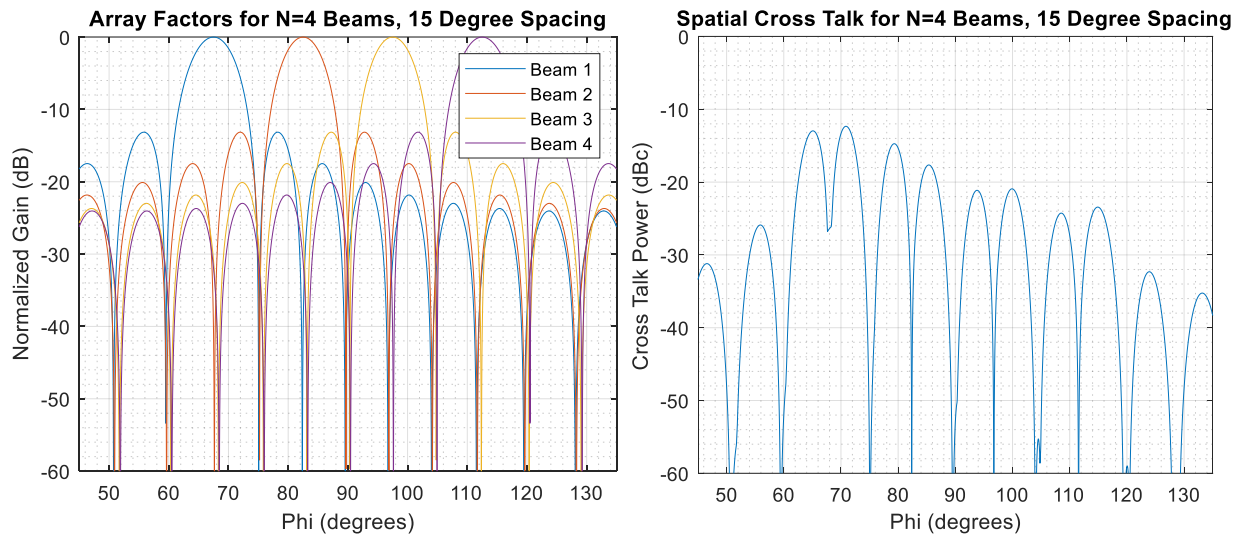


Figure 2.11. Array Factors and Interference for N=4 Beams

Once again, this work found that the nulls aligned with the main lobes meaning that negligible improvement would be accomplished by utilizing null-steering. This case experiences high levels of interference as the first sidelobes of beams 1 and 2 overlap with the main lobes of beams 2 and 1. In this case, the interference pattern shows that any interfering target illumination will be attenuated by over 13 dB. While this level of attenuation would be inadequate alone, the combined use with frequency division multiplexing makes 13 dB an acceptable level of attenuation. In fact, a perfect brick wall frequency filter would eliminate the need for directional filtering entirely, but the practical limitations of frequency filtering make directional filtering advantageous.

2.2.3 Frequency Multiplexing and Channelizer Design

The second method of mitigating interference between beams is by using frequency multiplexing. Each of the signals is transmitted at a different frequency offset within the radar bandwidth and is processed separately. Based on the results of the directional filtering section, this work designed and analyzed the performance of a 4 channel system.

The current SuperDARN receiver architecture at the Blackstone radar uses a 7 kHz IF filter [19].

For consistency, this work used 7 kHz as the desired bandwidth of an individual channel.

Recalling the relation between Doppler frequency and target velocity, a 7 kHz bandwidth at a center frequency of 10 MHz corresponds to a maximum unambiguous relative velocity of ± 57.5 km/s.

$$f_d = \frac{2v_r}{\lambda} \quad (2.14)$$

$$7 \text{ kHz} \times 30 \text{ m} \div 2 = 105 \frac{\text{km}}{\text{s}} \quad (2.15)$$

$$v_{r,ua} = \pm 57.5 \text{ km/s} \quad (2.16)$$

This large unambiguous velocity value suggests that in the future, more narrowband filters could be used to reduce the noise bandwidth of the radar. Analog filters are limited by the quality factor of the components and parasitic capacitances and inductances. Digital filters are limited by computational complexity. In order to efficiently filter and process each narrowband signal, a channelizer is needed to separate the single received signal into several narrowband signals. Since the individual channels use less bandwidth, a lower sampling rate can be used without violating the Nyquist criterion. In the channelizer implementation, two operations must be performed: anti-alias filtering and decimation. Since the decimation step removes samples, applying the filtering to the removed samples is computationally inefficient. Polyphase filters

offer an efficient method for achieving the filtering and decimation required in the channelizer by applying the filtering at the lower sampling rate after the decimation is performed. For this reason, polyphase filters are commonly used in multirate systems to reduce the computational cost by performing processing at lower sampling rates [12].

Based on the results of the directional filtering section, this work analyzed the performance of a polyphaser filter bank with 4 narrowband channels. This work chose a 50 kHz RF bandwidth in order to accommodate the 4 narrowband channels with a channel spacing greater than the 7 kHz bandwidth of each channel. The 12.5 kHz channel width allowed for a large transition bandwidth between the channels and a high degree of attenuation. This work set the stopband attenuation at 60 dB which, combined with the directional filtering, offered sufficient interference suppression while maintaining computational efficiency. This work implemented this filter design in GNU Radio, a tool for signal processing and software defined radios, and tested the design for the case of a simulated narrowband signal in the presence of wideband noise as shown in Figure 2.12.

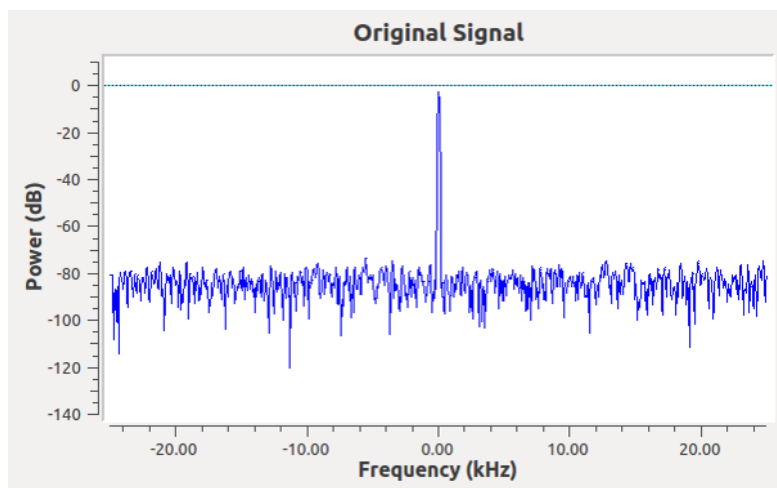


Figure 2.12. RF Channelizer Input Signal

The wideband noise had a flat frequency response extending across the entire 50 kHz bandwidth corresponding to the 50 kHz complex sampling rate. This work placed the narrowband signal at the center of the first frequency channel. The outputs of the polyphaser implementation of the channelizer are shown in Figure 2.13.

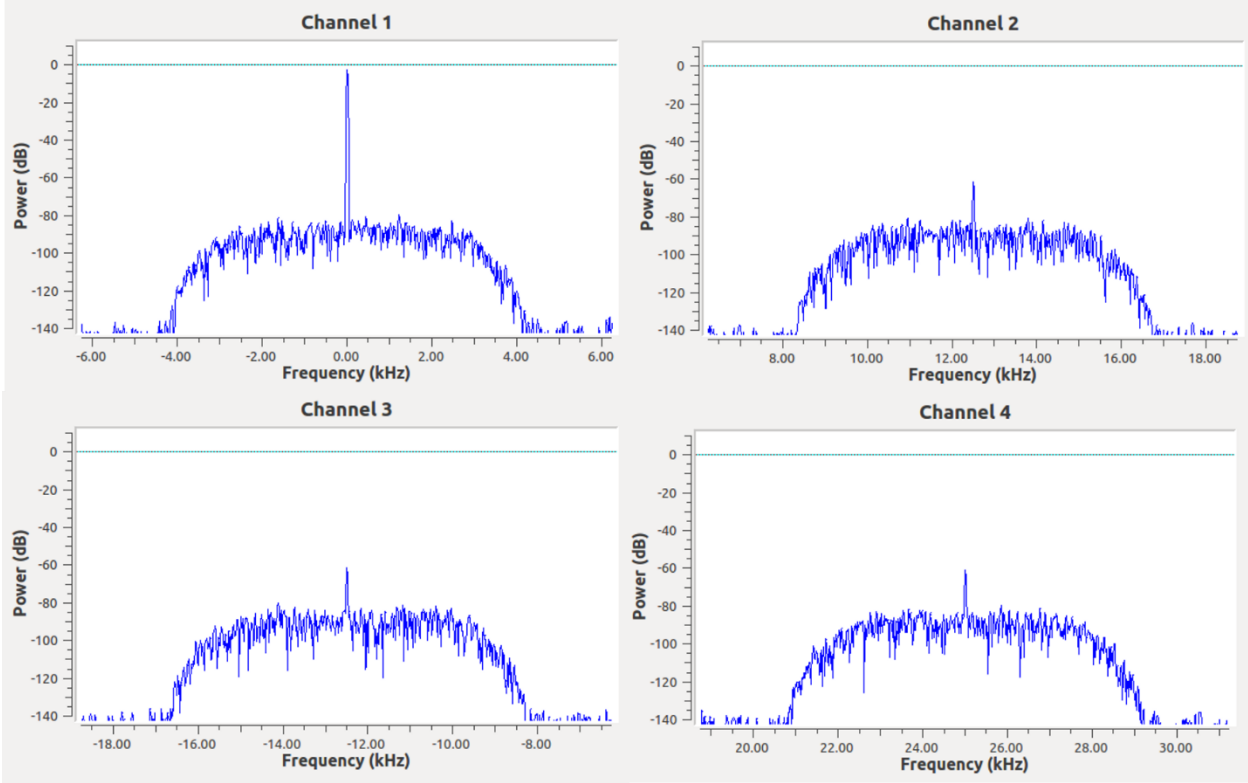


Figure 2.13. Channelizer Outputs

The 7 kHz wide polyphaser filter is visible in the altered shape of the noise in each channel. Additionally, the input tone was attenuated by 60 dB in channels 2, 3, and 4 confirming the stopband attenuation. Thus, this work demonstrated a polyphaser channelizer design providing adequate interference attenuation.

Another consideration unique to ionospheric radar is the relation between frequency and propagation path of the radar signal. In the SuperDARN sky wave propagation, differences in frequency will result in different ionospheric refraction as shown in Figure 2.14.

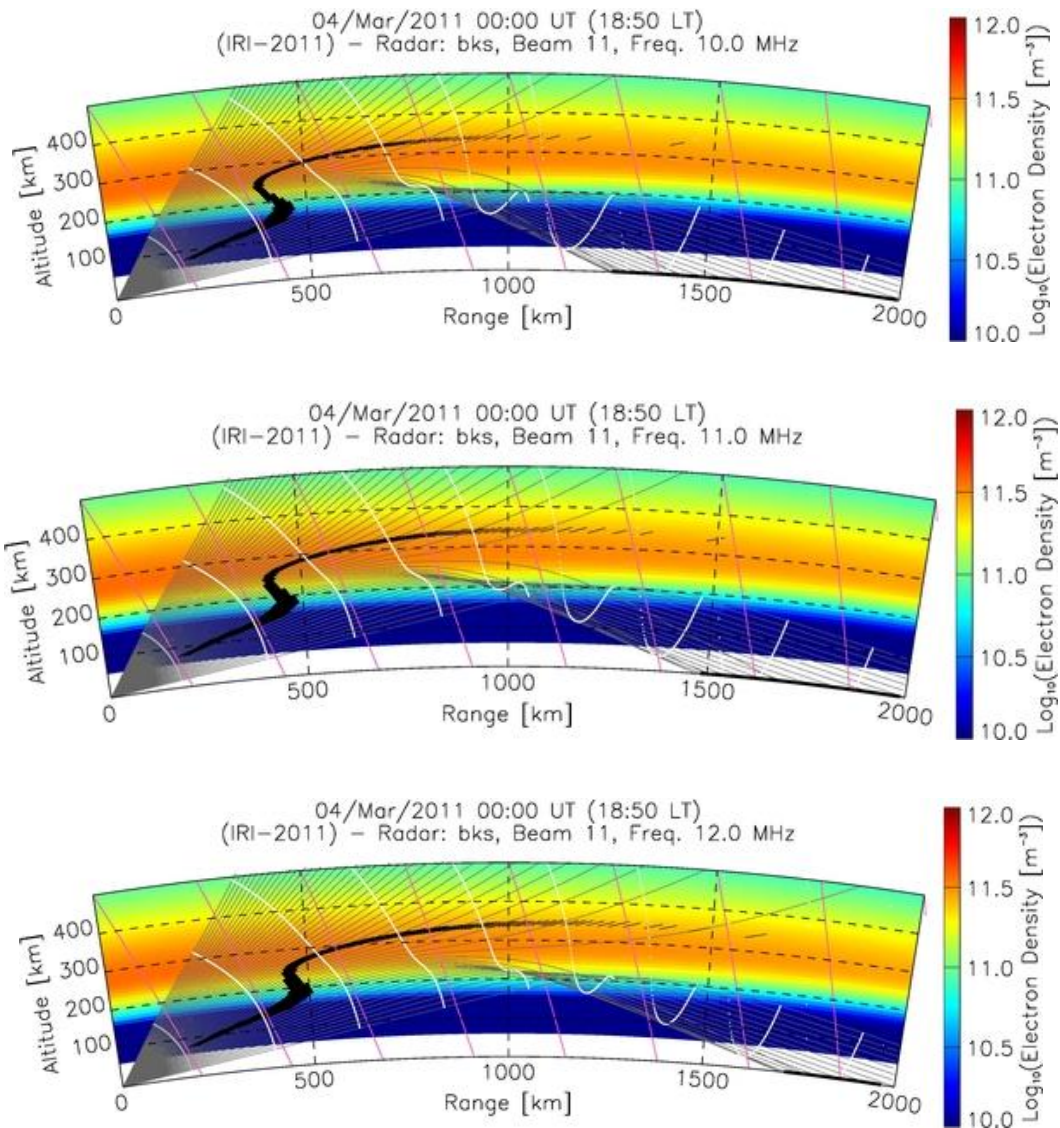


Figure 2.14. Ray Tracing for an IRI Model Ionosphere at 10 MHz, 11 MHz, and 12 MHz [4]

The higher frequency signals experience less refraction and take a different path than the lower frequency signals. As a result, different beams at different frequencies will be looking at slightly different locations and their results may not be correlated. Thus, it is beneficial to cluster all

channels within a minimal bandwidth to reduce the extent of the variation in propagation path. Additionally, it may not be appropriate to compare the results from beam 1 to the results from beam 2 at the same time instant. Instead, this approach to scanning can be thought of as four separate scans whose time intervals overlap rather than four beams of a single scan. In this way, the results of a single “scan” will be at the same frequency and will correlate, and the refresh rate will be improved by the number of beams or scans occurring simultaneously.

This work has shown that a combination of digital beamforming and frequency multiplexing can be used to significantly improve the refresh rate of SuperDARN radars. The directional and frequency filtering prevent interference allowing several scans to be operated simultaneously. This analysis did not consider the potential power limitations of the existing SuperDARN amplifiers or the effect of the nonlinearities within these amplifiers. Accordingly, the implementation of this multiple scan mode should consider the hardware limitations of each individual radar site.

2.2.4 Cognitive Radar and Adaptive Waveforms

The flexibility of software defined radio enables the implementation of cognitive radios which alter their parameters in response to environmental conditions. In the case of radar systems, cognitive systems can alter the waveform parameters in order to maximize the radar performance. For instance, the current SuperDARN radars utilize a degree of cognitive radar principles by searching for open frequency bands and dynamically selecting the transmit frequency to minimize interference. This work examined the effects of dynamically changing the range resolution of a SuperDARN radar.

In the current SuperDARN multipulse sequence, each individual pulse is $300 \mu\text{s}$ long which corresponds to a range resolution of 45 km. This range resolution is defined by the first null in the autocorrelation function of the waveform. Improving the range resolution without reducing the average transmit power can be accomplished through pulse compression. In this case, this work considered a phase coded waveform using a Barker code with length $n = 3$. A comparison of these two waveforms is shown in Figure 2.15.

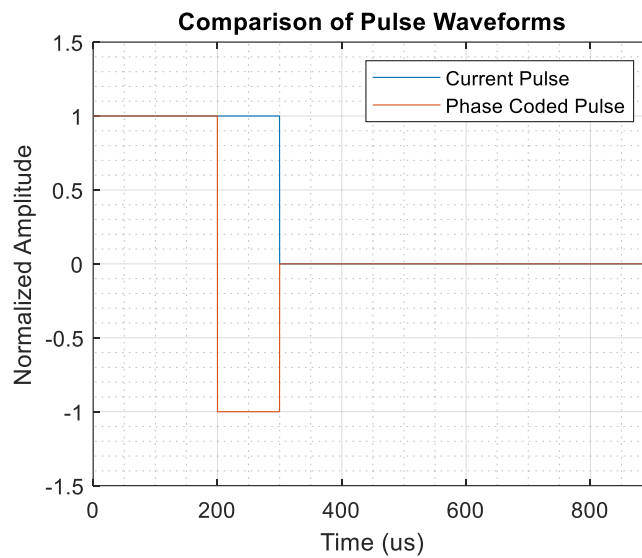


Figure 2.15. Comparison of Pulse Waveforms

The Barker code divides the pulse into three segments consisting of a binary sequence of +1 or -1. The pattern of a Barker code with length $n = 3$ is [+1, +1, -1] as seen in Figure 2.15 [10].

The autocorrelation of these two waveforms is shown in Figure 2.16.

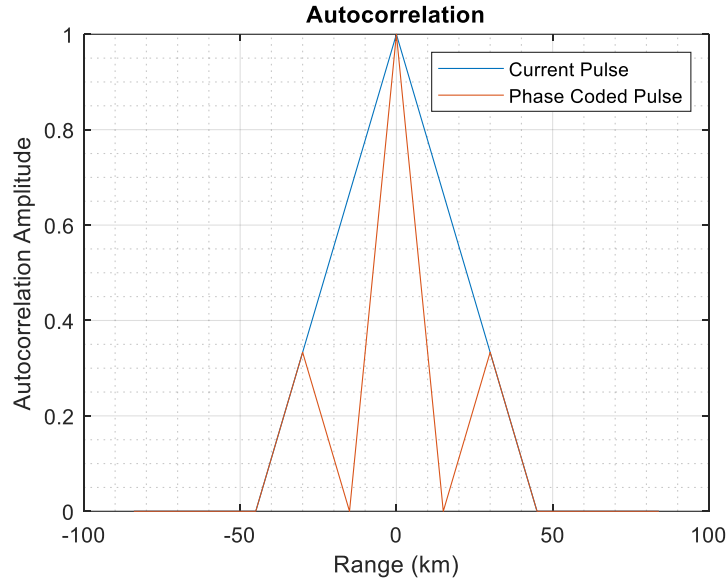


Figure 2.16. Comparison of Range Resolution

The phase coded waveform produces a range resolution of 15 km as defined by its first null. This range resolution corresponds to the resolution of a single segment of the three segment pulse, and represents an improvement in the range resolution by a factor of 3.

Pulse compression waveforms have been widely used for decades, but generally have not been used in SuperDARN radars due to the tradeoffs between range resolution and SNR for ionospheric radars. In the case of soft or beam-filling targets, the received power (and therefore SNR) is directly proportional to the range resolution (ΔR) of the radar as shown in the radar range equation below [10]:

$$P_r = \frac{P_t A \sigma_v \Delta R}{4\pi R^2} \quad (2.17)$$

Increasing the range resolution increases the volume of targets that the radar can use to produce backscattered echoes. Thus, reduced range resolution is generally undesirable. However, in circumstances with high electron densities, ionospheric targets will have large radar cross section

targets resulting in a high SNR. In this case, it would be desirable to switch to a pulse compressed waveform to improve the range resolution of the radar at the expense of the excess SNR. A cognitive radar system would be able to dynamically alter the waveform in order to maximize the range resolution while achieving a predetermined SNR threshold. A number of similar radar tradeoffs can be explored such as refresh rate vs. unambiguous range, range resolution vs. maximum range, and coherent processing interval vs. refresh rate. Ultimately, implementing a software defined radio approach would allow cognitive radar techniques to maximize the performance of SuperDARN radars.

Chapter 3. Prototype Development

The second objective of this thesis was to develop a prototype software defined radio system to determine the feasibility of switching to a software radio platform and to evaluate its performance. Several system goals guided the hardware selection and design process. First, the system needed to digitize each element of the antenna array in order to enable advanced beamforming techniques. Second, the system needed to digitize a large portion of the bandwidth of the SuperDARN twin terminated folded dipole array in order to enable advanced signal processing techniques. Additionally, this work chose a direct conversion architecture in order to remove the need for a mixer further improving the system linearity while also reducing the amount of external hardware required.

The software defined radio is the core of this prototype. This work derived several requirements for the selection of the software radio from the system goals. First, the need to digitize the entire array imposed a constraint on the cost of the device. The SuperDARN antenna array requires 16 receivers and 16 transmitters in order to fully digitize the array. Since this setup increases hardware costs by a factor of 16, this work limited the cost for a single transceiver to \$500.

The bandwidth of the SuperDARN array is approximately 6 MHz from 10 to 16 MHz [19]. Digitizing this entire bandwidth would increase the data handling requirements without providing substantial benefit as the SuperDARN signals are relatively narrowband. Additionally, the difference in frequency across this bandwidth results in a difference in propagation path due to the nature of ionospheric refraction. Thus, this work defined a 500 kHz bandwidth requirement, corresponding to full IQ (in-phase and quadrature) data at 500 kSPS to satisfy the Nyquist sampling criterion, which would be sufficient to enable multichannel operation.

The goal of using a direct conversion architecture to improve the system performance added additional sampling rate requirements. In order to satisfy the Nyquist criterion, a sampling rate greater than 32 MSPS was needed to digitize a signal at 16 MHz, the upper end of the SuperDARN bandwidth. Thus, the SDR ADC needed a sampling rate greater than 32 MSPS, and then needed to perform filtering and down conversion to reduce the bandwidth and data rate without introducing aliasing. It was imperative that the software radio perform this downconversion in a dedicated FPGA or DSP chip in order to efficiently manage the data across all 16 array elements and across each frequency channel used.

Due to the nature of radar systems, the receiver needed a high sensitivity in order to detect the weak radar echoes, particularly from the farthest range gates. One estimate of the quantization noise in an ADC is the ADC signal to noise ratio (SNR) as calculated from the number of bits (N) in the ADC. This relation is shown in the equation below [20]:

$$SNR = 6.02N + 1.76 \text{ dB} \quad (3.1)$$

This work imposed a requirement of a minimum of 12 bits on the SDR selection in order to provide an SNR of approximately 74 dB.

No major constraints were imposed on the output power of the transmit path of the SDR as each SuperDARN site is already equipped with transmitter boxes which provide adequate amplification for even relatively small signal sources as well as sufficient filtering of out of band spurs. However, linearity was considered when evaluating the transmitter performance.

3.1 Red Pitaya Selection

This work chose the Red Pitaya STEMLab 125-14 as the software defined radio for this prototype [21]. The Red Pitaya is a multipurpose test and measurement environment particularly for use in

educational settings. The Red Pitaya is a partially open-source project as the project software is open source, but the hardware schematics are limited. The core of the Red Pitaya is a Xilinx Zynq 7010 system on a chip (SOC) which offers a dual core ARM Cortex A9 processor and a FPGA. The reprogrammable FPGA is the key to the device's flexibility as a multi-instrument platform and also enables efficient computation of digital signal processing in SDR applications. The STEMLab 125-14, shown in Figure 3.1 below, utilizes a 14 bit ADC with a 125 MHz sampling frequency providing a broad bandwidth of signals up to 62.5 MHz [21].



Figure 3.1. Red Pitaya STEMLab 125-14 [21]

A key advantage of the Red Pitaya for SuperDARN applications is the low cost per transmit and receive path. Each device has two transmit and two receive paths such that only 8 devices at approximately \$300 per device could digitize an entire SuperDARN main array (not including additional hardware costs associated with amplification and clock distribution). The declining cost of electronics drives the low cost of software radios and enables the adoption of SDR in more applications such as digitizing large arrays.

The Red Pitaya is powered through a 5V 2A micro-USB power supply and communicates data via Ethernet connection. A micro-SD card, of up to 32 GB, is used as the device's storage. The

device is also able to use an external ADC clock to synchronize several Red Pitaya devices which was important for prototyping a digital array.

Software defined radio applications do not use the standard Red Pitaya software. Instead, open-source code developed by Pavel Demin enables operation as a software defined radio [22]. This code offers support for several applications including an SDR transceiver, embedded SDR transceiver, wideband SDR transceiver, multiband WSPR transceiver, and vector network analyzer. The prototype development and evaluation in this work utilized the SDR transceiver application. The SDR transceiver application utilizes digital down-converters (DDC) and digital up-converters (DUC) to process the ADC and DAC samples as shown in Figure 3.2 and offers a configurable IQ data rate with settings up to 1250 kSPS [22].

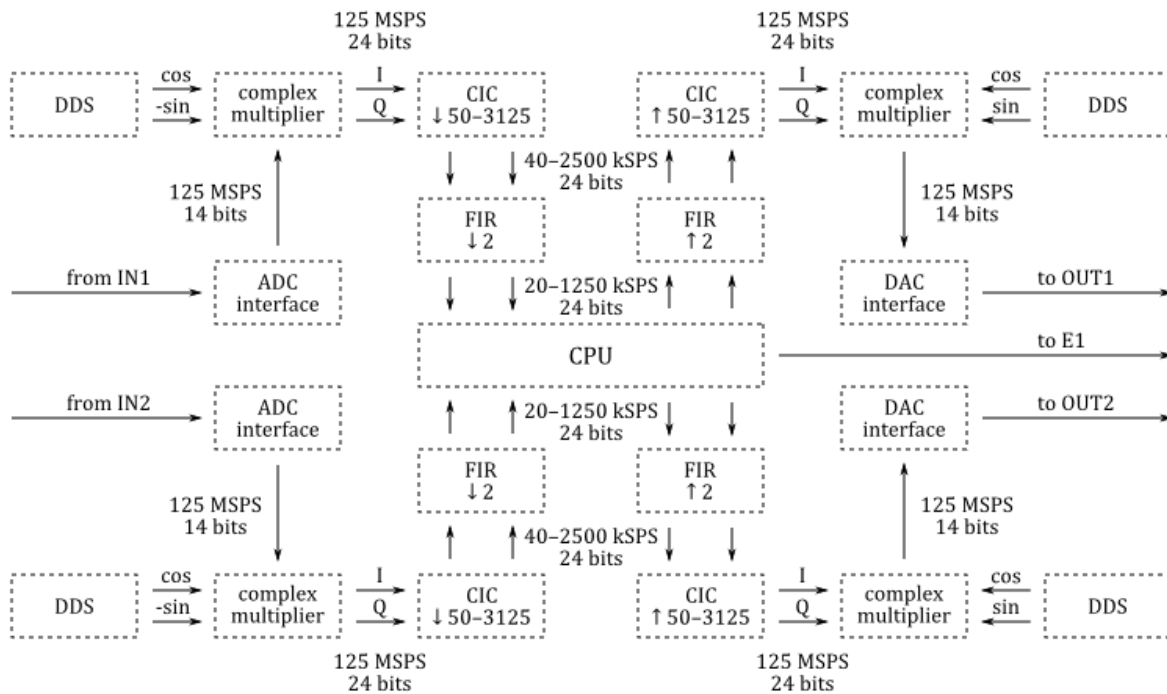


Figure 3.2. Block Diagram of Red Pitaya Digital Frequency Conversions [22]

Each of the two receive channels are digitized by the Red Pitaya's 14 bit ADC at 125 MSPS. The samples are processed as complex in-phase and quadrature (IQ) samples and cascaded integrator-comb (CIC) filter performs anti-aliasing filtering, decimation, digital downconversion. A finite impulse response (FIR) filter performs another decimation and passes the data to the CPU. The transmit path follows a parallel process where the CPU generates IQ samples which pass through an interpolator and digital upconversion before being passed to the DAC.

This software interfaces with GNURadio offering a simple method for test and development of software defined radio applications. Using GNURadio to control the Red Pitaya enabled rapid development and greater flexibility since GNURadio designs for other hardware platforms, such as an Ettus Research USRP, can be adapted to work with the Red Pitaya by simply replacing the sink and source blocks.

Additionally, the Red Pitaya platform has a history of use in other ionospheric research projects including ionosondes and passive HF radar systems [23] [24]. Overall, the low cost per channel, ease of use with GNURadio, and prior success in ionospheric research led to the selection of the Red Pitaya as the software defined radio for this prototype.

3.2 Red Pitaya Impedance and Modification

The Red Pitaya does experience some issues as a byproduct of its original design as a multi-instrument platform. The foremost issue is the impedance mismatch of the receive ports. Despite having standard SMA connections on the receive inputs, these channels are designed to have a 1 M Ω DC impedance to be used as oscilloscope probes. At 10 MHz, the lower end of the SuperDARN frequency range, the input impedance is approximately 1 k Ω [21]. This large impedance results in a significant mismatch when paired with a standard 50 Ω feedline. Previous

work showed that adding a 1:9 transformer between the SMA connector and the ADC effectively resolves the impedance mismatch issue and improves the sensitivity of the Red Pitaya [23]. This work implemented this approach, and subsequent measurements show a marked improvement as shown in the Red Pitaya Characterization section below.

3.3 Red Pitaya Characterization

This work performed several tests on the receive and transmit paths of the Red Pitaya in order to assess its typical performance. The first test measured the minimum discernable signal (MDS) on the receive path of the software radio. This test was completed both with and without the transformer modification described in the previous section in order to verify the improvement in the impedance mismatch loss. The test setup used a continuous wave tone from a signal generator, and a 500 kHz bandwidth at the 500 KSPS setting on the Red Pitaya. As seen in Figure 3.3, the addition of the impedance transformer produced a significant 15 dB improvement in the minimum discernable signal.

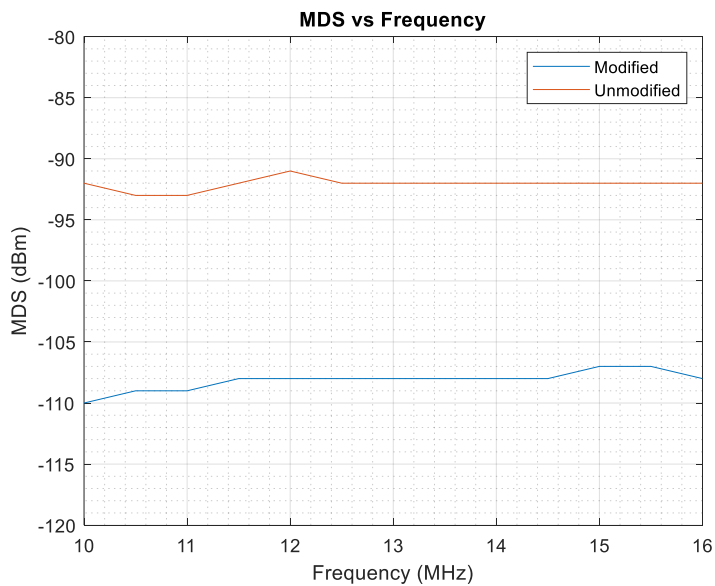


Figure 3.3. Minimum Discernable Signal vs Frequency for Modified and Unmodified Designs

A noise source for a direct measurement of the radio's noise figure (NF) was not available, but an estimation of the noise figure can be made from the MDS if certain assumptions are made.

The relation between MDS and NF is shown in the equation below where k represents the Boltzmann constant, T is the temperature, and B is the receiver bandwidth [12].

$$MDS = 10 \log_{10} \left(\frac{kT}{1 \text{ mW}} \right) + NF + 10 \log_{10} B \quad (3.2)$$

In calculating the noise figure, the 500 kHz bandwidth and MDS measurements from the MDS test were used. Assuming a noise temperature of 290 K, this work calculated estimates of the Red Pitaya's noise figure as shown in Figure 3.4. Once again, the results indicated a significant improvement in the system sensitivity due to the addition of the impedance transformer. Since the Red Pitaya does not include a low noise amplifier (LNA), the noise figure was still high indicating that a front end design would be needed in order to achieve the necessary sensitivity.

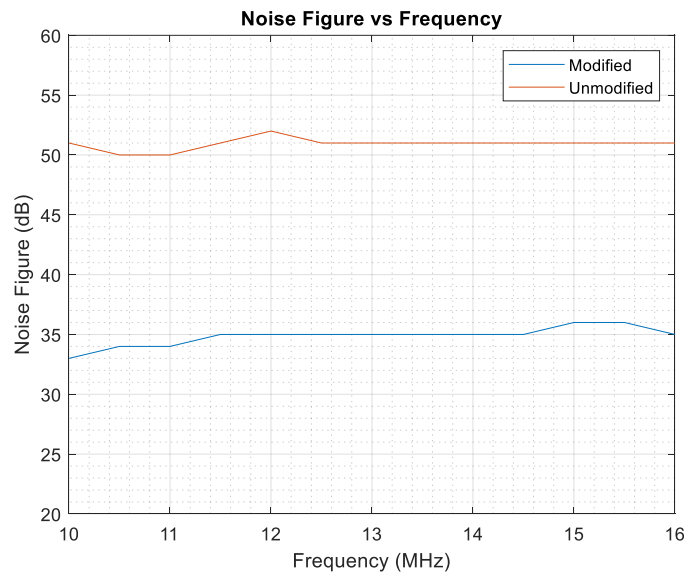


Figure 3.4. Noise Figure vs. Frequency

The next tests of the receive path examined the linearity of the receiver performance. First, this work measured the 1 dB compression point of the Red Pitaya by increasing the input power of a continuous tone until the measured power differed from the ideal linear trend by 1 dB as shown in Figure 3.5. The resultant 1 dB compression point of -4 dBm of input power provides the effective maximum input power before nonlinearities are produced by compression. In the context of a SuperDARN radar, the weak backscattered power is expected to be far below -4 dBm indicating that the system will not be constrained by compression in the Red Pitaya.

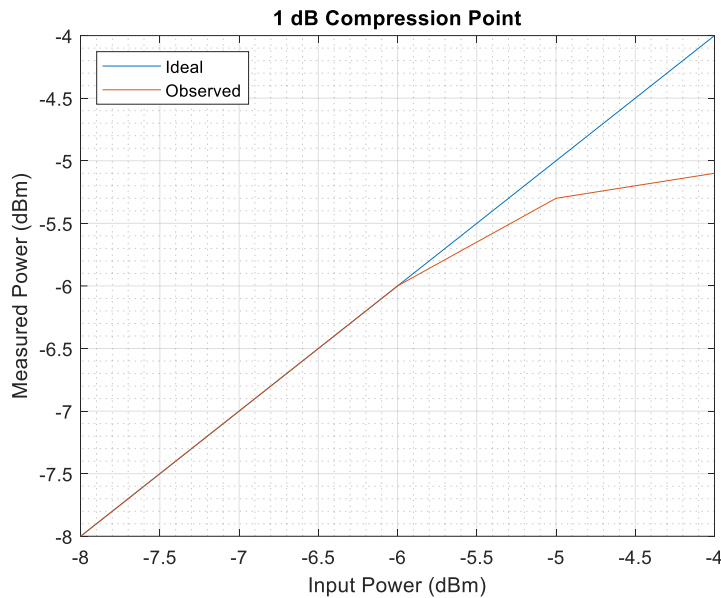


Figure 3.5. 1 dB Compression Point

A two tone test was used to determine the input referred third order intercept point (IIP3). The two tones were spaced at ± 50 kHz from the center frequency such that the third order intermodulation tones appeared at ± 150 kHz. Once again, a 500 kHz bandwidth was used. The IIP3 values were calculated from the measured input and third order modulation power, and are shown in Figure 3.6.

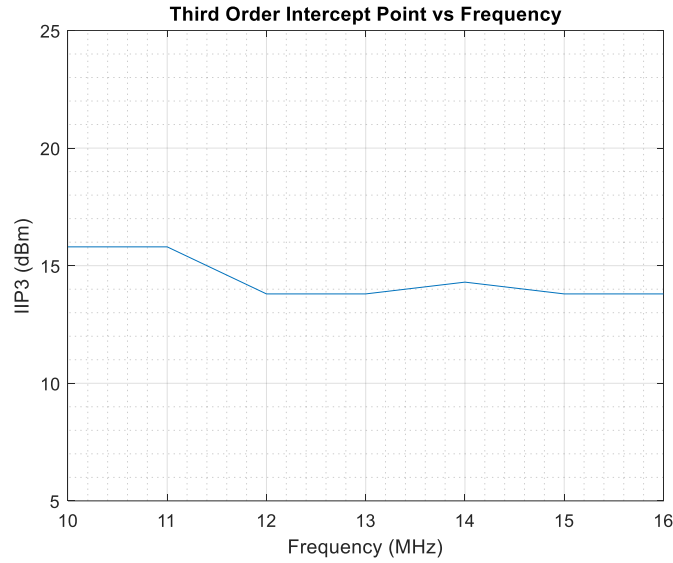


Figure 3.6. Third Order Intercept Point vs Frequency

These measurements show a reasonably flat frequency response with slightly diminishing performance as the frequency increases. These results indicate that, at the low power levels associated with radar echoes, any intermodulation effects will most likely be below the noise floor. In other words, the system will be constrained by its sensitivity and not by its linearity.

The measurements of MDS and IIP3 were then used to calculate the spurious free dynamic range (SFDR) according to the equation below [12]:

$$SFDR = \frac{2}{3}(IIP3 - MDS) \quad (3.3)$$

The resultant values for the spurious free dynamic range of the Red Pitaya's receive paths are shown in Figure 3.7.

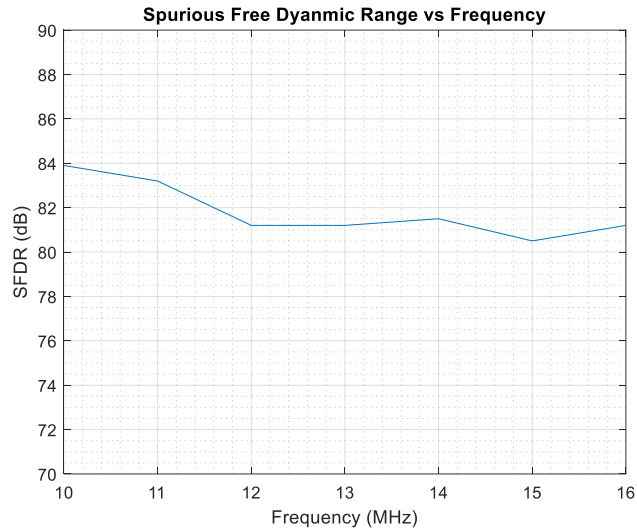


Figure 3.7. SFDR vs Frequency

These results are reasonably consistent with respect to frequency and also provide an adequate dynamic range for the detection of radar echoes. Once again, these results indicate the system will be constrained by its sensitivity and not by its linearity

The next tests characterized the performance of the transmitter paths on the Red Pitaya. The first transmitter test showed the variation of the maximum output power with respect to the transmit frequency as shown in Figure 3.8.

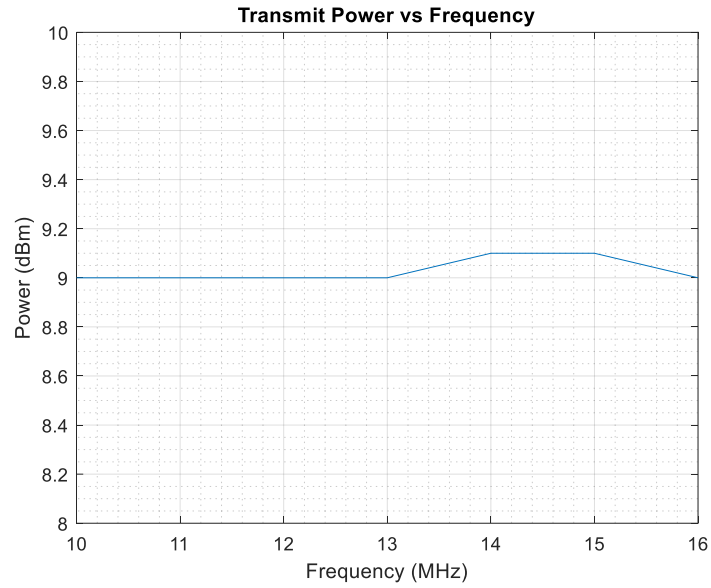


Figure 3.8. Transmit Power vs. Frequency

An output power of +9 dBm is sufficient to drive the existing SuperDARN transmitter amplifiers for testing purposes at approximately two thirds of their maximum power. Future implementation of the Red Pitaya as the signal source for a SuperDARN radar may require minor modifications to the driver amplifier design.

The linearity of the transmitter is particularly important for enabling multichannel operation without producing spurious emissions. Using the same two tone test from the receive path IIP3 measurements, the output referred third order intercept points were calculated for the transmitter as a function of frequency as shown in Figure 3.9.

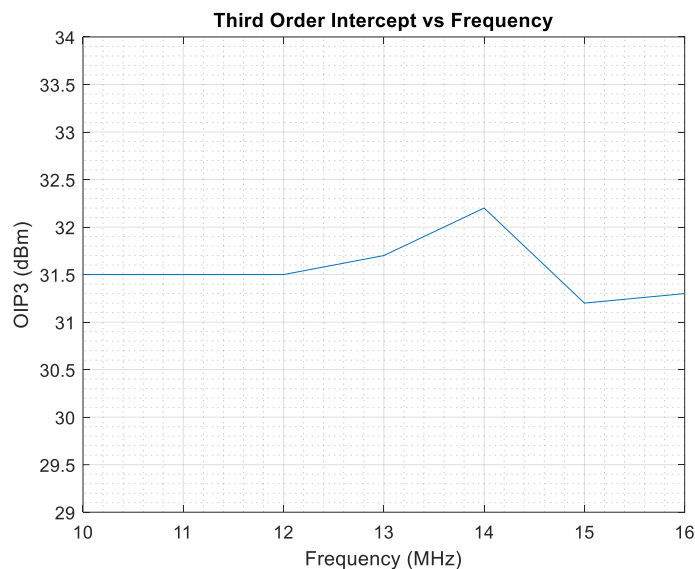


Figure 3.9. Third Order Intercept Point vs. Frequency

These results indicate that the Red Pitaya will be able to perform multichannel operations without significant performance degradation due to nonlinearities. Overall, the Red Pitaya provides adequate linearity on both the transmit and receive paths, in part due to the elimination of analog mixers in a direct conversion architecture. While testing the Red Pitaya operating both receive channels, this work found a potential issue due to cross-talk between the two receive channels as discussed in the following section.

3.4 Cross-Talk Issue and Analysis

During testing of the receive paths, a crosstalk issue was observed between the channels. A steady crosstalk power of approximately -55 dBm was observed across the SuperDARN bandwidth posing a potential issue for using the Red Pitaya in SuperDARN applications. This issue is primarily caused by both receive channels passing through amplifiers implemented on the same component [25]. The cross talk between channels affects the system performance by degrading the beamformer performance.

In digital beamforming on the receive path, a plane wave approaching the antenna array will reach each element of the antenna array at a different phase delay. These phase delays can be expressed as a steering vector in terms of the plane wave's wavevector (\mathbf{k}) and the position (\mathbf{r}) of each of the N elements of the antenna array [26].

$$\mathbf{v} = \left[e^{-j\mathbf{k}\cdot\mathbf{r}_1}, e^{-j\mathbf{k}\cdot\mathbf{r}_2}, \dots, e^{-j\mathbf{k}\cdot\mathbf{r}_N} \right], \quad \mathbf{r}_i = (x_i, y_i, z_i) \quad (3.4)$$

The digital beamformer then applies phase delays or weights to each element of the array in order to compensate for the phase delay experienced by the plane wave resulting in constructive interference. In the case of the Red Pitaya, the cross talk occurs before the phase and amplitude weights are applied so the influence of the cross talk can be considered in the expression of the steering vector. To express the cross talk in the steering vector, this work considered an effective steering vector (v_{eff}) formed from a linear superposition of the two interfering signals at each receiver in the array. The extent of the cross talk, measured in decibels relative to the signal's original power, is represented in this superposition by a linear scaling factor, ρ .

$$\rho = 10^{\frac{P}{20}}, \text{ where } P \text{ is the signal power in } dB \quad (3.5)$$

It is assumed that the cross talk power between the two channels on the Red Pitaya is approximately symmetric based on the observed and expected characteristics of the device.

Thus, the paired elements of this effective steering vector can be represented as:

$$v_{1,eff} = (1 - \rho)v_1 + \rho v_2 \quad (3.6)$$

$$v_{2,eff} = \rho v_1 + (1 - \rho)v_2 \quad (3.7)$$

The contribution of these two channels to the array factor can then be found:

$$AF = w_1 v_1 + w_2 v_2 + \dots + w_N v_N \quad (3.8)$$

$$AF_{eff} = w_1 v_{1,eff} + w_2 v_{2,eff} + \dots + w_N v_{N,eff} \quad (3.9)$$

$$AF_{eff} = w_1(1 - \rho)v_1 + w_2(1 - \rho)v_2 + w_2(\rho)v_1 + w_2(\rho)v_1 \dots + w_N v_{N,eff} \quad (3.10)$$

$$AF_{eff} = (1 - \rho)(w_1 v_1 + w_2 v_2) + \rho(w_2 v_1 + w_2 v_1) \dots + w_N v_{N,eff} \quad (3.11)$$

Thus, the new array factor can be seen as the previous array factor reduced by a scale factor and a second array factor superimposed due to the cross weighting of the channels.

$$AF_{eff} = \alpha AF + \rho AF_2, \quad \alpha = 1 - \rho \quad (3.12)$$

$$AF_2 = w_1 v_2 + w_2 v_1 + w_3 v_4 + w_4 v_3 + \dots + w_{N-1} v_N + w_N v_{N-1} \quad (3.13)$$

The cross talk issue occurs between the two channels that share a single Red Pitaya device.

Accordingly, the cross talk generated by one channel only affects one other channel. Therefore, any one element in the effective steering vector is only dependent on the steering vector elements corresponding to that element and that element's "partner" channel. This work found that careful selection of these element pairs and the weighting vector mitigated the degradation of the beamformer due to cross talk.

In order to understand how pairing selections influenced the beamforming quality, this work completed simulations of the array factor in MATLAB. This simulation used 16 antenna elements in a linear array with half wavelength spacing. These criteria were chosen in order to approximate the conditions of the SuperDARN antenna arrays. One key difference in the actual array is that the spacing of the SuperDARN antenna elements, in terms of wavelength, varies slightly as the frequency of the system changes. To calculate the array factor, the weight vector

was calculated first for a given look direction of the antenna array. The corresponding steering vector and array factor for an array with no cross talk were computed to serve as a reference. Then, the effective steering vector was calculated for various channel pairing combinations and for several cross talk power levels. Results from these simulations are presented in the following sections.

3.4.1 Effect of Cross Talk on Broadside Radiation

The simplest case occurs when the antenna is steered so that the beam points in the broadside direction ($\phi = 90^\circ$). In this orientation, the weighting vector simply reduces to a single value for all antenna elements.

$$w_n = e^{jn\pi \cos \phi} \quad (3.14)$$

$$w_n = e^{jn\pi 0} = 1 \quad (3.15)$$

Thus, the weighting on each channel of the array has the same magnitude and phase. As a result, the corresponding array factor for the broadside direction is governed solely by the effective steering vector and the scale factor due to cross-talk. Since the effective steering vector is shown to be a symmetric linear superposition of elements from the original steering vector, it can be shown that the array factor for the broadside case is independent of the cross talk.

$$AF = w_1 v_1 + w_2 v_2 + \dots + w_N v_N \quad (3.16)$$

$$AF = v_1 + v_2 + \dots + v_N \quad (3.17)$$

$$AF_2 = w_1 v_2 + w_2 v_1 + w_3 v_4 + w_4 v_3 + \dots + w_{N-1} v_N + w_N v_{N-1} \quad (3.18)$$

$$AF_2 = v_2 + v_1 + v_4 + v_3 + \dots + v_N + v_{N-1} \quad (3.19)$$

$$AF = AF_2 = v_1 + v_2 + \dots + v_N \quad (3.20)$$

$$AF_{eff} = \alpha AF + \rho AF_2 = (1 - \rho)AF + \rho AF = AF \quad (3.21)$$

Thus, the presence of cross talk will have no effect on the broadside radiation pattern of the antenna array (barring intermodulation, compression, and other non-linearity issues within the receiver). This expected result was used to verify the simulation results as shown in Figure 3.10.

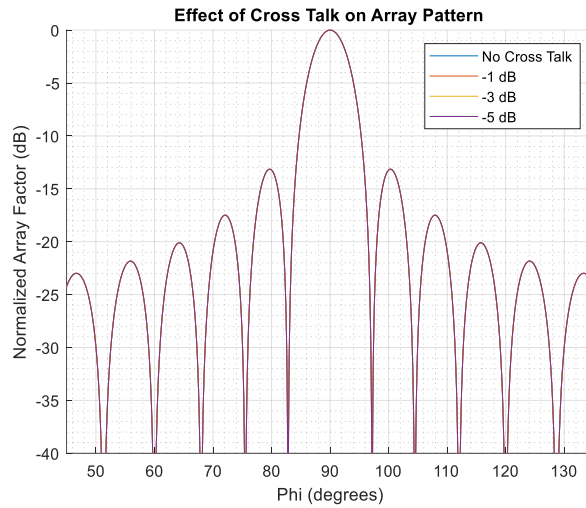


Figure 3.10. Effect of Cross Talk on Array Factor for $\phi = 90^\circ$

The array factor did not change for the broadside case even with increasing levels of cross-talk power. However, it is important to note that this result only occurred due to the rectangular windowing of the weighting function which occurs when no window is applied. If another type of window were applied, the elements of the weighting vector would not be equal resulting in a

disruption of the beamforming and array factor. For example, this work applied a 16 point Hanning window to the weighting vector producing the altered array factor shown in Figure 3.11. The results in this figure show a degradation of the beam performance when steered broadside; whereas, the weighting shown in Figure 3.10 did not experience a degradation. Thus, any analysis must include the weighting schemes used in processing the beamforming information.

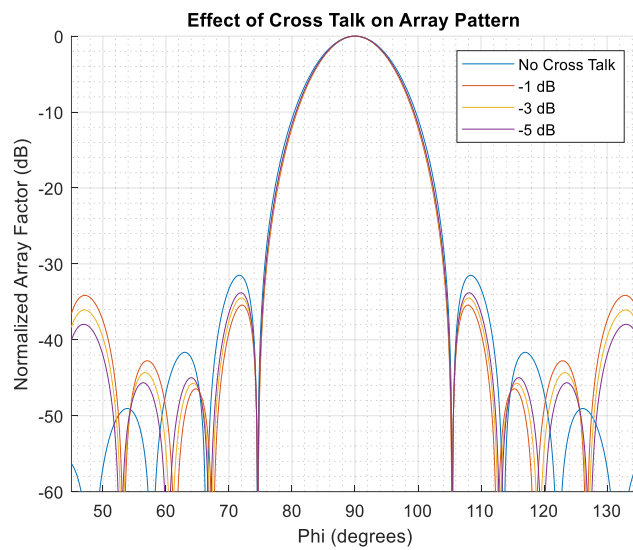


Figure 3.11. Effect of Windowing on Array Factor for $\phi = 90^\circ$

The SuperDARN antenna arrays currently use rectangular windowing in their analog beamforming. Since this approach is likely to be continued in future systems and for the sake of comparison, the following approaches to channel pairing were completed using rectangular windowing.

3.4.2 Adjacent Pairing Approach

The first approach to channel pairing was to pair adjacent antenna elements. In this pairing scheme, antenna element 1 was paired with the neighboring antenna element 2 such that both signals would be processed on the same Red Pitaya device. Without considering the implications of the cross talk interference, this approach would most likely have been chosen for simplicity and to minimize the length of cable runs to the receive channels. The sensitivity to cross talk of this pairing scheme is shown in Figure 3.12 for a beam steered 30° away from broadside ($\phi = 60^\circ$) at varying levels of cross talk power.

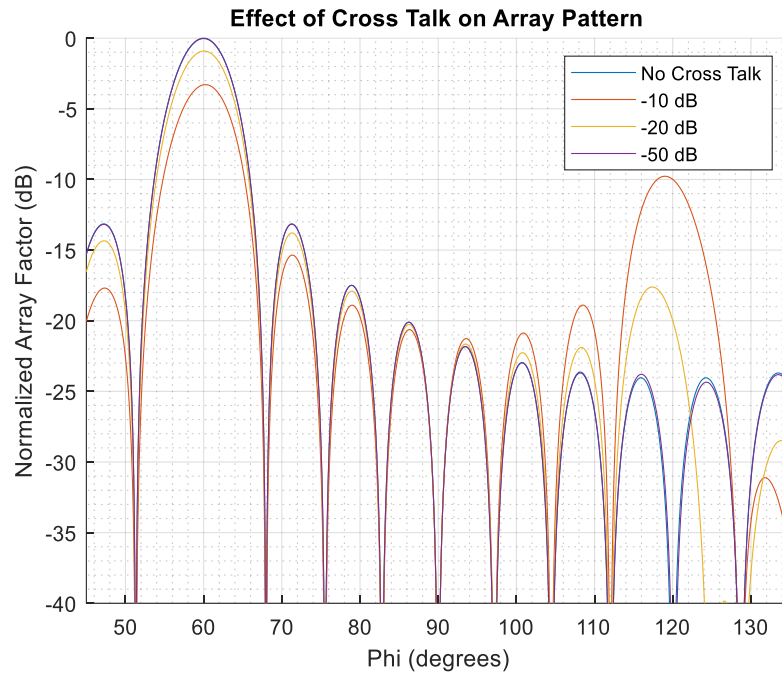


Figure 3.12. Effect of Cross Talk on Adjacent Pairing Scheme

As seen in Figure 3.12, the performance of the digital beamformer experiences minimal disturbance for a cross talk power of -50 dB and significantly degrades with increasing cross talk power. From the figure, it is apparent that the array factor experiences two distinct forms of degradation. First, the gain of the main lobe of the array pattern is reduced. As previously

discussed, any reduction in the antenna gain will result in a reduction in the received power. Thus, with the same signal to noise ratio requirement, the maximum range of the radar system will be reduced. Using the radar range equation for beam-filling targets, the new maximum range due to loss of gain was calculated for each of the cases in Figure 3.12. In this calculation, the loss of receive antenna gain is represented by a reduction in the effective area of the receive antenna (A) [10].

Cross Talk Power (dB)	Gain Loss (dB)	Range Reduction (dB)	Relative Maximum Range (%)
-10	3.3	1.65	68.4
-20	0.9	0.45	90.2
-50	0.03	0.015	99.7

Table 3.1. Reduction of Maximum Range Due to Cross Talk

Thus, cross talk introduces a reduction in the maximum range of the radar system. Due to the extended propagation distances available to the SuperDARN radars through sky-wave propagation, even small percentage reductions correspond to large differences in physical range. For instance, the Blackstone SuperDARN radar operating with 100 range gates and a 2400 μ s delay to the first range gate has a maximum range of 4860 km. Therefore, even a one percent reduction in range corresponds to 48.6 km of data that is no longer available. Additionally, all ranges still experience a reduction in the signal to noise ratio decreasing the measurement quality.

The second form of degradation of the array factor comes from the introduction of grating lobes and increased sidelobe power. In Figure 3.12, a prominent grating lobe appears at approximately $\phi = 120^\circ$ for the cases of higher cross talk power. In terms of the radar system performance, this grating lobe would introduce a directional ambiguity. A strong target or clutter source present in this grating lobe would appear to the radar as a target from within the main lobe of the antenna pattern. Depending on the strength of the grating lobe and the interference source, this would also significantly diminish the signal to interference or signal to clutter ratio thereby increasing the number of missed or false detections.

The extent of these two issues also varies across the radar field-of-view. As the antenna beam is steered, the weighting of the elements within the antenna array changes and the phase delays in the steering vector are also changed. Therefore, different interference occurs between the desired signal and the cross-talk. Several plots are shown in Figure 3.13 representing the array factor degradation for various steering angles. In this figure, a cross talk power of -10 dB was used in order to accentuate the variation with respect to the beam direction.

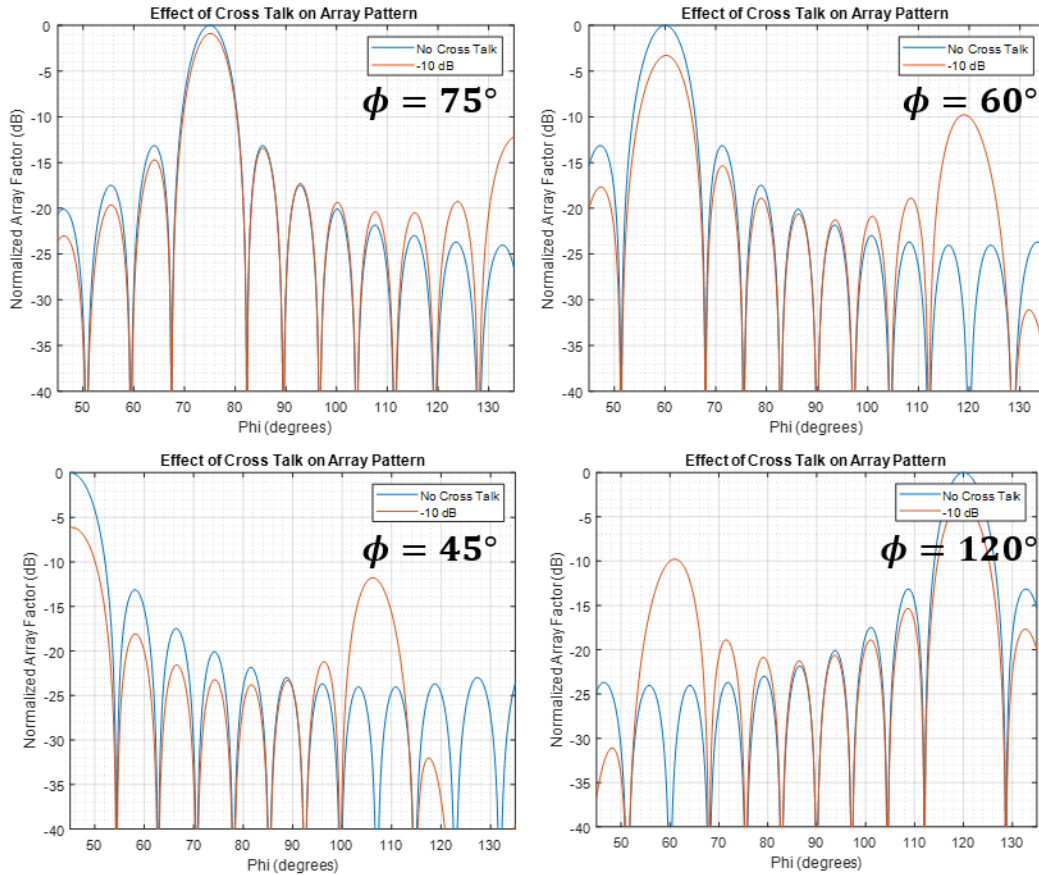


Figure 3.13. Variation with Respect to Beam Direction for Adjacent Pairing

The extent of the gain reduction and grating lobe power vary significantly across the radar field-of-view. At a 45° angle off broadside, the main lobe gain is reduced by over 5 dB representing a massive reduction in the maximum range. Meanwhile, at a 15° angle off broadside, the main lobe gain is only reduced by less than 3 dB. Due to the significant variation in performance across the range of look directions, any chosen pairing scheme must be tested for each possible steering direction within the radar field-of-view.

In order to better understand how the cross talk interferes with the desired array factor, it is helpful to consider the two superimposed array factors which produce the effective array factor as shown in the equation below:

$$AF_{eff} = \alpha AF + \rho AF_2 \quad (3.22)$$

The first array factor corresponds to the case where no cross talk exists, and the second array factor corresponds only to the results of the cross-weighted cross talk power. These two array factors are shown in Figure 3.14 for a look direction 30° off broadside.

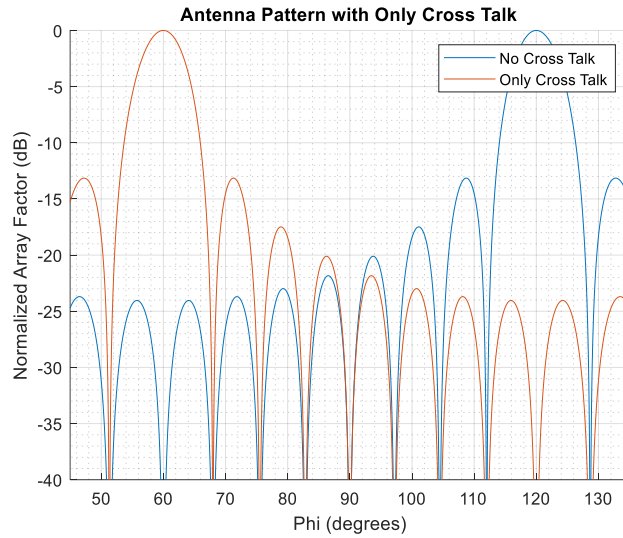


Figure 3.14. Array Factors for Adjacent Pairing Approach

These two array factors are significantly offset and share no overlapping of the main beam. As a result, the two array factors effectively compete for control of the effective array factor resulting in the reduced main lobe and increased grating lobe seen in the previous figures. In an ideal case, these two array factors would match perfectly across all different look directions within the field of view. This work explored alternative pairing schemes in order to vary the cross-weighting scheme that control the cross talk array factor in an attempt to approach this ideal case. These results are included in Appendix I. Ultimately, the cross-talk power of -50 dB found in the Red Pitaya had a negligible effect on the array factor within the radar field-of-view for all pairing schemes considered.

3.5 Front End Design

The next obstacle to implementation of a prototype radar receiver using the Red Pitaya was the need for external front end circuitry. In a software defined radio receiver, an ADC digitizes the signal and some aspects of the signal processing are implemented in the digital domain. For this design, the Red Pitaya was used in a direct conversion architecture where the signal is digitized before any mixing or frequency conversion is applied. Then any necessary frequency conversion, filtering, demodulating, and amplification are implemented in the digital domain as shown in Figure 3.15.

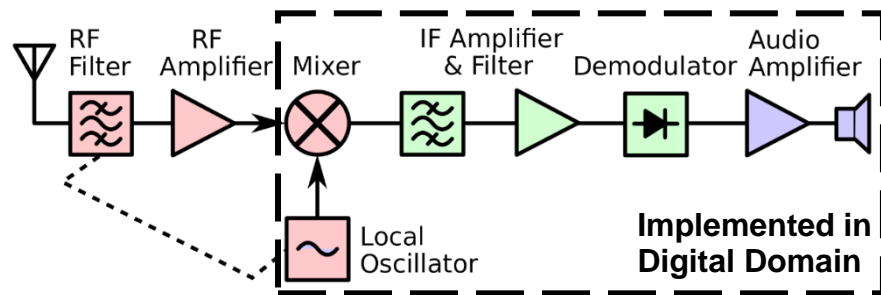


Figure 3.15. Modified Superheterodyne Block Diagram for Direct Conversion SDR [13]

Not all elements of the receiver design can be moved into the digital domain. As seen in Figure 3.15, the antenna, RF preselection filter, and RF low noise amplifier (LNA) are still implemented in the analog domain. The LNA is critical in reducing the system noise figure as ADCs, including the Red Pitaya ADC as shown previously, typically have very high noise figures. The preselection filter improves the suppression of strong out of band sources of interference which improves the linearity by preventing intermodulation or compression from occurring in the LNA. In this case, the preselection filter and LNA constitute the “front end” of the receiver design. This work designed the following front end to accommodate a SuperDARN receiver using a direct conversion architecture with a Red Pitaya as the software defined radio.

3.5.1 Preselection Filter

The first element of the front end design seen by the received signal after the antenna is the preselection filter. The preselection filter primarily rejects strong out of band interferers in order to improve the linearity of the LNA and the ADC. The design attempted to maintain the “flexibility” of the SDR across the entire SuperDARN frequency range. Accordingly, this work designed the passband of the filter to cover the frequency range from 10 to 16 MHz to match the bandwidth of the SuperDARN twin terminated folded dipole arrays. Another option would have been to use a narrower filter that could be tuned to different center frequencies across the SuperDARN bandwidth. Passing the entire bandwidth was chosen in order to allow for techniques such as multichannel operation with the channelization being performed in the digital domain.

For this application, this work selected a third degree Chebyshev filter in order to have a controlled passband ripple while also having a steep filter roll-off. A passband ripple of 0.1 dB was chosen with a center frequency of 13 MHz and a passband bandwidth of 6 MHz. Since SuperDARN radars operate in the HF frequency range, a lumped element filter was constructed from discrete inductors and capacitors rather than a transmission line filter. The filter topology is shown in Figure 3.16 below.

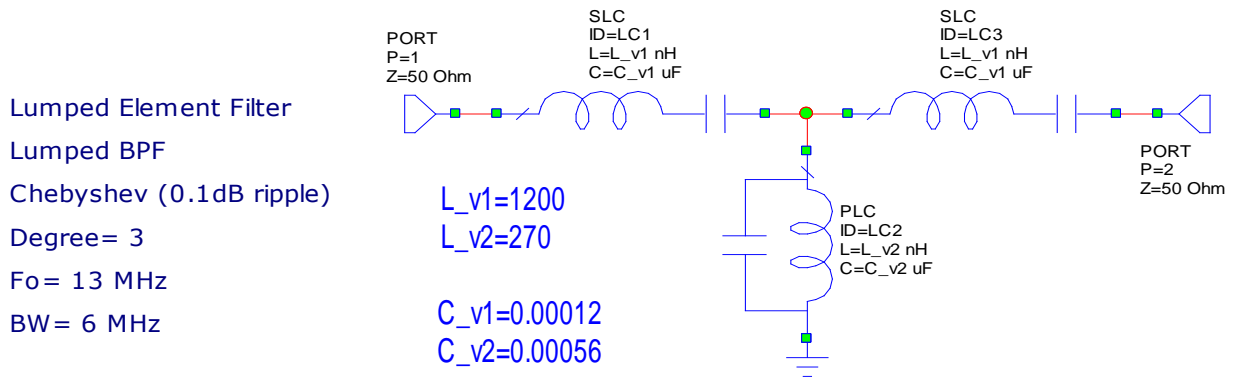


Figure 3.16. Bandpass Preselection Filter

After adjusting the design values to correspond with standard part values, the filter design produced the simulated frequency response shown in Figure 3.17.

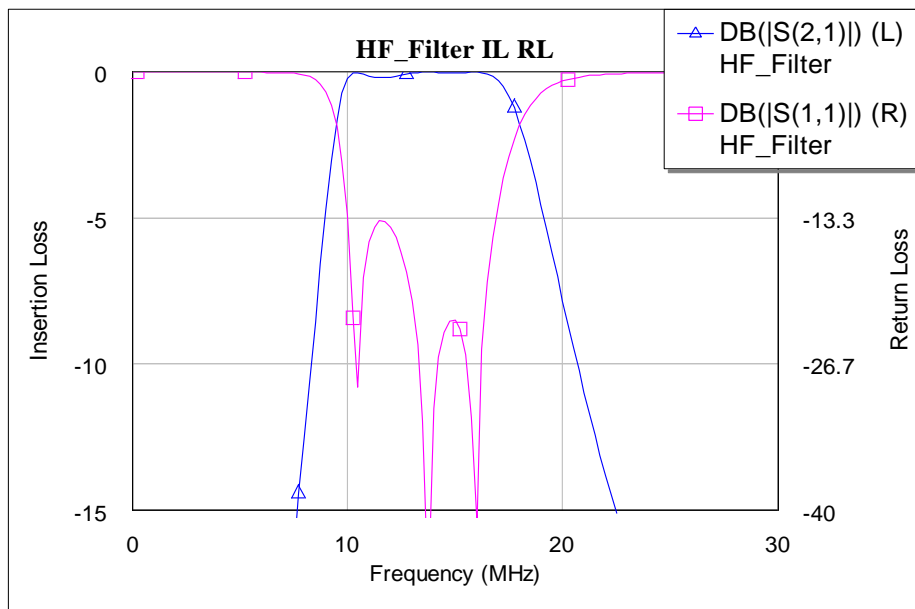


Figure 3.17. Frequency Response of Filter Insertion Loss (Blue) and Return Loss (Magenta)

This filter accomplished the design goals of a 0.1 dB ripple in the passband from 10 to 16 MHz. The filter also had a sharp roll-off allowing for adequate suppression of out-of-band interference.

3.5.2 LNA Selection

The next element in the front end signal path is the low noise amplifier. Based on a cascade analysis of the system, this work chose design requirements for the LNA including a noise figure of less than 3 dB and a gain of at least 15 dB. Additionally, the frequency response of the amplifier needed to cover the entire SuperDARN frequency range from 10 to 16 MHz in order to preserve the flexibility advantage of a software defined radio. Based on these desired specifications, this work chose the Qorvo AG303-86 low noise amplifier for the front end design. This amplifier provides a gain of 21.4 dB and a noise figure of 2.9 dB at typical operating conditions in the SuperDARN frequency range meeting the design requirements [27].

3.5.3 PCB Design and Implementation

There were several additional considerations in the implementation of the front end design. First, DC blocking capacitors were included to prevent damage either to the board due to external failures or to the SDR due to failures in the front end. The preselection filter already included series capacitors protecting the antenna side and another capacitor was added on the output side of the board. Additional protection circuitry included two antiparallel diodes placed at the output of the front end in order to protect the software defined radio from potential surges in RF power. A STMicroelectronics L78L05ABD13TR 5 V regulator provided the DC bias for the LNA.

This work implemented the front end design on a PCB made of FR4 with dielectric constant of 4.4 and a thickness of 1.6 mm. Microstrip transmission lines were used with a line width of 1.57 mm in order to achieve the desired line impedance of 50 Ω . All RF components were placed in a linear path to minimize the discontinuities in the microstrip line. The board layout, excluding copper pours for visibility of the traces, is shown in Figure 3.18.

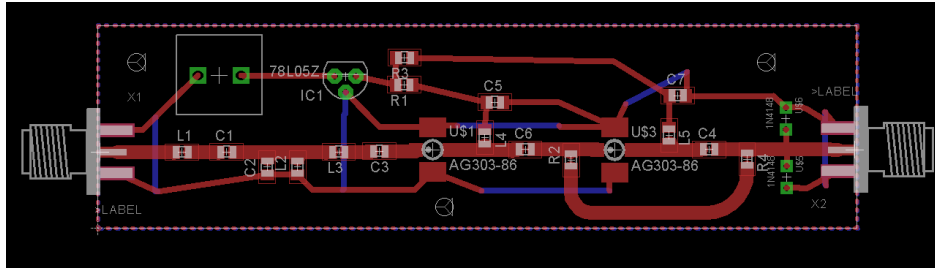


Figure 3.18. Front End PCB Design

Copper pours were added to the top and bottom layers, and no signals were routed on the bottom layer in order to ensure a continuous ground plane for proper microstrip line performance. The fully assembled front end is shown in Figure 3.19.

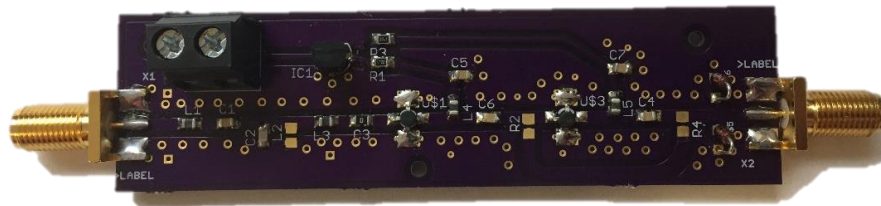


Figure 3.19. Assembled Front End Design

In order to validate the design, this work empirically evaluated the frequency response as shown in Figure 3.20.

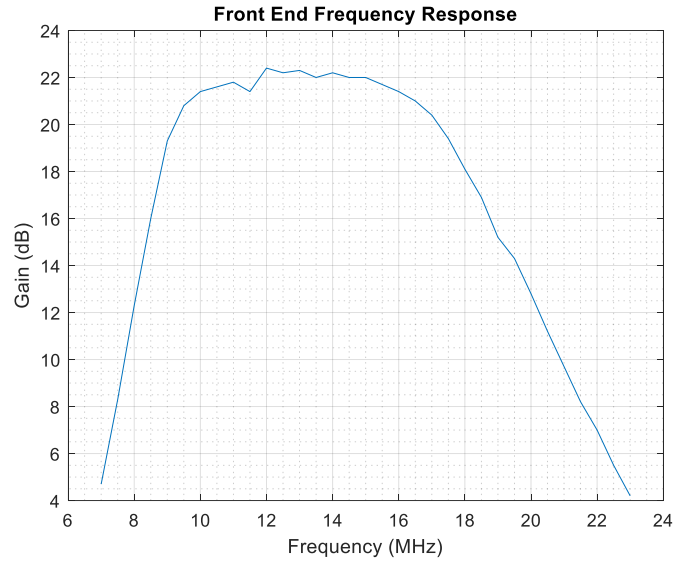


Figure 3.20. Front End Frequency Response

Some additional passband ripple occurred due to variations in capacitor and inductor values, parasitic PCB capacitances, and variations in the amplifier frequency response. Still, the passband frequency response is sufficiently flat over narrow frequency bands to allow for use in a SuperDARN radar.

3.5.4 Cascade Analysis

The overall system performance was obtained from a cascade analysis of the subsystems using Friis' formulas for cascaded gain, noise factor, and noise figure as shown in the equations below [12]:

$$G = G_1 G_2 G_3 \dots G_n \quad (3.23)$$

$$F = F_1 + \frac{F_2 - 1}{G_1} + \frac{F_3 - 1}{G_1 G_2} + \dots + \frac{F_n - 1}{G_1 G_2 G_3 \dots G_{n-1}} \quad (3.24)$$

$$NF = 10 \log_{10} F \quad (3.25)$$

The cascade analysis considered the preselection filter, with a loss of 0.1 dB corresponding to the passband ripple, the LNA with a gain of 21.4 dB and a noise figure of 2.9 dB, and the software defined radio's ADC with a noise figure of approximately 35 dB.

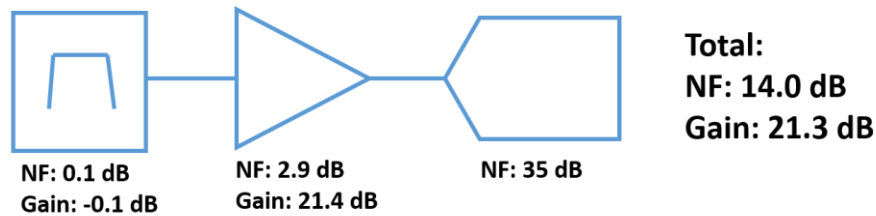


Figure 3.21. Cascade Analysis

The resultant noise figure of 14 dB was higher than ideal, but the opportunities for additional gain were limited by the direction conversion architecture. Reducing the LNA noise figure to 1 dB would only improve the system noise figure by 0.1 dB suggesting that the noise figure could only be significantly improved by changing the gain. However, adding additional gain to the existing front end stage would likely introduce oscillations. In a traditional front end design, gain is distributed across the radiofrequency and intermediate frequency stages to prevent such oscillations. Thus, the direct conversion architecture is potentially limited in terms of sensitivity. Overall, the linearity advantages of the direct conversion architecture outweighed its noise figure limitations.

This cascade analysis did not include the loss through the coaxial feed cable that runs from the antenna to the receiver, nor did it account for any potential losses through the transmit/receive switch. These losses were neglected in order to enable a direction comparison of receiver designs. An analysis intended to determine the complete radar performance should account for these losses. Ultimately, this front end design significantly improved the noise figure of a software defined radio receiver while maintaining the flexibility of SDR systems.

3.6 Receiver Synchronization

With the front end hardware and software defined radio selection complete, the next challenge in digitizing the SuperDARN array was to synchronize the various receive channels. Both of the receive channels on a single Red Pitaya receive their ADC clock signal from the same 125 MHz crystal oscillator. Sharing an ADC clock is important to ensure that both receive channels are operating at the same frequency as slight errors in frequency may exist between different oscillators. Additionally, the samples are guaranteed to occur at the same time except for slight differences in the delay of the feed line for the clock signal. This setup leaves three major sources of error between the two signals.

First, magnitude imbalances between the two channels will exist due to differences in the analog front end hardware, particularly in the 9:1 transformer used for impedance matching. Second, the n^{th} recorded sample on channel 1 is not guaranteed to correspond with the n^{th} recorded sample on channel 2 despite their shared ADC clock. This coarse time offset is a byproduct of the control software, in this case GNU Radio, which may not start both channels at the exact same time due to the limitations of the serial communication between the Red Pitaya and the control software running on a separate computer. Finally, a phase offset will exist due to differences in the analog components in both the RF front end and the feedline for the ADC clock signal.

3.6.1 Calibration Signal

In order to measure these errors and account for them in the signal processing chain, this work designed a calibration signal and calibration procedure. Ideally, a single wideband arbitrary noise source would provide ample information for a cross correlation to provide the relevant offsets, but this testing was limited to a pulsed continuous wave source from an available

laboratory signal generator. Instead, the designed signal has three distinct sections, each designed to address one of the three sources of error described above. The calibration pulse consisted of nine seconds at an amplitude well below the one dB compression point of the Red Pitaya, followed by one second of no forward power, and then another 5 seconds at the previous amplitude. This signal, as recorded by the two channels of the Red Pitaya, are shown in Figure 3.22.

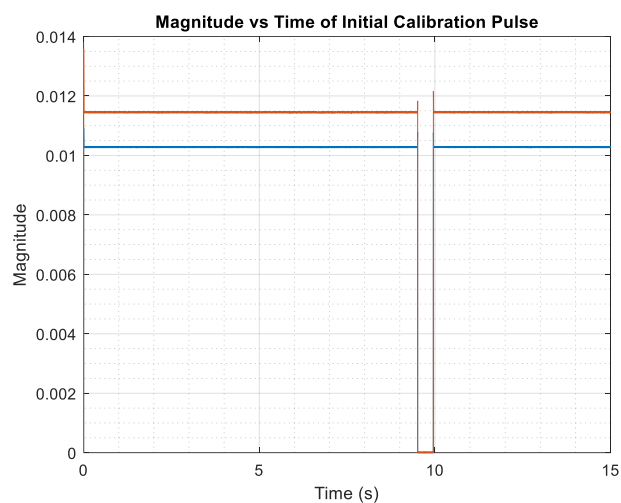


Figure 3.22. Calibration Pulse Magnitude

The first section served to allow adequate time for transient oscillations to fade, and then allowed for the magnitudes of the two channels to be equalized. The second stage provided sharp transitions that are used for the coarse time alignment, similar to synchronization techniques in serial communication protocols like I2C. Finally, the last section provided the opportunity to examine the phase offset between the two channels.

A closer look at the two recordings of this calibration signal demonstrates both the magnitude imbalance and the coarse time offset between the two signals. Figure 3.23 shows a clear difference in the amplitude of the two signals prior to the sharp transition. Additionally, the

figure shows a substantial difference in the observed time at which the transition occurs. The following sections demonstrate how these issues were corrected.

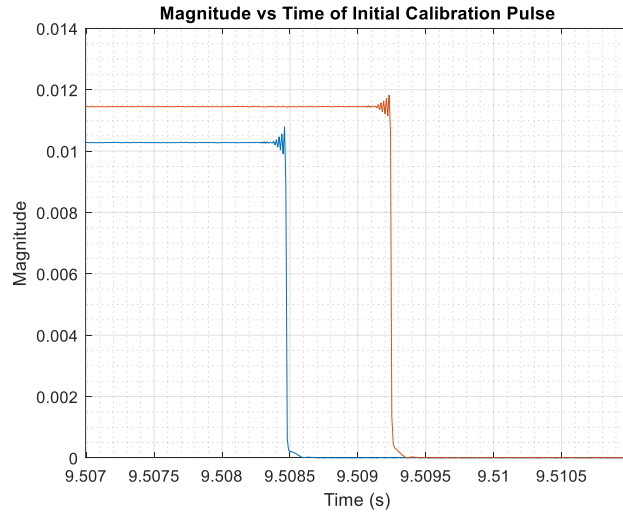


Figure 3.23. Demonstration of Magnitude and Coarse Time Errors

3.6.2 Magnitude Calibration

As detailed in the prior section, the first stage of the calibration signal was designed to allow for magnitude calibration. The objective of this section was to determine a scaling factor that can be applied to the second signal such that it will match the amplitude of the first signal. Figure 3.24 below shows the magnitudes over the period from 2 to 8 seconds. Only the data from this time interval was used in the calculation of the scaling factor.

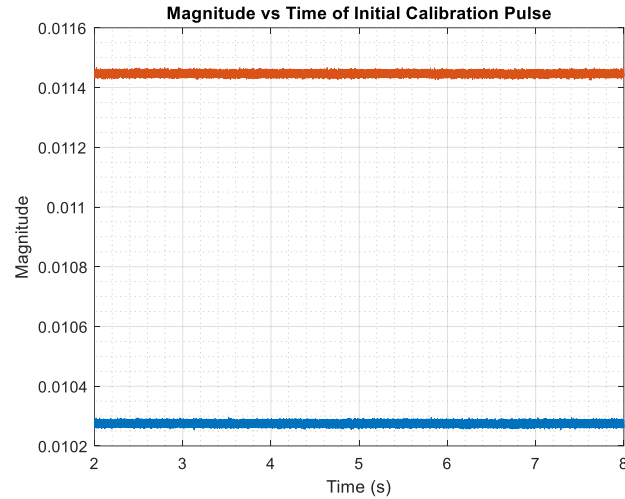


Figure 3.24. Magnitude Calibration Time Interval

The procedure for calculating the scaling factor (r) consisted of integrating the magnitude values over both signals over this interval and finding the ratio between them as described in the equations below:

$$A_1 = \Sigma|s_1|; A_2 = \Sigma|s_2| \quad (3.26)$$

$$r = \frac{A_1}{A_2} \quad (3.27)$$

$$s_{2,eq} = r s_2 \quad (3.28)$$

Thus, the second signal was scaled by a ratio factor in order to correct for the magnitude imbalance between the two channels. The plot of the scaled signals, shown in Figure 3.25, demonstrates that the magnitude error has been corrected.

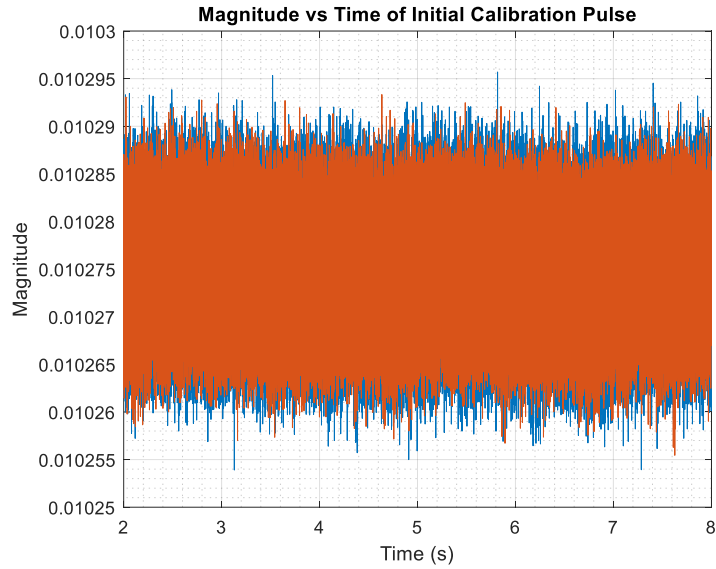


Figure 3.25. Calibration Signals with Magnitude Corrections

3.6.3 Coarse Alignment in Time

After achieving the magnitude equalization, the next step in the calibration procedure was to adjust for the coarse time offset that was evident in Figure 3.23. It is necessary to complete the coarse time calibration before attempting the phase calibration in order to resolve 2π phase ambiguities. This alignment was achieved by shifting the second signal by the appropriate number of lags or samples. In order to compute this lag difference, a cross correlation was calculated from the two signals. The peak intensity of the resultant lag-correlation plot, as shown in Figure 3.26 below, provided the relative delay between the two signals.

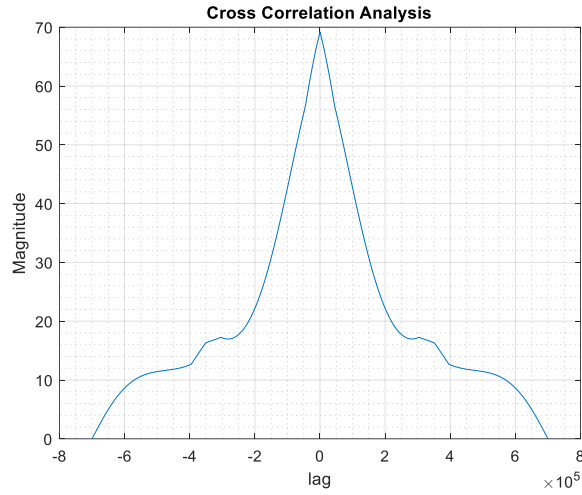


Figure 3.26. Cross Correlation Analysis of Delay Time

This calculation used the time interval between six and thirteen seconds because this period featured the two sharp transitions which help demonstrate the alignment in time. After applying the appropriate time delay and magnitude scaling, the resultant signals were closely synchronized as shown in Figure 3.27 and Figure 3.28 below.

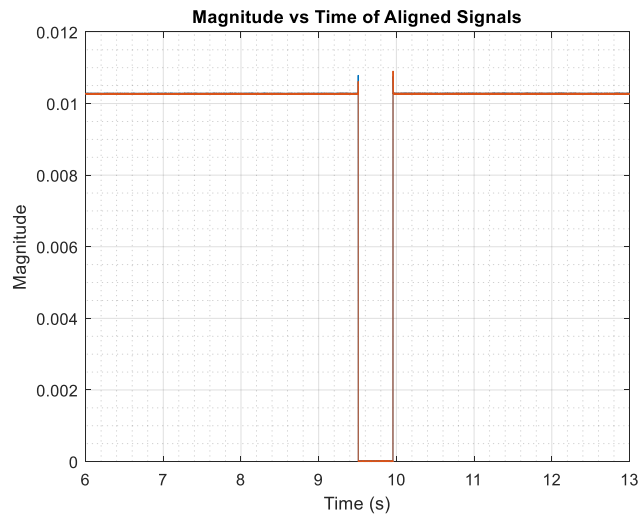


Figure 3.27. Magnitude of Calibration Signal After Coarse Alignment

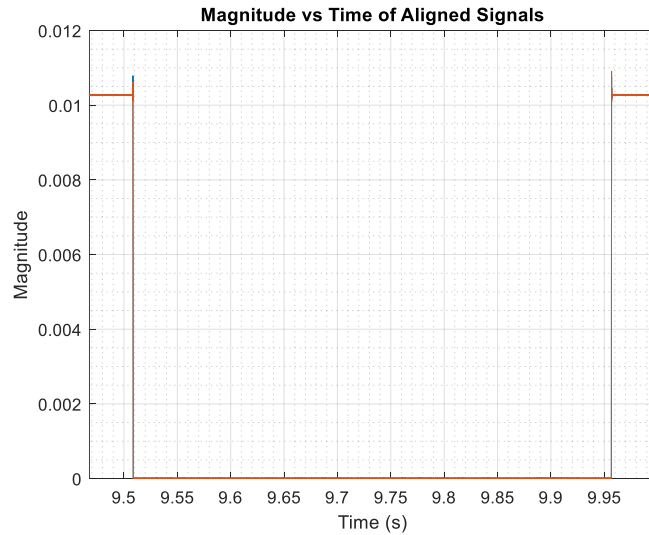


Figure 3.28. Synchronization of Transition Edges After Coarse Alignment

A closer look at the first transition edge, as shown in Figure 3.29, accentuates just how closely the signals became synchronized through the first two steps of the calibration process. However, some discrepancies between the two observed signals still existed due to the stochastic nature of the thermal noise in each channel.

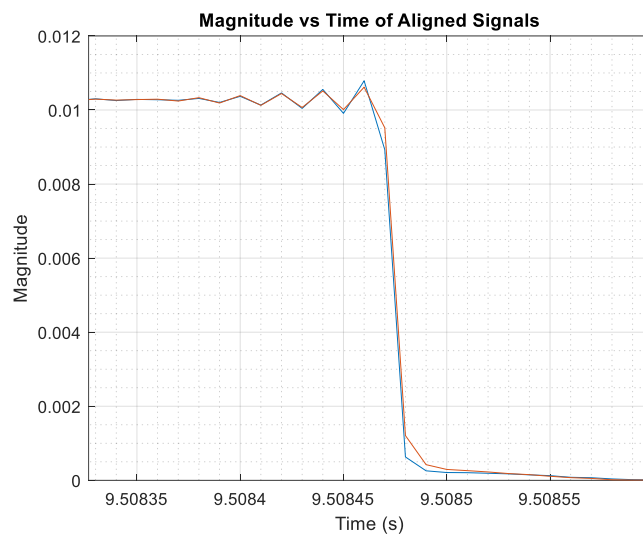


Figure 3.29. Sample by Sample Measurement of Transition Edge After Coarse Alignment

3.6.4 Phase Synchronization

The previous plots have only shown calibration errors in the form of magnitude differences between the two recorded signals. The final stage of the calibration procedure was to correct for the phase offset between the two channels due to the variation in the analog components in the RF front end of the software radio. In order to analyze the phase error, the signals were first scaled and aligned as discussed in the previous two sections. Then, the phase angle of the complex voltage of each sample was calculated for each signal. The difference between the two phase measurement angles at a given sample index provided the phase error at a given point in time as shown in Figure 3.30.

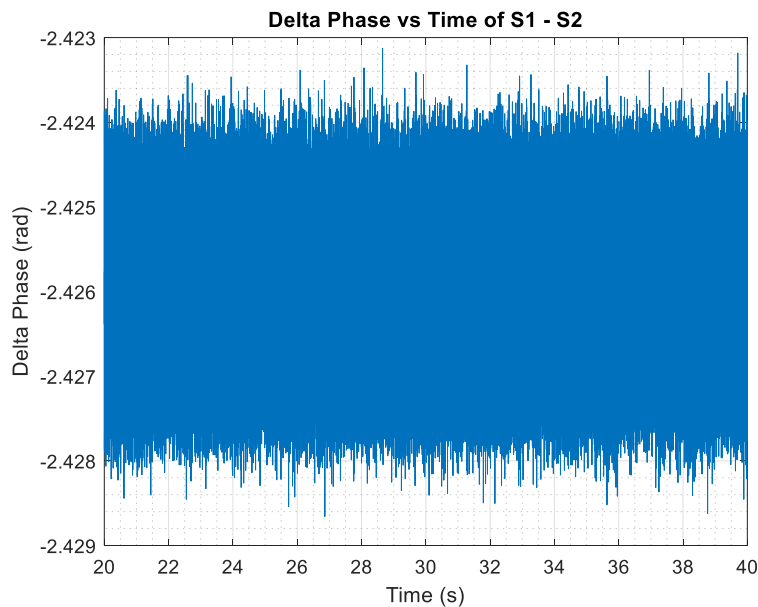


Figure 3.30. Phase Difference vs Time

There was a large, but relatively fixed, difference in the phase measurements of the two received signals. In this particular instance, this work found the average phase difference over this portion of the calibration signal to be -2.43 radians. After adjusting the signals for this offset, the

phase difference of the calibrated signals over the same period was calculated and is shown in Figure 3.31.

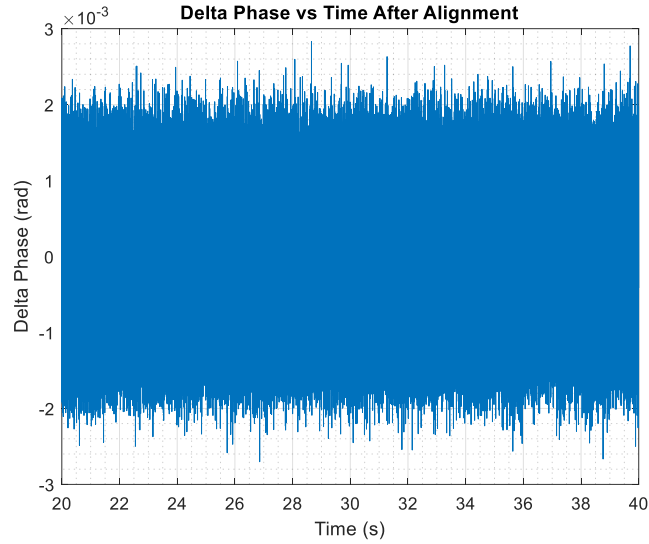


Figure 3.31. Phase Difference vs Time of Synchronized Signals

It is important to note that errors in the phase difference still occur due to the stochastic nature of the noise, but the average maximum phase difference is now constrained to thousandths of a radian.

3.6.5 Long-Term Stability of Cancellation Ratio

While the magnitude and phase difference plot shown in the sections above demonstrate the improvement of the calibration, they do not provide a useful interpretation of how the remaining calibration errors will affect the performance of the system. One method of studying this effect is calculating the cancellation ratio as defined in the equation below:

$$CR [dB] = 20 \log_{10} \frac{|s_{1,cal} - s_{2,cal}|}{|s_{1,cal}|} \quad (3.29)$$

Thus, the cancellation ratio represents the remaining power (ideally due only to thermal noise) after calculating the difference between the two calibrated signals. Thus, the ideal cancellation ratio would be $-\infty$ dB corresponding to zero difference in the two signals. The cancellation ratio over the time interval used in the phase synchronization is shown in Figure 3.32.

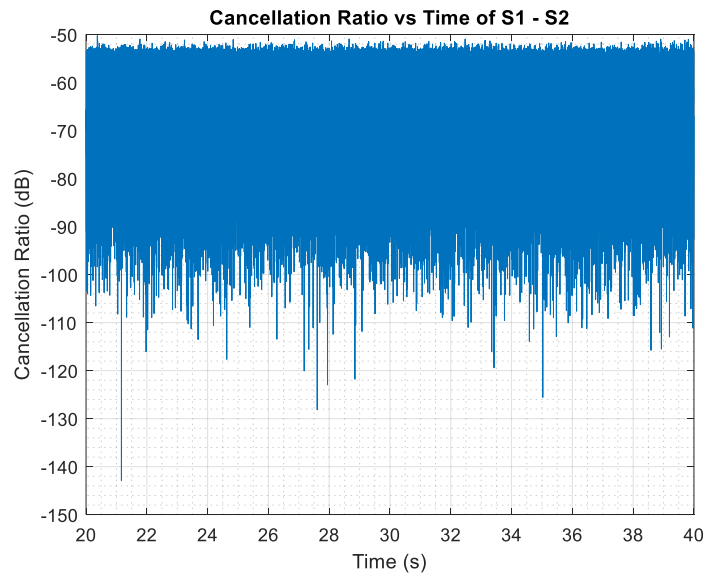


Figure 3.32. Cancellation Ratio After Synchronization

A worst case cancellation ratio of -50 dB shows that any remaining differences between the two measured and calibrated signals is likely to be negligible when compared to the thermal noise power in the system which ought to be the dominant source of error.

The final objective of this project was to examine the performance of the calibration over extended periods of time. It was anticipated that the calibration could degrade over time due to fluctuations in the magnitude and phase response of the analog components in the parallel RF front end paths, particularly due to thermal effects.

In the case of the SuperDARN system, the radar scans the entire field of view over the course of two minutes. Thus, any system must maintain its calibration over at least a two minute interval, but ideally for ten minutes in order to allow for several scans to be completed. Therefore, after allowing a “warm-up” period of five minutes for the device to reach its normal operating temperature, this work recorded samples for approximately 10 minutes. After applying the calibration routine described in the previous sections, the cancellation ratio was calculated at one second intervals for the remainder of the recorded signals. The results of this study are shown in Figure 3.33.

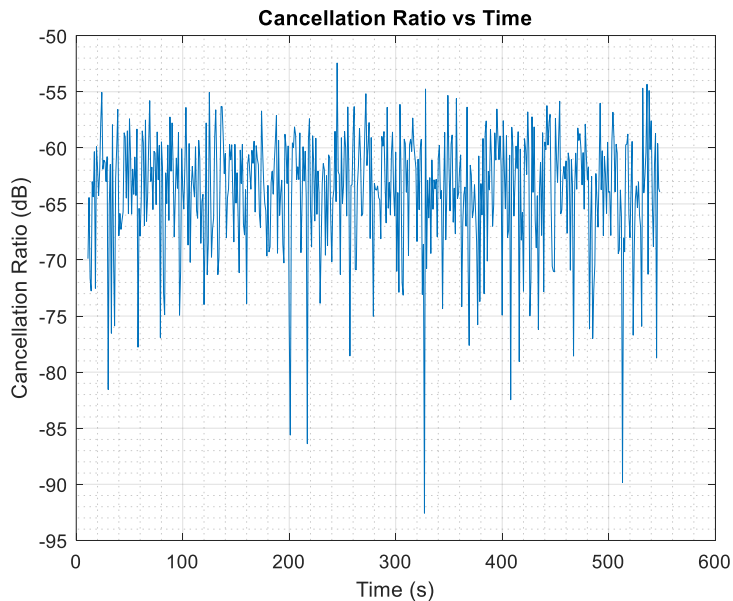


Figure 3.33. Cancellation Ratio vs Time

The Red Pitaya maintained its synchronization over the approximately 10 minute period demonstrating that this calibration routine would be sufficient for implementation as part of the SuperDARN operating procedure.

3.6.6 Clock Distribution for Multiple Channel Synchronization

The receiver synchronization becomes more complex when considering all 16 receive channels. Since different devices do not inherently share the same ADC clock, additional clock distribution circuitry is required to ensure synchronization. The default Red Pitaya ADC clock is derived from a 125 MHz crystal oscillator. This oscillator provides a low-voltage differential signaling (LVDS) output which is fed into the Red Pitaya's two channel ADC. The ADC then passes the clock signal to the Xilinx Zynq SoC which provides the DAC clock. Since the two receive channels are processed by the same ADC chip with the same ADC clock input, their samples will share the same period thereby ensuring that the two channels have no offset in frequency.

In order to achieve digital beamforming with a SuperDARN antenna array, 16 channels need to be synchronized. Such a system would require eight Red Pitaya devices, each with two transmit and two receive channels. The same calibration techniques used for synchronizing two channels can be applied across the entire array if all the channels share the same frequency offset. This shared frequency offset can be achieved if all the channels share a common ADC clock. In order to demonstrate this capability, a prototype clock distribution system was developed for a four channel receiver.

The task of feeding an external clock to the Red Pitaya's ADC is simplified by the device's configuration. While the default configuration uses an on-board crystal oscillator to generate the ADC clock, the device can be reconfigured to accept an external ADC clock by moving two resistors to disconnect the existing the oscillator. The external ADC clock is passed to the Red Pitaya through the header pins along the side of the board designed to fit to a ribbon cable.

LVDS traces are designed to use controlled impedance differential pair transmission lines.

Accordingly, header pins and ribbon cable are less than ideal for connecting to an external LVDS

source. For this prototype, the header pins were kept in order to preserve the functionality of the remaining pins and the length of the attached cable was minimized. At 125 MHz, the corresponding wavelength is 2.4 meters; therefore, an electrically short cable ($l < 0.1\lambda = 24 \text{ cm}$) should have a minimal impact on the system performance [28]. Utilizing twisted or braided ribbon cable can also improve the performance by ensuring the differential lines are effected equally by electromagnetic interference. Future iterations may benefit from removing the header pins, attaching a twinaxial connector to the Red Pitaya, and using impedance controlled twinaxial cable to connect to an external clock source.

This work designed a clock distribution board to generate and distribute an LVDS to two Red Pitaya devices. The essential aspects of this design are the clock selection, LVDS splitter, and the power supply. The default Red Pitaya oscillator is the TXC Corporation BF-125.000MBE-T which has a frequency stability of ± 50 ppm. A high stability oscillator was used for the external clock source in order to ensure that approximately the same quality was observed after skew and distortion due to the splitter, PCB traces, and cabling. This work selected the Microchip Technology DSC1103NI2-125.0000, which has a frequency stability of ± 25 ppm, as the source for the clock distribution board [29]. Other factors in its selection were cost and size (this work attempted to choose components large enough to be assembled by hand).

A splitter was needed in order to provide the appropriate output signal level and impedance to both Red Pitayas while also providing the correct load impedance to the oscillator. For this design, this work chose the Maxim MAX9175EUB+ LVDS splitter. The delay time through the splitter was not critical for this application, but the MAX9175EUB+ offers a low delay time of 2.39 ns and a current draw of 25 mA [30].

Both the Maxim splitter and the Microchip oscillator can be run on a +3.3V power supply simplifying the design of the board. To further simplify design, the power to the board was provided by an external DC power supply connected through a screw terminal block. This 3.3 V supply was also filtered by 0.1 μf bypass capacitors placed as close as possible to the oscillator and splitter. The capacitor placement can be seen in the PCB layout in Figure 3.34.

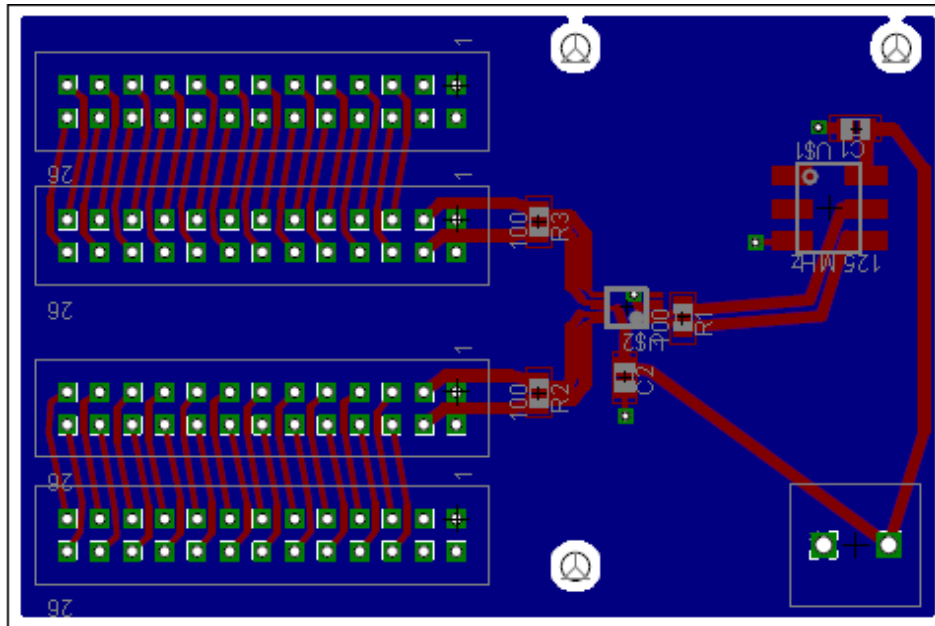


Figure 3.34. Clock Distribution Board Layout

The clock distribution board was fabricated as a two layer board on a FR4 substrate with a dielectric thickness of 1.6 mm. Both the substrate material and thickness are accounted for in the design of the controlled impedance differential traces used for the LVDS paths. Edge coupled differential microstrip transmission lines were used with a target differential impedance of 100 Ω . For FR4 with a relative permittivity of 4.4, a satisfactory differential impedance of 120 Ω was achieved for a microstrip width of 0.8 mm with a spacing of 0.3 mm. This work used a non-ideal line impedance as the result of spatial limitations particularly as the traces converge on the

pins of the splitter and oscillator. Additionally, $100\ \Omega$ termination resistors were placed at the input to the LVDS splitter and at the output of the clock distribution board.

Another important consideration for the layout of the LVDS lines was the path length. Any difference in the path lengths of the CLK+ and CLK- lines will introduce clock skew and diminish the accuracy of the sample and hold times within the ADC. Any difference in the path lengths for the two Red Pitayas will result in an additional time offset between the two devices. Clock skew was mitigated by meandering the LVDS paths in order to achieve minimal difference in path length and clock skew. At the same time, sharp angles in the paths were avoided in order to minimize discontinuities in the impedance of the lines.

Connections for the remaining unused pins were also broken out in order to ensure that these pins could be used as needed due to the prototype nature of this design and to provide a simple method for sharing a common ground reference. As mentioned previously, future designs may remove these headers in favor of a twinaxial connector if these connections are not needed.

Additionally, future designs may incorporate a GPS disciplined oscillator (GPSDO) in order to facilitate the use of the array in a bistatic system requiring common timing across large distances. Ultimately, this clock distribution design and synchronization procedure enabled the design of a multi-channel radar receiver using a Red Pitaya software defined radio.

3.7 Test Results from Blackstone Radar

The final stage of this prototype development was to compare the performance of this multi-channel receiver against the existing SuperDARN hardware. A test was conducted at the Blackstone, VA SuperDARN radar on the afternoon of April 5, 2019 using the prototype SDR receiver. This test used a four-channel receiver prototype incorporating the Red Pitaya, front end board, and clock distribution board as described in the previous sections. Three of these channels were connected to separate elements of the interferometry array. By using the receive-only interferometry array, the main array receiver was not disrupted allowing the receive data from this prototype to be directly compared against the data received by the main array during the same test interval. However, the main array did have the benefit of superior gain due to using 16 antenna elements compared to the 3 antenna elements used by the prototype receiver.

The fourth channel was coupled to the radar's transmit signal in order to provide a reference when calculating the correlation of the radar returns. Each of these channels recorded IQ data at a sampling rate of 50 kHz. The ADC clock provided by the clock distribution board ensured a common frequency reference. For this experiment, the radar was set to sound continuously on Beam 11 (nearly broadside radiation), at 10.225 MHz for a period of 5 minutes. This mode used 7 second integration periods. The two Red Pitayas were networked with a host computer through a router, and all filtering and signal processing was performed on the host computer.

Figure 3.35 below shows the magnitude of the IQ data received by a single receiver channel over the duration of two pulse sequences (~260 ms). The distinctive 8 pulse sequence of the SuperDARN 'katscan' mode can be seen in this data. The strong pulses are the result of leakage of the transmit signal into the receiver.

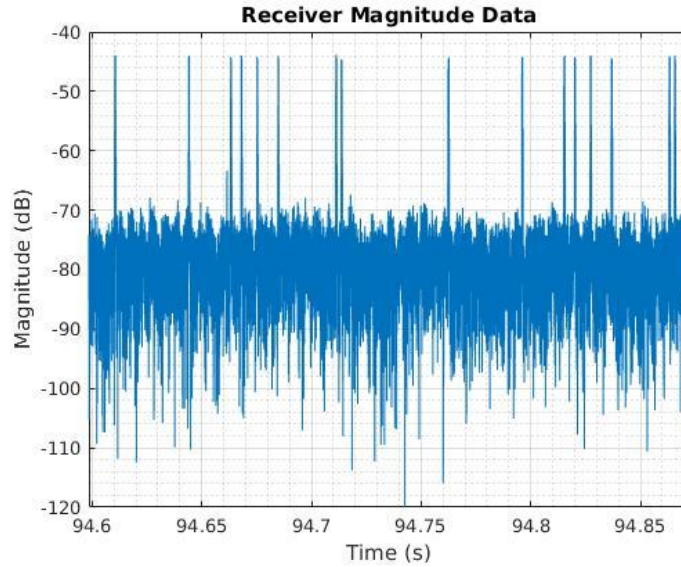


Figure 3.35. Two Pulse Sequences Shown in Single Receiver Data

This experiment used the leakage of the transmit signal into the receivers to achieve synchronization in time. Figure 3.36 shows the magnitude data from the three interferometry array channels and their corresponding sum channel over a period of 7 ms.

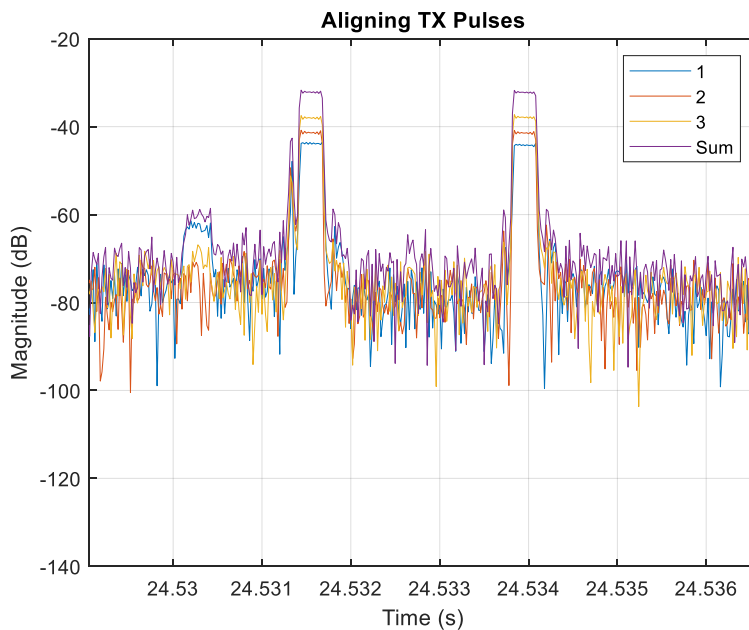


Figure 3.36. Synchronization of Receive Channels

In this figure, the two large pulses correspond to leakage of the transmit signal either through interaction of the main and interferometry array or through RF noise in the electronics room. The first pulse is relatively small and noisy indicating it is an echo from a scatterer. Figure 3.36 shows the synchronization between the three channels leading to constructive interference on summing. This sum signal or sum channel was also synchronized with the transmit signal recorded by the fourth channel as shown in Figure 3.37.

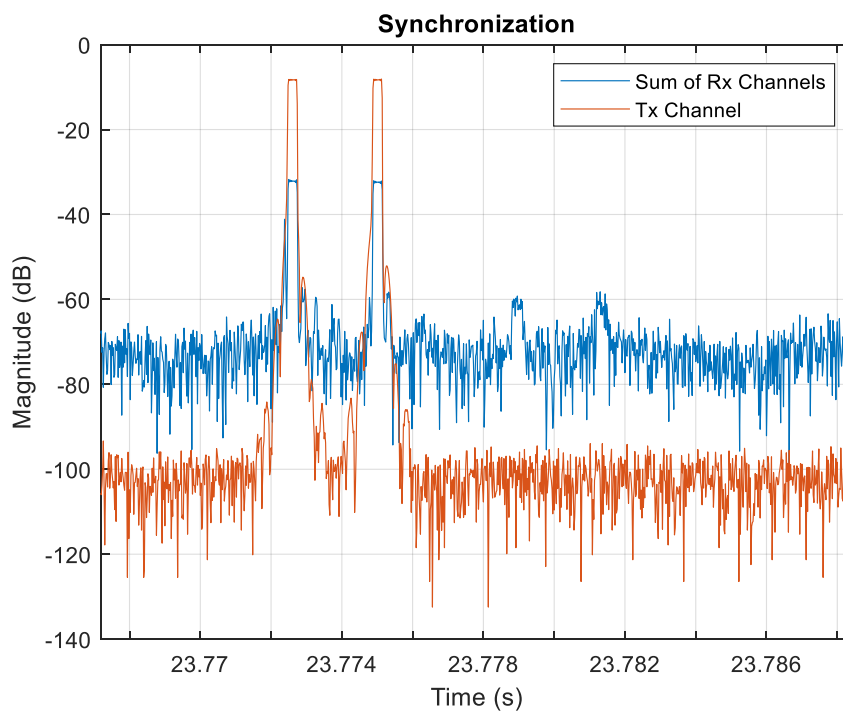


Figure 3.37. Synchronization of Recorded TX and RX Signals

The alignment of the transmit pulses in the transmit and receive channel data allowed for accurate calculation of the delays, and therefore ranges, of the received echoes. The presence of the transmit signal in the receive channels did introduce interference which was resolved by implementing receiver blanking digitally as shown in Figure 3.38.

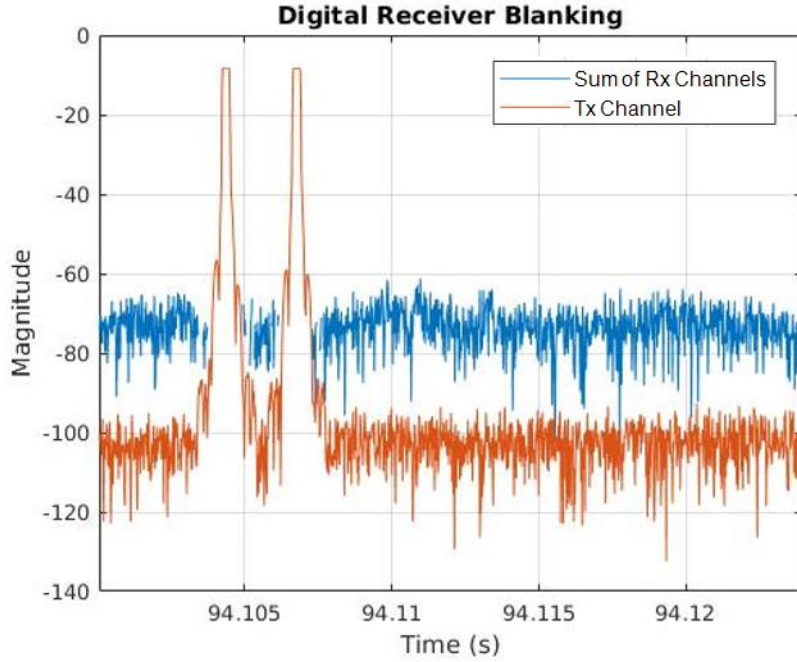


Figure 3.38. Digital Receiver Blanking

The receive channel signal power was replaced with nulls during transmissions. In order to process radar returns, the data was subdivided into 7 second intervals corresponding to the processing intervals used by the main array. This work calculated the cross correlation (\hat{R}) between the recorded transmit signal and recorded receive signal to obtain the power as a function of time and range. The calculation proceeds according to

$$\hat{R}_{RxTx}(m) = \sum_{n=0}^{N-m-1} (Rx)_{n+m}(Tx)_n^*, m \geq 0 \quad (3.30)$$

The results are shown in Figure 3.39 in the form of a range-time plot.

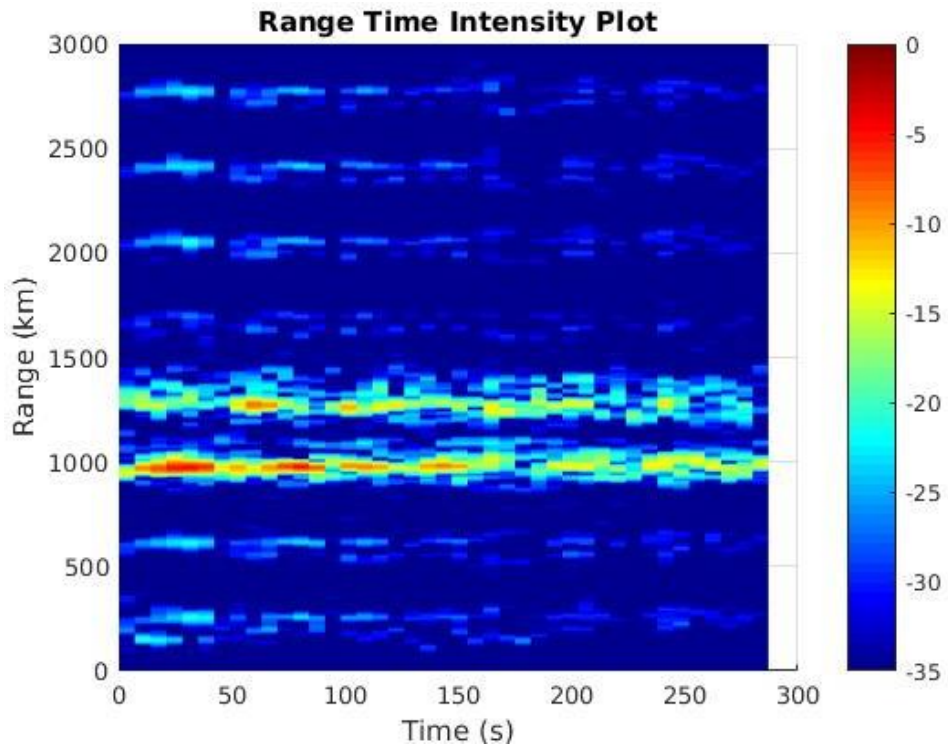


Figure 3.39. Range Time Intensity Display of Prototype Data

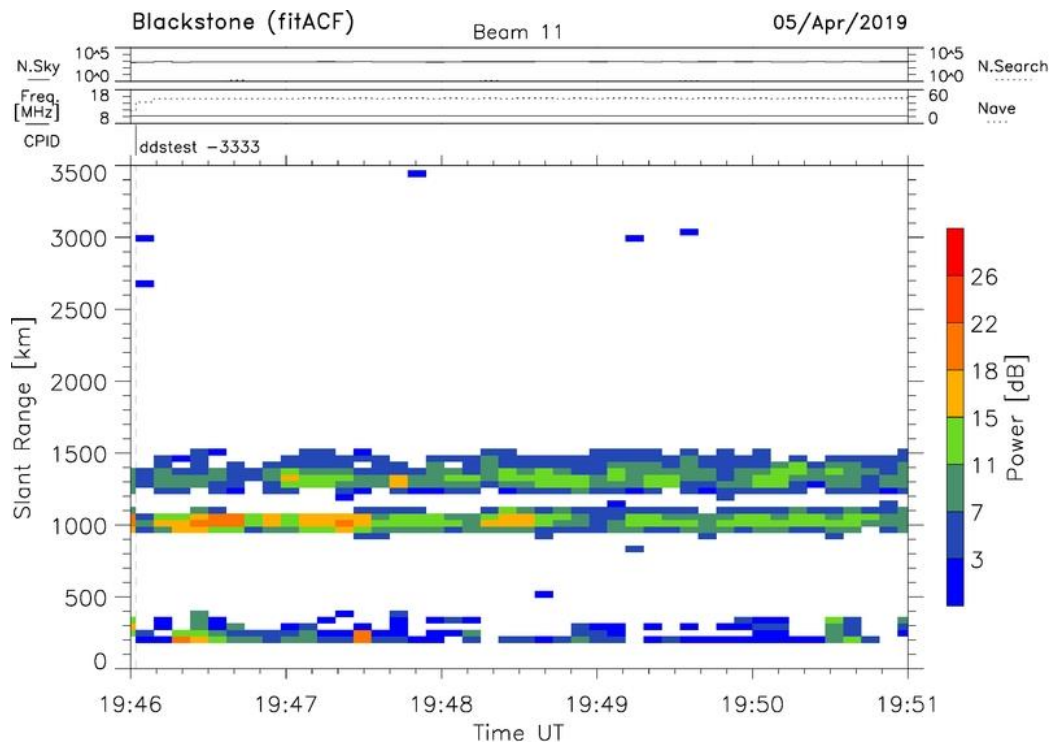


Figure 3.40. Range Time Intensity Display of Main Array Data

Here, each column represents a 7 second integration period. Each sample in range corresponds to a time delay. The intensity is represented on a relative dB scale. From these results, the highest power returns are almost 30 dB above the apparent noise floor. The two bright bands at approximately 1000 km and 1350 km represent ground scatter and are consistent with measurements taken before and after this experiment. The lighter bands are due to cross-range interference and are an artifact of the signal processing. The multipulse sequence produces range ambiguities which are resolved in the traditional SuperDARN signal processing through lag analysis. The straightforward calculation of cross-correlations applied here to the data from the receiver prototype does not resolve the issues with cross-range interference. However, no aspect of the prototype prevents future work from using existing techniques to eliminate cross range interference.

Since the main array was also functioning during this test, the prototype results can be confirmed by comparison with the results of the main array shown in Figure 3.40. The prototype receiver and the main array produce similar results. In particular, the bands of ground scatter at 1000 km and 1350 km are present in both sets of results. Both figures also show a gradual decay in scatter power as time increases. Interestingly, both results show similar signal to noise ratios despite the main array having a significant gain advantage due to the greater number of antenna elements. However, the additional antenna gain does allow the main array to observe an additional scatter band at 250 km with a weak SNR that is not visible in the prototype results. Ultimately, this test demonstrates that the low-cost prototype four-channel SDR receiver can be applied to collect useable data from the SuperDARN antenna system and opens possibilities for newer, more flexible receiving modes.

Chapter 4. Future Work and Conclusions

4.1 Future Work

Having motivated the benefits of adopting a SDR system and having successfully demonstrated a low-cost prototype, numerous options exist for expanding upon this work. The first step would be to continue the prototype development to accommodate 16 channels, allowing the prototype to be tested along the entire main array. Testing using the full main array would enable verification of the transmit functionalities of the Red Pitaya as well as experiments incorporating the techniques described in the second chapter of this work.

Future hardware work, beyond accommodating 16 channels, should include GPS synchronization in the clock distribution design in order to accommodate future bistatic radar operations. Future work should also consider the long term reliability of the Red Pitaya device, particularly due to thermal issues. Forced convection may be necessary in order to achieve adequate cooling through the FPGA heatsink during continuous operation. In that vein, the manufacturers of the Red Pitaya have also announced a new model designed specifically for software defined radio applications. This model may provide a more truly off-the-shelf solution as it will come standard with 50 Ω impedance ports.

There are many opportunities to expand upon the software and signal processing aspects of this research. In order to implement the fully software defined 16 element array of transceivers, additional software will be required to control radar operations in accordance with the scheduling, mode, and timing requirements of the radar. Future work should achieve compatibility between the software radio and the existing SuperDARN processing techniques for addressing bad lags, cross range interference, and estimating the Doppler velocity of the target.

Such work should address the networking and data handling requirements for scaling this prototype up to a full 16 element array. One potential method for addressing the data handling requirement may be to delegate processing to the individual SDRs and away from the central computer. Such work may include modifying the FPGA code for the Xilinx Zynq SoC to perform additional processing and to communicate with the central computer over the Red Pitaya's serial communication ports.

The most exciting opportunities for future work are potential experiments that could be conducted using a full SDR array and the techniques described in the second chapter of this work. One particular experiment may include using Barker codes and an adaptive approach to search for sub-auroral ion drifts (SAIDs) since these features are smaller in range than the standard SuperDARN range resolution. The multiple frequency, multiple beam approach could be used to visualize wavefronts of traveling ionospheric disturbances (TIDs) in radar field-of-view plots as a result of higher refresh rates. Alternatively, the multiple frequency, multiple beam approach could enable more frequent use of camping beam modes without interrupting standard radar operations. This functionality may prove especially useful in allowing future SuperDARN radars to operate in a bistatic mode without disrupting the monostatic operations. Overall, numerous opportunities exist for expanding on this work and integrating SDR into the next generation of SuperDARN radars.

4.2 Conclusions

Software defined radio is an enabling technology in modern radio and radar design thanks to rapid advancement in electronics design. In the context of SuperDARN radars, low-cost software defined radios facilitate improved beamforming and waveform processing techniques. This work showed that SDRs and digital beamforming can be used to improve the directional

resolution of SuperDARN radars. Combining digital beamforming techniques with frequency diversity would take advantage of the flexibility of software defined radios in order to improve the time resolution of the radar. Furthermore, implementing a cognitive radar approach could allow for finer range resolution during periods of high signal-to-noise ratio.

To demonstrate the feasibility of such a system, this work developed a low-cost prototype of a multichannel SDR receiver for SuperDARN radars. The Red Pitaya software defined radio's performance was characterized and modifications were made to improve its performance. These modifications included the design of a custom front end and a clock distribution board.

Laboratory results demonstrated the suitability of this prototype for SuperDARN radars. These results were confirmed through a field test at the Blackstone radar where the prototype performed comparably to the existing SuperDARN receiver hardware. Ultimately, this work showed adopting an SDR approach to SuperDARN radar design is feasible and could enable new science through superior measurement capabilities.

References

- [1] G. Chisam, M. Lester, S. Milan, M. Freeman, Bristow, W.A., A. Grocott, K. McWilliams, J. Ruohoniemi, T. Yeoman, P. Dyson, R. Greenwald, T. Kikuchi, M. Pinnock, J. Rash, N. Sato, G. Sofko, J.-P. Villain and A. Walker, "A decade of the Super Dual Auroral Radar Network (SuperDARN): scientific achievements, new techniques and future directions," *Survey in Geophysics*, vol. 28, no. 1, pp. 33-109, 2007.
- [2] R. Greenwald, K. Baker, J. Dudeney, M. Pinnock, T. Jones, E. Thomas, J.-P. Villain, J.-C. Cerisier, C. Senior, C. Hanuise, R. Hunsucker, G. Sofko, J. Koehler, E. Nielsen, R. Pellinen, A. Walker, N. Sato and H. Yamagishi, "DARN/SuperDARN," *Space Science Reviews*, vol. 71, no. 1-4, pp. 761-796, 1995.
- [3] N. Nishitani, J. M. Ruohoniemi, M. Lester, J. B. H. Baker, A. V. Koustov, S. G. Shepherd, G. Chisam, T. Hori, E. G. Thomas, R. A. Makarevich, A. Marchaudon, P. Ponomarenko, J. A. Wild, S. E. Milan, W. A. Bristow, J. Devlin, E. Miller, R. A. Greenwald, T. Ogawa and T. Kikuchi, "Review of the accomplishments of mid-latitude Super Dual Auroral Radar Network (SuperDARN) HF radars," *Progress in Earth and Planetary Science*, vol. 6, no. 1, p. 27, 2019.
- [4] J. Ruohoniemi, "Space@VT SuperDARN," Virginia Tech, [Online]. Available: <http://vt.superdarn.org/tiki-index.php>. [Accessed 17 February 2019].

- [5] K. T. Sterne, R. A. Greenwald, J. B. Baker and J. M. Ruohoniemi, "Modeling of a twin terminated folded dipole antenna for the Super Dual Auroral Radar Network (SuperDARN)," in *IEEE RadarCon*, Kansas City, 2011.
- [6] Drm310, "Super Dual Auroral Radar Network," Wikipedia, 4 July 2008. [Online]. Available: https://en.wikipedia.org/wiki/Super_Dual_Auroral_Radar_Network. [Accessed 14 March 2019].
- [7] G. Breit and M. Tuve, "A radio method of estimating the height of the conducting layer," *Nature*, vol. 116, no. 2914, p. 357, 1925.
- [8] M. A. Richards, J. A. Scheer and W. A. Holm, *Principles of Modern Radar Basic Principles*, Raleigh: SciTech Publishing, 2010.
- [9] J. S. Seybold, *Introduction to RF Propagation*, Hoboken: John Wiley & Sons, Inc., 2005.
- [10] M. A. Richards, *Fundamentals of Radar Signal Processing*, New York: McGraw Hill Education, 2014.
- [11] D. Farley, "Multiple-Pulse Incoherent-Scatter Correlation Function Measurements," *Radio Science*, vol. 7, no. 6, pp. 661-666, 1972.
- [12] J. H. Reed, *Software Radio A Modern Approach to Radio Engineering*, Upper Saddle River: Prentice Hall PTR, 2002.
- [13] Chetvorno, "Superheterodyne receiver," 8 January 2016. [Online]. Available: https://en.wikipedia.org/wiki/Superheterodyne_receiver. [Accessed 20 February 2019].

- [14] MathWorks, "Array Pattern Synthesis," PathWorks, 2019. [Online]. Available:
<https://www.mathworks.com/help/phased/examples/array-pattern-synthesis.html>.
[Accessed 14 March 2019].
- [15] R. T. Parris, W. Bristow and S. Shuxiang, "Imaging with the Kodiak radar: Hardware, Technique, and First Results," in *SuperDARN Workshop*, 2008.
- [16] R. O. Schmidt, "Multiple Emitter Location and Signal Parameter Estimation," *IEEE Transactions on Antennas and Propagation*, vol. 34, no. 3, pp. 276-280, 1986.
- [17] V. Pisarenko, "The retrieval of harmonics from a covariance function," *Geophysical Journal of the Royal Astronomical Society*, vol. 33, no. 3, pp. 347-366, 1973.
- [18] Y. Wu and W. Zou, "Orthogonal frequency division multiplexing: a multi-carrier modulation scheme," *IEEE Transactions on Consumer Electronics*, vol. 41, no. 3, pp. 392-399, 1995.
- [19] K. T. Sterne, Testing the Re-designed SuperDARN HF Radar and Modeling of a Twin Terminated Folded Dipole Array, Blacksburg: Virginia Tech, 2010.
- [20] W. Bennett, "Spectra of Quantized Signals," *Bell System Technical Journal*, vol. 27, pp. 446-471, 1948.
- [21] Red Pitaya, "Red Pitaya," Red Pitaya, 2019. [Online]. Available:
<https://www.redpitaya.com/>. [Accessed 18 February 2019].

- [22] P. Demin, "Red Pitaya Notes," [Online]. Available: <http://pavel-demin.github.io/red-pitaya-notes/>. [Accessed 4 March 2019].
- [23] M. Hirsch, "SciVision," 6 November 2016. [Online]. Available: <https://github.com/scivision/piradar/wiki>. [Accessed 4 March 2019].
- [24] R. W. McGwier, "Gnuradio, Citizen Science, and Red Pitaya," in *Hume Board of Directors Meeting*, Blacksburg, 2017.
- [25] Analog Devices, "AD8065/AD8066 Data Sheet," Analog Devices, 2019.
- [26] W. L. Stutzman, *Antenna Theory and Design*, Hoboken: John Wiley and Sons, Inc., 2013.
- [27] TriQUint Semiconductor, "AG303-86," TriQuint Semiconductor, 2019.
- [28] F. T. Ulaby and U. Ravaioli, *Fundamentals of Applied Electromagnetics*, Upper Saddle River: Pearson Education, Inc., 2015.
- [29] MicroChip, "DSC1103/23," MicroChip, 2019.
- [30] Maxim Integrated Products, "MAX9174/MAX9175," Maxim Integrated Products, Sunnyvale, 2019.

Appendix A – Cross Talk Analysis

A.1 Opposite Pairing Approach

The second approach considers pairing opposite array elements. In the case of opposed array element pairs, the first antenna element and the last antenna element in the linear array would both feed into the same Red Pitaya device and experience interference due to cross talk in the receive channels. An opposite pairing approach appears as a potentially attractive option if any symmetries exist in the values of the weighting vector. This new weighting scheme is apparent in the new formula for the cross talk array factor as shown in the equation below.

$$AF_2 = w_1 v_{16} + w_{16} v_1 + w_2 v_{15} + w_{15} v_2 + \dots + w_8 v_9 + w_9 v_8 \quad (\text{A.1})$$

The corresponding patterns for the original and cross talk array factors are shown in Figure A.1.

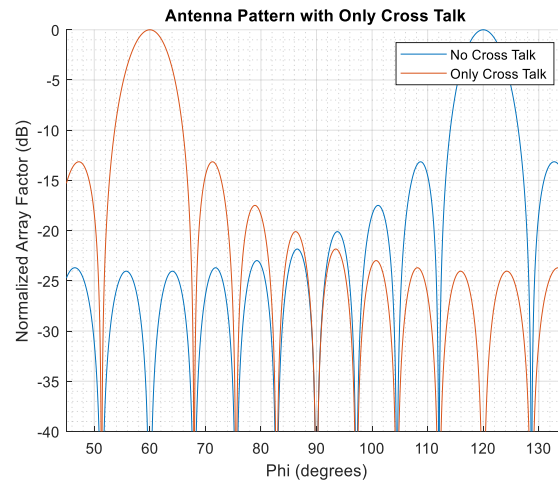


Figure A.1. Array Factors for Opposite Pairing Approach

Similar to the adjacent pairing approach, no overlap exists between the main lobes of the two array factors suggesting that this pairing scheme is likely to suffer the same gain loss and grating lobe issues experienced by the adjacent pairing scheme.

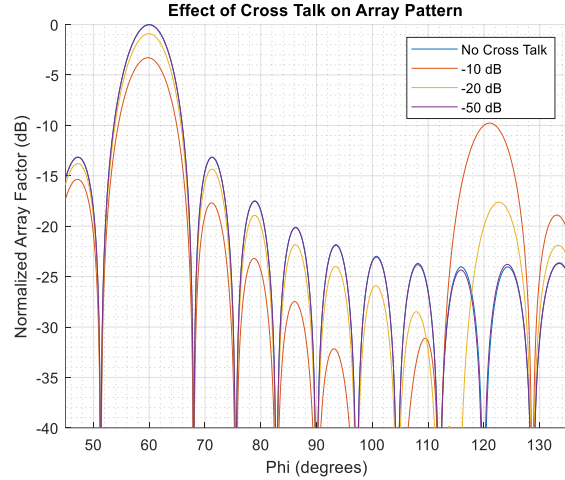


Figure A.2. Effect of Cross Talk on Opposite Pairing Scheme

As expected, this opposite pairing scheme produced suboptimal results similar to the adjacent pairing scheme due to its similar cross talk array factor.

A.2 Half Pairing Approach

The final approach to minimizing the cross talk issue used a half pairing scheme. In this approach, antenna elements separate by half of the antenna array are paired and would be fed into the same Red Pitaya device. In a SuperDARN 16 element linear array, a half pairing approach would dictate that the first antenna element be paired with the ninth. This pairing approach seeks to take advantage of periodicities within the weighting vector to minimize the differences between the original array factor and the cross talk array factor. This new weighting scheme is shown in the new formula for the cross talk array factor in the equation below.

$$AF_2 = w_1 v_{N/2+1} + w_{N/2+1} v_1 + w_2 v_{N/2+2} + w_{N/2+2} v_2 + \dots + w_{N/2} v_N + w_N v_{N/2} \quad (\text{A.2})$$

The corresponding patterns for the original and cross talk array factors are shown in Figure A.3.

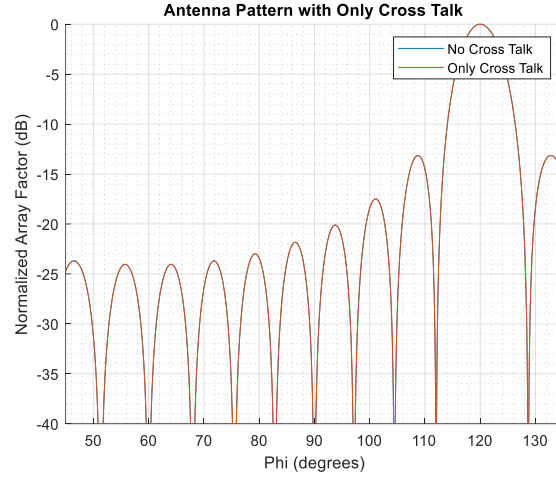


Figure A.3. Antenna Factors for the Half Pairing Approach

In contrast to the adjacent and opposite pairing schemes, the half pairing approach yields a cross talk array factor that closely matches the original array factor. In the case of a look direction 30° off broadside with a 16 element linear array, the cross talk array pattern exactly matches the original array factor. This result can be understood by examining the weighting vector for this particular circumstance. The formula for the element weights is given in the equation below, and the corresponding values are shown in Table A.1.

$$w_n = e^{jn\pi \cos \phi} \quad (\text{A.3})$$

$$w_n = e^{jn\pi \cos 60^\circ} \quad (\text{A.4})$$

$$w_n = e^{jn\pi/2} \quad (\text{A.5})$$

1	2	3	4	5	6	7	8
1	$1j$	-1	$-1j$	1	$1j$	-1	$-1j$
9	10	11	12	13	14	15	16
1	$1j$	-1	$-1j$	1	$1j$	-1	$-1j$

Table A.1. Antenna Element Weights for $\phi = 60^\circ$

As seen in the equation and table above, the weighting vector for this particular look direction is periodic. When used with the half pairing scheme, the effective array factor reduces to the original array factor as was the case for broadside radiation as shown in the equations below.

$$AF = w_1 v_1 + w_2 v_2 + \dots + w_N v_N \quad (\text{A.6})$$

$$AF = 1v_1 + jv_2 - v_3 - jv_4 + \dots + 1v_9 + jv_{10} - v_{11} - jv_{12} + \dots - jv_N \quad (\text{A.7})$$

$$AF_2 = w_1 v_{N/2+1} + w_{N/2+1} v_1 + w_2 v_{N/2+2} + w_{N/2+2} v_2 \quad (\text{A.8})$$

$$+ \dots + w_{N/2} v_N + w_N v_{N/2} \quad (\text{A.9})$$

$$AF_2 = 1v_9 + jv_{10} - v_{11} - jv_{12} + \dots + 1v_1 + jv_2 - v_3 - jv_4 + \dots - jv_{N/2}$$

$$AF = AF_2 = 1v_1 + jv_2 - v_3 - jv_4 + \dots + 1v_9 + jv_{10} - v_{11} - jv_{12} + \dots - jv_N \quad (\text{A.10})$$

$$AF_{eff} = \alpha AF + \rho AF_2 = (1 - \rho)AF + \rho AF = AF \quad (\text{A.11})$$

As a result, the array factor is entirely insensitive to the level of cross talk power as shown in Figure A.4.

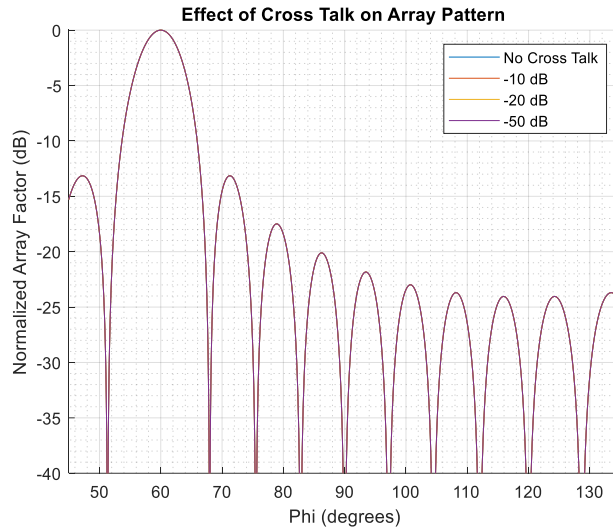


Figure A.4. Effect of Cross Talk on Half Pairing Scheme

Unfortunately, this result only holds true for this particular look direction. As the beam is steering throughout the field of view, the weighting vector does not remain completely periodic. Results for several look directions are shown in Figure A.5 for the case of -10 dB cross talk power.

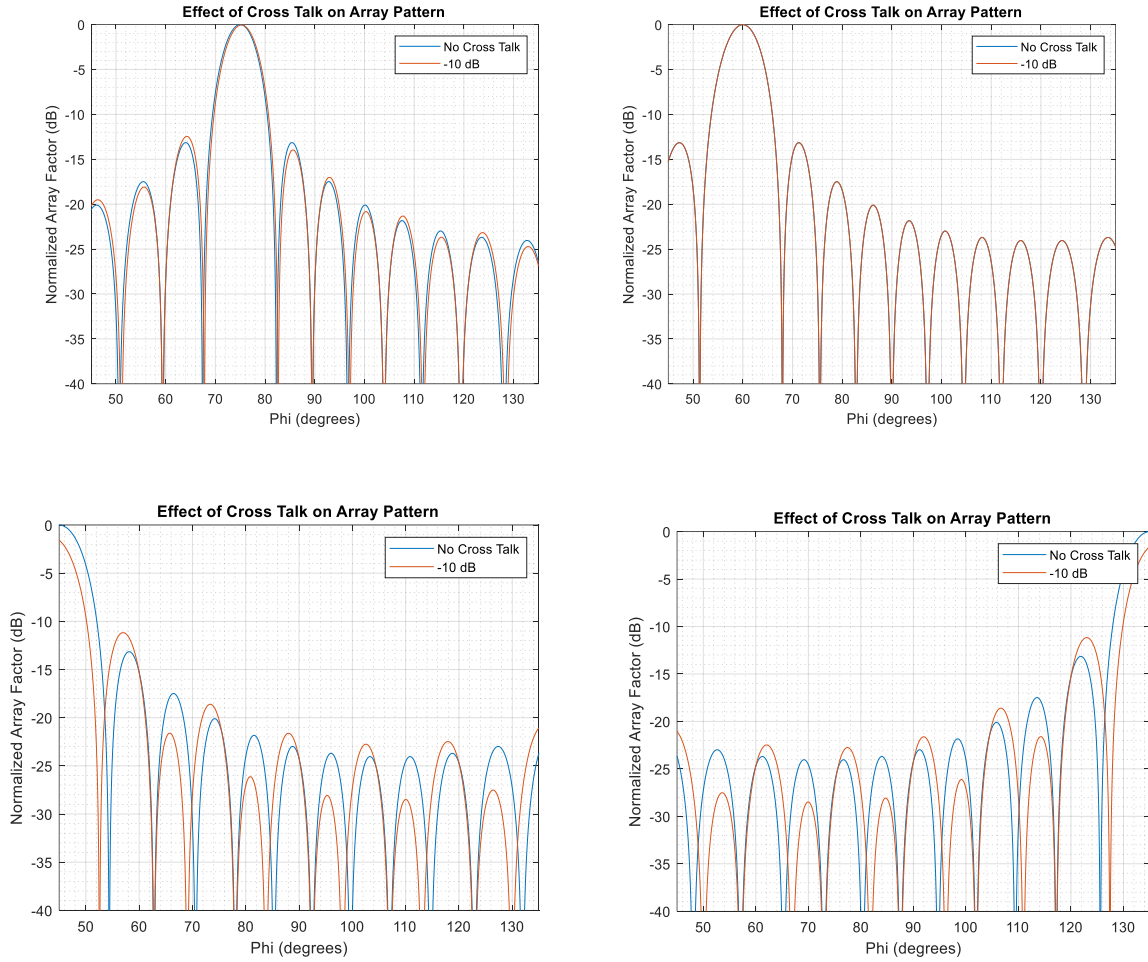


Figure A.5. Variation with Respect to Beam Direction for Half Pairing

The half pairing scheme does experience a loss of antenna gain in the main lobe like the adjacent and opposite pairing schemes. However, the loss in the half pairing scheme is relatively small, even for a large cross talk power of -10 dB. From Figure A.5, the worst loss cases for $45^\circ \leq \phi \leq 135^\circ$ occurs at $\phi = 45^\circ, 135^\circ$ and is less than 3 dB. Recalling Figure 3.13 from the adjacent pairing approach at the same cross talk power, the best case scenario for the adjacent pairing is comparable to the worst case scenario for the half pairing approach.

An additional consideration is the apparent lack of grating lobes. While some sidelobes are slightly increased, no major grating lobe is apparent as was the case in the adjacent and opposite

pairing approaches. The lack of a grating lobe suggests that the half pairing approach is vastly superior in terms of its ability to resolve spatial ambiguities and suppress clutter and interference. In order to further verify the absence of grating lobes, the Figure A.6 was produced showing the entire array factor for $0^\circ \leq \phi \leq 180^\circ$ with the worst case look direction of $\phi = 45^\circ$ and the expected cross talk power level of -50 dB. The backlobe pattern is neglected as the SuperDARN array utilizes a corner reflector placed on the backside of the array to minimize backlobe radiation. Additionally, potentially worse look directions beyond 45° are ignored as the SuperDARN radar field of view is limited to within this range both by the control software and the antenna element's radiation pattern.

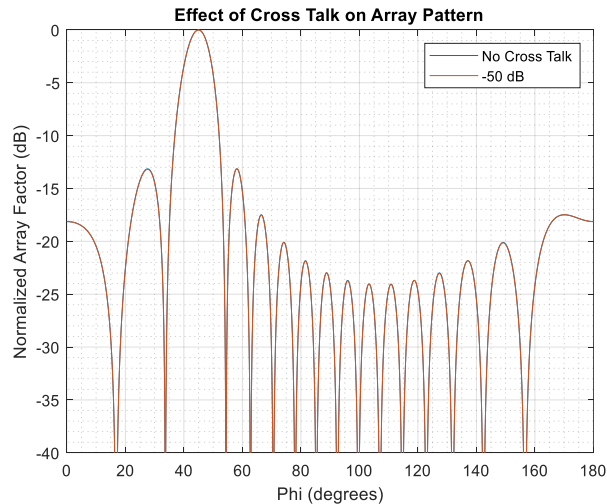


Figure A.6. Effect of Cross Talk on Half Pairing Approach

Almost no difference exists between the original array factor and the effective array factor after cross talk interference is introduced. Thus, it can be concluded that the half pairing approach is a sufficiently optimal pairing scheme for SuperDARN radars. However, it is important to note that this analysis assumed no non-linearities within the receivers which could introduce additional

interference into the system. Furthermore, this analysis only used half wavelength spacing which will change slightly as the SuperDARN radars use a range of frequencies.

In order to obtain the final radiation pattern for the SuperDARN antenna array, the antenna element radiation pattern will need to be included along with the array factor as shown above.

The optimum pairing scheme will vary in other antenna arrays with different numbers of elements, element spacings, and weighting schemes. Ultimately, the half pairing approach ensures that the cross talk within the Red Pitaya receive path will have a negligible effect on the performance of SuperDARN radar systems with rectangular weighting and suggests that cross talk can be overcome through careful pair selection in other weighting schemes.